UNIVERSIDADE ESTADUAL DE CAMPINAS
FACULDADE DE ENGENHARIA ELÉTRICA E DE COMPUTAÇÃO

Hening Almeida de Andrade

Integrated Couplers for OAM Fiber Modes

Acopladores Integrados para Modos OAM em Fibras

Campinas
2022

Hening Almeida de Andrade

Integrated couplers for OAM fiber modes

Acopladores integrados para modos OAM em fibras

Dissertation presented to the Faculty of Electrical and Computer Engineering of the University of Campinas in partial fulfillment of the requirements for the degree of Master in Electrical Engineering, in the area of Telecommunications and Telematics.

Dissertação apresentada à Faculdade de Engenharia Elétrica e de Computação da Universidade Estadual de Campinas como parte dos requisitos exigidos para a obtenção do título de Mestre em Engenharia Elétrica, na Àrea de Telecomunicações e Telemática.

Supervisor/Orientador: Lucas Heitzmann Gabrielli

Co-supervisor/Coorientador: Giovanni Beninca de Farias

Este exemplar corresponde à versão final da dissertação defendida pelo aluno Hening Almeida de Andrade, e orientada pelo Prof. Dr. Lucas Heitzmann Gabrielli.

Campinas
2022

Ficha catalográfica
Universidade Estadual de Campinas
Biblioteca da Área de Engenharia e Arquitetura
Rose Meire da Silva - CRB 8/5974

An24i

Andrade, Hening Almeida de, 1994-
Integrated couplers for OAM fiber modes / Hening Almeida de Andrade. – Campinas, SP : [s.n.], 2022.

Orientador: Lucas Heitzmann Gabrielli.
Coorientador: Giovanni Beninca de Farias.
Dissertação (mestrado) – Universidade Estadual de Campinas, Faculdade de Engenharia Elétrica e de Computação.

1. Momentos angulares. 2. Fibras óticas. 3. Comunicações ópticas. 4. Fotônica integrada. 5. Antenas óticas. I. Gabrielli, Lucas Heitzmann, 1982-. II. Farias, Giovanni Beninca de. III. Universidade Estadual de Campinas. Faculdade de Engenharia Elétrica e de Computação. IV. Título.

Informações para Biblioteca Digital

Título em outro idioma: Acopladores integrados para modos OAM em fibras
Palavras-chave em inglês:
Angular momentum
Optical fibers
Optical communications
Integrated photonics
Optical antennas
Área de concentração: Telecomunicações e Telemática
Titulação: Mestre em Engenharia Elétrica
Banca examinadora:
Lucas Heitzmann Gabrielli [Orientador]
Daniel Orquiza de Carvalho
Michel Zamboni Rached
Data de defesa: 20-04-2022
Programa de Pós-Graduação: Engenharia Elétrica

Identificação e informações acadêmicas do(a) aluno(a)
- ORCID do autor: https://orcid.org/0000-0002-1904-1502
- Currículo Lattes do autor: http://lattes.cnpq.br/0922143462560859

Comissão Julgadora – Dissertação de Mestrado

Candidato: Hening Almeida de Andrade **RA:** 226620

Data da defesa: 20 de Abril de 2022

Título da Tese: "Integrated Couplers for OAM Fiber Modes"

Prof. Dr. Lucas Heitzmann Gabrielli (Presidente, FEEC/UNICAMP)
Prof. Dr. Daniel Orquiza de Carvalho (UnB)
Prof. Dr. Michel Zamboni Rached (FEEC/UNICAMP)

A Ata de Defesa, com as respectivas assinaturas dos membros da Comissão Examinadora, encontra-se no SIGA/Sistema de Fluxo de Dissertação/Tese e na Secretaria de Pós-Graduação da Faculdade de Engenharia Elétrica e de Computação.

Dedication

To my family, especially my parents, who have always supported me and encouraged me throughout my life.

Acknowledgements

First of all, I would like to thank God for giving me the strength to overcome the difficulties along the way, without him none of this would be possible. Then, I would like to thank my parents for their love and support throughout my life.

To my advisor, Lucas Gabrielli, for all the ideas, discussions and knowledge sharing that were fundamental to build this research. I would also like to thank my co-advisor, Giovanni Farias, for encouraging me to study for a Master's degree and for his guidance since I started working with photonics.

To Julian Pita for introducing me to the Optical Communications Laboratory (LCO) and for working by my side most of the time, sharing his knowledge and giving me suggestions to this work. I also thank Erick and Paulão for their support in using the equipment of the LCO.

To my colleagues from the Advanced Electromagnetism and Computational Research Group (GEMAC), especially Lucas Gavião, Paloma and Rafael for their suggestions during the experimental demonstration. I also thank my colleagues from CPQD, BrPhotonics and Idea! for their support and for the fruitful discussions. Special thanks to Adriano for his support in the packaging process.

To my friends Alisson, Felipe, Arthur, Carol, Daniel, Lucas Motesino, Ana, Lucas Magalhães and Gabi for their support.

Finally, I would like to thank everyone who directly or indirectly contributed to this work.

The most incomprehensible thing about the world is that it is comprehensible.

Albert Einstein

Resumo

A popularização de novos serviços de internet e o número crescente de dispositivos interconectados está aumentando o tráfego global de internet, o que demanda redes de transmissão de dados com maior capacidade. Comunicação por fibra óptica é a principal tecnologia para transmissão de dados em longas distâncias e em altas taxas. Técnicas de multiplexação, como Multiplexação por Divisão de Polarização (PDM) e Multiplexação por Divisão de Comprimento de Onda (WDM) são utilizadas para aumentar o número de canais de comunicação em sistemas ópticos. Um novo domínio de multiplexação para explorar em fibras ópticas é o espaço. Multiplexação por Divisão de Espaço (SDM) propõe o uso de fibras multi-núcleo e multimodo para aumentar o número de canais usando vários núcleos e vários modos, respectivamente. O uso de vários modos para transmissão de dados também é chamado de Multiplexação por Divisão de Modos (MDM). Uma base modal atrativa para MDM é a família de modos com Momento Angular Orbital (OAM) devido à robustez desses modos contra perturbações. Embora os modos OAM possam ser facilmente gerados em espaço livre, requer componentes adicionais e montagens muito volumosas e sensíveis ao desalinhamento. Acopladores integrados podem ser utilizados como soluções compactas e eficientes para geração e detecção de modos OAM em sistemas MDM.

Neste trabalho, projetamos e comparamos acopladores integrados para modos OAM em fibras utilizando a plataforma de Silício sobre Isolante (SOI) e baseado em três diferentes abordagens: antenas compactas, grade circular e otimização topológica. Os resultados de simulação mostraram que os dispositivos projetados podem acoplar os modos OAM analisados com baixa interferência intermodal. Os dispositivos projetados por otimização topológica apresentaram os melhores resultados de eficiência, enquanto as antenas compactas e a grade circular podem ser sintonizadas para diferentes modos OAM. A grade circular apresentou resultados um pouco melhores do que as antenas compactas, à custa de uma maior dependência na ordem do OAM. Também demonstramos experimentalmente o uso do acoplador OAM baseado em antenas compactas, o qual foi fabricado em uma foundry de fotônica em silício, para o acoplamento de modos OAM em uma Fibra de Cristal Fotônico de Núcleo Oco (HC-PCF) disponível no nosso laboratório. Os acopladores propostos podem ser potencialmente aplicados como soluções compactas e eficientes para geração/detecção em sistemas MDM onde modos OAM são usados para aumentar a capacidade de transmissão de dados de links ópticos.

Abstract

The popularization of new internet services and the growing number of interconnected devices is increasing the global internet traffic, which demands data transmission networks with larger capacity. Fiber-optic communication is the main communication technology for long-distance and high-speed data transmission. Multiplexing techniques, such as Polarization Division Multiplexing (PDM) and Wavelength Division Multiplexing (WDM) are used to increase the number of communication channels in optical systems. A new multiplexing domain to exploit in optical fibers is the space. Space division multiplexing (SDM) proposes the use of multicore and multimode fibers to increase the number of communication channels using multiple cores and multiple modes, respectively. The use of multiple modes for data transmission is also called Mode Division Multiplexing (MDM). An attractive modal basis for MDM is the family of modes with Orbital Angular Momentum (OAM) due to the robustness of those modes against perturbations. Although OAM modes can be easily generated in free-space, it requires additional components and very bulky and sensitive to misalignment setups. Integrated couplers can be used as compact and efficient solutions for OAM generation and detection in MDM systems.

In this work, we design and compare integrated couplers for OAM fiber modes using the Silicon On Insulator (SOI) platform and based on three different approaches: compact antennas, circular grating and topology optimization. Simulation results show that the designed devices can couple the analysed OAM fiber modes with low intermodal crosstalk. The devices designed by topology optimization showed the best efficiency results, while the compact antennas and the circular grating can be tuned for different OAM modes. The circular grating showed slightly better results than the compact antennas at the expense of a higher dependence on the OAM order. We also experimentally demonstrate the use of the OAM coupler based on compact antennas, that was fabricated in a silicon photonics foundry, for the coupling of OAM modes in a Hollow-Core Photonic Crystal Fiber (HC-PCF) available in our laboratory. The proposed couplers can potentially be applied as compact and efficient solutions for generation/detection in MDM systems where OAM modes are used to increase the data transmission capacity of optical links.

List of Figures

List of Tables

List of Abbreviations

API	Application Programming Interface
BG	Bessel-Gaussian
BOX	Buried Oxide
CAGR	Compound Annual Growth Rate
CE	Coupling Efficiency
CGH	Computer Generated Holograms
CMOS	Complementary Metal-Oxide Semiconductor
DFM	Design for Manufacturing
DSP	Digital Signal Processing
FEM	Finite Element Method
FDTD	Finite-Difference Time-Domain
FFT	Fast Fourier Transform
FOM	Figure of Merit
FSR	Free Spectral Range
GEMAC	Advanced Electromagnetism and Computational Research Group
GND	Ground
HC-PCF	Hollow-Core Photonic Crystal Fiber
HC-PBGF	Hollow-Core Photonic Bandgap Fiber
HG	Hermite–Gaussian
HOM	Higher-Order Modes
IFT	Inverse Fourier Transform
IoT	Internet of Things
IS	Integrating Sphere
LCO	Optical Communications Laboratory

LG	Laguerre–Gaussian
LP	Linearly Polarized
M2M	Machine-to-Machine
MDM	Mode Division Multiplexing
MFD	Mode Field Diameter
MPW	Multi Project Wafer
MMI	Multimode Interferometer
NA	Numerical Aperture
OAM	Orbital Angular Momentum
OL	Objective Lens
PC	Polarization Controller
PCF	Photonic Crystal Fiber
PBGF	Photonic Bandgap Fiber
PDK	Process Design Kit
PDM	Polarization Division Multiplexing
PIC	Photonic Integrated Circuit
PID	Proportional Integral Derivative
PM	Power Meter
PML	Perfectly Matched Layer
PSO	Particle Swarm Optimization
SAM	Spin Angular Momentum
SC-PCF	Solid-Core Photonic Crystal Fiber
SDM	Space division multiplexing
SEM	Scanning-Electron Microscope
SLM	Spatial Light Modulator
SMF	Single Mode Fiber
SOI	Silicon On Insulator
SPP	Spiral Phase Plates
TE	Transverse Electric

TM	Transverse Magnetic
TOX	Top Oxide
TLS	Tunable Laser Source
VA	Variable Attenuator
WDM	Wavelength Division Multiplexing

Contents

Chapter 1

Introduction

In recent years, a variety of internet services, such as web conferencing, video streaming, cloud storage and social networks, became popular and increasingly attracts more users. Cisco forecasts that the total number of Internet users will grow from 3.9 billion in 2018 to 5.3 billion in 2023, which represents a 6% Compound Annual Growth Rate (CAGR) [10]. The emergence of new technologies, such as 5G, Internet of Things (IoT) and cloud computing is making the number of connected devices grow even faster (10% CAGR) with the Machine-to-Machine (M2M) connections representing the fastest-growing category (19% CAGR) [10]. As a consequence, the global Internet traffic is increasing and requiring transmission networks with larger capacity.

The vast majority of all communication in the world goes through a worldwide network of interconnected optical fibers [11]. Fiber-optic communication is the most advanced technology for long-distance and high data rate transmission, offering low loss, low latency, wide bandwidth and tight spatial confinement [11–13]. Typical optical links use Single Mode Fiber (SMF) to transmit data through the modulation of light. Higher-order modulation formats and multiplexing techniques are applied to increase the capacity of these links. While PDM uses both orthogonal polarization states of the light, WDM uses multiple operation wavelengths to increase the number of communication channels. However, WDM is limited by the transmission windows in which the optical fiber can propagate light with low attenuation and the optical bandwidth of the devices, such as optical amplifiers. To overcome the limitations of WDM, a new multiplexing domain is the space. SDM can use multicore fibers and multimode fibers to provide additional communication channels. While in multicore fibers, each core represents a different channel, in multimode fibers, each supported mode represents a different channel, which is also known as MDM. Additionally, multicore fibers with each core supporting multiple modes can exploit even more the space for multiplexing.

MDM can also be extended to photonic integration for the improvement of density, efficiency and interconnection capacity [14]. For those reasons, it is considered the most promising method for maintaining the trend of “Moore’s law” in photonic integration and optical fiber transmission [14]. An attractive modal basis for MDM systems is the family of modes that carry OAM. Due to the robustness of those modes against perturbations, we can potentially achieve multimode transmission with very low intermodal crosstalk and reduce the receiver complexity [15]. The concept of OAM modes is associated with optical vortex, in which the optical beam twists around the propagation axis with the planes of constant phases running in a helical pattern. OAM beams can be easily generated in free-space using, for example, Spiral Phase Plates (SPP), q-plates, and Computer Generated Holograms (CGH) programmed on Spatial Light Modulator (SLM) [4, 15, 16]. These collimated OAM beams can then be coupled to multimode fibers using focusing lenses. However, these setups are very bulky and sensitive to misalignment. The use of integrated devices to generate and couple OAM modes into fibers can potentially reduce the complexity and size of MDM systems.

Integrated photonics provides low size, low power consumption and high scalability of optical devices. One of the most promising technologies for the development of integrated optical devices is silicon photonics. The optical properties of silicon enable the development of compact and low-loss optical devices, while also benefiting from the maturity and know-how of Complementary Metal-Oxide Semiconductor (CMOS) processing techniques to achieve high-yield and cost reduction in large-scale fabrication [17]. Silicon photonics is applied in wide range of applications from telecom and datacom to sensing [18]. The main strategies for fiber-to-chip coupling in silicon photonics are based on waveguide tapers for edge coupling and diffraction elements for out-of-plane coupling. The vast majority of the proposed OAM couplers in the literature are based on out-of-plane coupling due to the fabrication complexity of the design using edge coupling. The first OAM couplers were designed for free-space applications [7, 19, 20]. These devices are based on microring resonator [19], circular grating [7] and nanoantenna phased array [20]. For fiber transmission, an array of grating couplers were proposed [21], but, due to the dimensions of the device, an external focusing element is required for the coupling into the fiber. For direct fiber-to-chip coupling a forked-grating coupler [22], an array of 2D grating couplers [23] and a circular grating coupler [24] were proposed. However, these designs have some limitations, such as the coupling of only one OAM mode, few devices in the array due to the grating dimensions, and coupling with only a specially designed fiber, respectively.

In this work, we aim to develop compact and efficient integrated couplers, in SOI platform, for the coupling of different OAM modes into multimode fibers. To achieve this, we analyse different design approaches based on compact antennas, circular grating and topology optimization. Finite Element Method (FEM) and Finite-Difference Time-Domain (FDTD) simulations are performed during the design process to obtain the OAM fiber modes and OAM couplers' results, respectively. Evolutionary and gradient-based algorithms are also applied for the optimization of the designs and the overlap integral is applied to calculate the performance of the proposed couplers. A Photonic Integrated Circuit (PIC) with one of the proposed OAM couplers is fabricated at IMEC/Europractice in a Multi Project Wafer (MPW) run. The fabricated OAM coupler is characterized using different methods to demonstrate the coupling of OAM modes into a HC-PCF available in our laboratory.

This dissertation is organized in five chapters, with the first one being this introduction. In Chapter 2, we present the fundamentals of light propagation in optical fibers, basic concepts of optical modes and the angular momentum of the light. We also discuss the generation and detection of OAM beams and the use of integrated photonics for the development of OAM couplers. In Chapter 3, we present the proposed OAM couplers, their design considerations and simulation results. We also compare the three design approaches, showing the advantages of each one in relation to the others. In Chapter 4, we present the designed PIC for the control and characterization of the OAM couplers. The experimental setups and procedures for the characterization of the OAM couplers are also detailed and the obtained experimental results are discussed. Finally, in Chapter 5, we present the main conclusions and opportunities for future works.

The following publications were a result of this Master's project:

1. **H. A. de Andrade**, J. L. Pita, G. B. de Farias, and L. H. Gabrielli, "Integrated Couplers for OAM Fiber Modes using Compact Antennas and Circular Grating," in Frontiers in Optics / Laser Science, pp. FM2D.2, Optical Society of America, 2020.

2. **H. A. de Andrade**, J. L. Pita, G. B. de Farias, and L. H. Gabrielli, "Demonstration of Integrated Coupler Based on Compact Antennas for OAM Fiber Modes," in CLEO: Science and Innovations, pp. SM2N.7. Optical Society of America, 2022.

Chapter 2

Fundamentals of OAM Modes and Coupling

In this chapter, we first present the fundamentals of light propagation in optical fibers, then, we describe the basic concepts of optical modes. The angular momentum of the light is explained and we analyse the propagation of OAM beams in free-space and in optical fibers. Finally, we present the main approaches to generate and detect OAM modes from classical free-space setups to novel integrated approaches.

2.1 Light Propagation in Optical Fibers

2.1.1 Ray Optics

An optical fiber in its simplest form is composed by a cylindrical core and a surrounding cladding made of glass with the refractive index of the cladding lower than the refractive index of the core [25]. This type of optical fiber with an abrupt change in the refractive index is called step-index fiber, which differs from the graded-index fiber, where the refractive index between core and cladding changes gradually. The light propagation in optical fibers is based on the principle of total internal reflection, where, for a step-index fiber, an optical ray will be confined in the optical fiber if the angle when it hits the core-cladding interface is larger than a critical angle (ϕ_c), defined by [25]:

$$\sin \phi_c = n_2/n_1 \tag{2.1}$$

where n_1 is the refractive index of the core and n_2 is the refractive index of the cladding. The light confinement through total internal reflection in a step-index fiber is illustrated in Fig. 2.1.

The maximum angle of the incident ray with the fiber axis to remain confined inside the core is given by [25]:

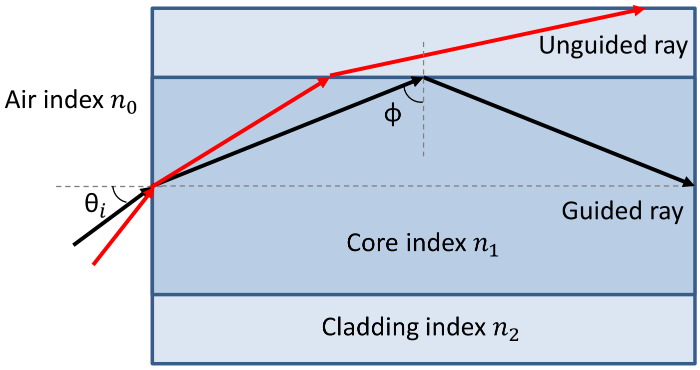

Figure 2.1: Light confinement through total internal reflection in a step-index fiber.

$$n_0 \sin\theta_i = n_1 \cos\phi_c = (n_1^2 - n_2^2)^{1/2} \tag{2.2}$$

where n_0 is the refractive index of the air and θ_i is the angle of the incident ray. The term $n_0 \sin\phi_i$ is known as the Numerical Aperture (NA) of the fiber and it represents its light-gathering capacity [25]. Another important property of optical fibers is its refractive index contrast, given by [25]:

$$\Delta = (n_1 - n_2)/n_1 \tag{2.3}$$

2.1.2 Wave Equation

The light is an electromagnetic wave and, like all electromagnetic phenomena, it is governed by the Maxwell's equations, which describe the temporal and spatial evolution of the electric and magnetic fields. For a nonconducting medium without free charges, these equations can be written as (the shown notation and derivation follows mostly [21, 25, 26]):

$$\nabla \times \mathbf{E} = -\partial\mathbf{B}/\partial t \tag{2.4a}$$
$$\nabla \times \mathbf{H} = \partial\mathbf{D}/\partial t \tag{2.4b}$$
$$\nabla \cdot \mathbf{D} = 0 \tag{2.4c}$$
$$\nabla \cdot \mathbf{B} = 0 \tag{2.4d}$$

where **E** and **H** are the electric and magnetic field vectors, respectively. **D** and **B** are their respective flux densities. In a dielectric medium, they are related to the field vectors by:

$$\mathbf{D} = \varepsilon_r \varepsilon_0 \mathbf{E} \tag{2.5a}$$
$$\mathbf{B} = \mu_r \mu_0 \mathbf{H} \tag{2.5b}$$

where ε_r and μ_r are, respectively, the relative permittivity and relative permeability of the medium, and ε_0 and μ_0 are the vacuum permittivity and vacuum permeability, respectively. Taking the curl ($\nabla\times$) on both sides of Eq. 2.4a and combining it with Eqs. 2.4b, 2.5a and 2.5b, we obtain the wave equation for the electric field:

$$\nabla \times \nabla \times \mathbf{E} = -\frac{\varepsilon_r \mu_r}{c^2}\frac{\partial^2 \mathbf{E}}{\partial t^2} \tag{2.6}$$

where the speed of light in vacuum is defined by c $= (\mu_0\varepsilon_0)^{-1/2}$. Eq. 2.6 can be written in the frequency domain as:

$$\nabla \times \nabla \times \tilde{\mathbf{E}} = -\varepsilon_r(\mathbf{r},\omega)\frac{\omega^2}{c^2}\tilde{\mathbf{E}} \tag{2.7}$$

where $\varepsilon_r(\mathbf{r},\omega)$ is the frequency dependent relative permittivity. In general, ε_r is complex and its real and imaginary parts are related to the refractive index n and absorption coefficient α, respectively, by the definition:

$$\varepsilon_r = (n + i\alpha c/2\omega)^2 \tag{2.8}$$

where n and α are both frequency dependent. The frequency dependence of n is called chromatic dispersion or material dispersion [25]. Because of the low loss of silica optical fibers, ε_r can be taken to be real and replaced by n^2. Since n is independent of the spatial coordinates in both core and cladding of a step-index fiber and the index difference between core and cladding is small (in the order of $\sim 10^{-2}$), one can use the identity [21, 25–27]:

$$\nabla \times \nabla \times \tilde{\mathbf{E}} \equiv \nabla(\nabla \cdot \tilde{\mathbf{E}}) - \nabla^2\tilde{\mathbf{E}} = -\nabla^2\tilde{\mathbf{E}} \tag{2.9}$$

where we used Eqs. 2.4c and 2.5a to set $\nabla \cdot \tilde{\mathbf{E}} = 0$. This is called the "weakly-guiding" or "scalar" approximation [21, 26, 27]. Taking this assumptions, Eq. 2.7 can be simplified to obtain a wave equation called Helmholtz equation:

$$\nabla^2\tilde{\mathbf{E}} + n^2(\omega)k_0^2\tilde{\mathbf{E}} = 0 \tag{2.10}$$

with the wave number in vacuum $k_0 = \omega/c = 2\pi/\lambda$. λ is the vacuum wavelength of the optical field oscillating at the frequency ω [25]. In a similar way, the wave equation for the magnetic field can be obtained:

$$\nabla^2\tilde{\mathbf{H}} + n^2(\omega)k_0^2\tilde{\mathbf{H}} = 0 \tag{2.11}$$

2.1.3 Optical Modes

An optical mode is a specific solution of the wave equation that satisfies the appropriate boundary conditions and it has the property that its spatial distribution does not change with propagation [25]. The fiber modes can be classified as guided modes, leaky modes, and radiation modes [25]. The guided modes are the ones used for signal transmission in fiber-optic communication.

For a fiber with cylindrical symmetry, a Helmholtz equation for the field U (which can be either the electric or magnetic field) in cylindrical coordinates can be set up using the scalar approximation [21]:

$$\frac{\partial^2 U}{\partial r^2} + \frac{1}{r}\frac{\partial U}{\partial r} + \frac{1}{r^2}\frac{\partial^2 U}{\partial \phi^2} + \frac{\partial^2 U}{\partial z^2} + n^2 k_0^2 U = 0 \tag{2.12}$$

The modes, which are propagating in the z-direction need to be periodic in the angle ϕ with a period of 2π, which makes it possible to write the function as [21]:

$$U(r, \phi, z) = u(r)e^{-im\phi - i\beta z}, \text{ with } m = 0, \pm 1, \pm 2, ... \tag{2.13}$$

For step-index fibers, this equation leads to well-known solutions for $u(r)$ that are different Bessel functions [21]:

$$u(r) \propto J_m(k_T r) \text{ for } r < a \tag{2.14a}$$

$$u(r) \propto K_m(\gamma r) \text{ for } r > a \tag{2.14b}$$

where a is the fiber core, J_m is the Bessel function of the first kind and order m, K_m is the modified Bessel function of the second kind and order m. k_T and γ are defined by [21]:

$$k_T^2 = n_1^2 k_0^2 - \beta^2 \tag{2.15a}$$

$$\gamma = \beta^2 - n_2^2 k_0^2 \tag{2.15b}$$

where β is the propagation constant of the mode. A useful parameter to identify the mode is its mode index, or effective index, defined as $n_{\text{eff}} = \beta/k_0$. A guided mode propagates with an effective index whose value lies in the range $n_1 > n_{\text{eff}} > n_2$. The mode is said to reach cutoff and ceases to be guided when $n_{\text{eff}} \leq n_2$. A parameter that plays an important role in determining the cutoff condition is called the normalized frequency V, or simply the V parameter, defined by:

$$V = k_0 a (n_1^2 - n_2^2)^{1/2} \approx (2\pi/\lambda) a n_1 \sqrt{2\Delta} \tag{2.16}$$

As the frequency is increased or the geometry is enlarged, the value of V increases and more modes are supported by the fiber. A rough estimate of the number of modes is given by $V^2/2$. For example, a fiber with $a = 25\,\mu\text{m}$ and $\Delta = 5 \times 10^{-3}$ has $V \simeq 18$ at $\lambda = 1.3\,\mu\text{m}$ and supports about 162 modes. However, the number of supported modes decreases rapidly as V is reduced. For example, a fiber with $V = 5$ supports only 7 modes [25]. Fibers where only a single guided mode is able to propagate are called single-mode fibers. They differ from fibers where many modes can propagate, called multimode fibers. For SDM applications, special fibers called few-mode fibers are interesting, which usually support less than 10 guided modes [21].

In the case of more complicated index-profile shapes within the core, even though many strategies have been developed in the past to solve the scalar wave equation, numerical methods are applied [26]. It is customary to denote the solutions by β_{mn} with each value of β_{mn} corresponding to one possible mode of propagation. In general, both $\mathrm{E_z}$ and $\mathrm{H_z}$ are nonzero (except for $m = 0$), in contrast with planar waveguides, where one of them can be taken to be zero. Fiber modes are therefore referred to as hybrid modes and they are denoted by $\mathrm{HE_{mn}}$ or $\mathrm{EH_{mn}}$, depending on whether $\mathrm{H_z}$ or $\mathrm{E_z}$ dominates, respectively. In the special case of $m = 0$, $\mathrm{HE_{0n}}$ and $\mathrm{EH_{0n}}$ are also denoted by $\mathrm{TE_{0n}}$ and $\mathrm{TM_{0n}}$, respectively, since they correspond to a Transverse Electric (TE) mode, where $E_z = 0$, and a Transverse Magnetic (TM) mode, where $H_z = 0$. For weakly guiding fibers, both $\mathrm{E_z}$ and $\mathrm{H_z}$ are nearly zero. These modes are called Linearly Polarized (LP) modes and a different notation $\mathrm{LP_{mn}}$ is used [25].

LP Modes

The LP modes are obtained when the scalar approximation is applied. These modes possess a linear polarization and their field distribution are described by the Bessel functions of Eqs. 2.14a and 2.14b with an azimuthal dependence in the form of $\cos(m\phi)$. In the label $\mathrm{LP_{mn}}$, m represents the angle dependence and n is the mode order in the radial direction that is characterized by the Bessel function of $(n-1)$-th order [21]. The electric field intensity profile of the first LP modes of a step-index few-mode fiber is illustrated in Fig. 2.2. The lowest-order mode ($\mathrm{LP_{01}}$) is called the fundamental mode and its field distribution is approximated by a Gaussian beam [21]. This is the only mode supported (in both orthogonal polarizations) by a single-mode fiber.

Relation Between LP Modes and Hybrid Modes

When the scalar approximation is not applied, we obtain the full-vectorial solutions for the eigenmodes of the fiber, called hybrid modes. The fundamental mode in this case is the $\mathrm{HE_{11}}$ mode, which is equivalent to the $\mathrm{LP_{01}}$ mode. The second order modes are the $\mathrm{TE_{01}}$, $\mathrm{HE_{21}}$ and $\mathrm{TM_{01}}$ modes. These modes are almost degenerate, i.e. they have slightly different propagation constants. When the scalar approximation is applied, these three modes are all degenerate and the $\mathrm{LP_{11}}$ modes can be constructed by the linear combination of these modes, forming an alternative modal basis [21]. The relation between the $\mathrm{LP_{11}}$ modes and the hybrid modes in a step-index few-mode fiber is illustrated in

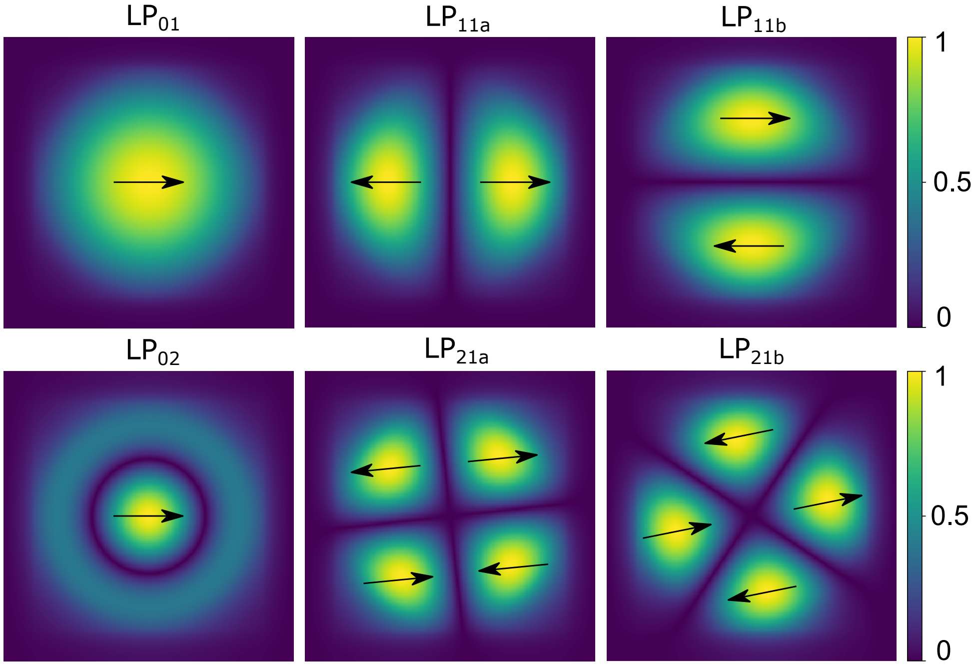

Figure 2.2: Magnitude of the electric field for different LP modes in a step-index few-mode fiber. The arrows indicate the polarization direction of the electric field. Each mode has also a version in the other orthogonal polarization (not shown).

Fig. 2.3. The HE_{21}^{even} and HE_{21}^{odd} modes are strictly degenerate and differ by the parity symmetry of the polarization lines. The same can be applied for higher-order LP modes. Although the scalar approximation is often used in fibers with very small index difference between core and cladding, LP modes are not true eigenmodes of the fiber and the signal transmitted by a LP mode is actually transmitted by a linear combination of different eigenmodes propagating with slightly different velocities. As a consequence, LP modes are not stable over long distance [21].

2.2 The Angular Momentum of Light

The light, as any electromagnetic wave, can carry both energy and momentum (linear and angular) [4]. In 1936, the angular momentum of light was first experimentally demonstrated [28], but only much later, in 1992 [29], it was described that this angular momentum is composed by two parts: a Spin Angular Momentum (SAM) and an OAM [30]. SAM is related to the polarization of the light, while OAM is related to its spatial distribution. SAM can be represented by $\pm\sigma$, with the sign depending on the handedness of the circular polarization, as illustrated in Fig. 2.4(a) [21]. Linearly polarized beams do not possess SAM [30]. The OAM that photons carry generates a twist of the light. As a consequence, OAM beams have a helical phase front with a phase dependence in the form of $e^{i\ell\phi}$, where ϕ is the azimuth angle and ℓ is called the topological charge. The amplitude of ℓ indicates the number of intertwined helices in the propagation distance

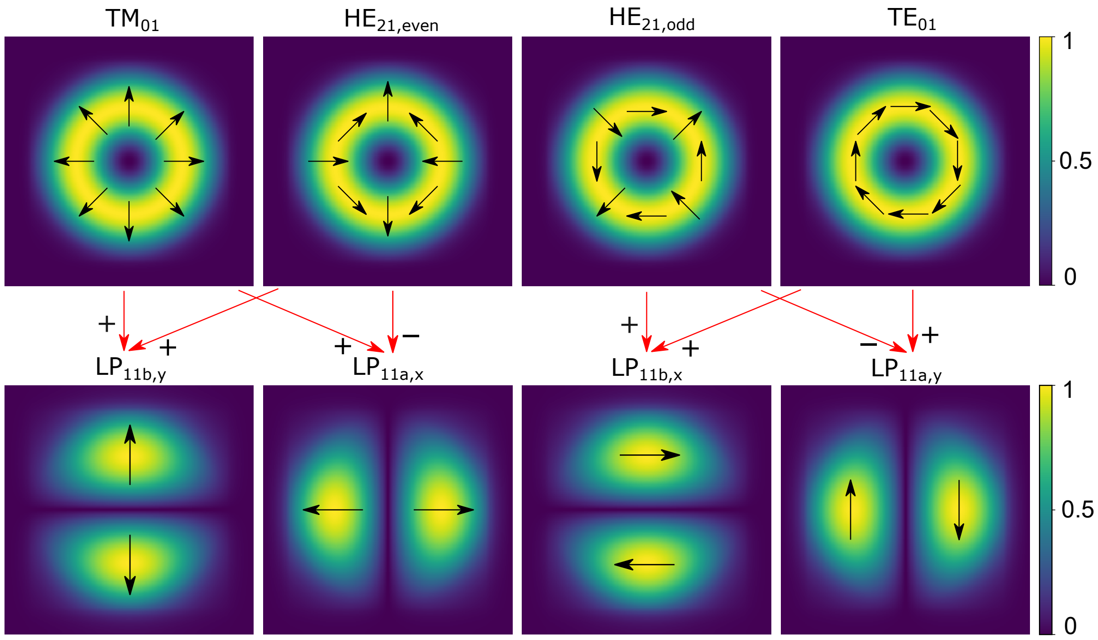

Figure 2.3: Relation between LP modes and hybrid modes in a step-index few-mode fiber.

of one wavelength and the sign of ℓ indicates its handedness, as illustrated for different OAM states in Fig. 2.4(b). The topological charge can assume any integer value and the number of orthogonal OAM states is infinite [31].

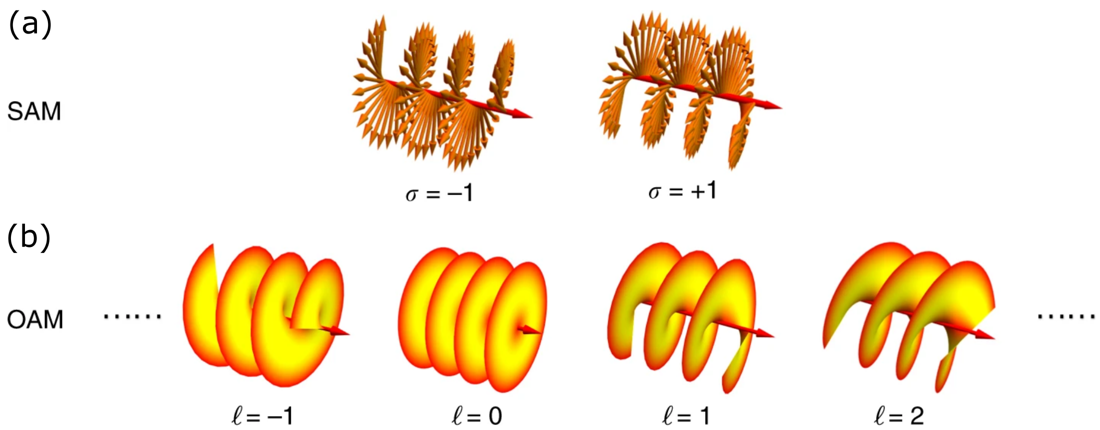

Figure 2.4: (a) States of SAM in circularly polarized beams. (b) OAM beams with different topological charges. "Adapted from [1], which is licensed under Creative Commons Attribution 4.0 International (CC BY 4.0)."

2.2.1 OAM Beams in Free-space

In free-space, many types of beams can carry OAM, such as Laguerre–Gaussian (LG) beams, Hermite–Gaussian (HG) beams, Bessel beams, Bessel-Gaussian (BG) beams, among others [32, 33]. OAM beams were first described by LG beams, which are the solutions of the paraxial wave equation in cylindrical coordinates and they are given by [29, 30, 34]:

$$LG_{\ell p}(\rho,\phi,z,t) = \frac{C_{\ell p}}{\sqrt{w(z)}}\left(\frac{\rho\sqrt{2}}{w(z)}\right)^{|\ell|}\exp\left(-\frac{\rho^2}{w^2(z)}\right)L_p^{|\ell|}\left(\frac{2\rho^2}{w^2(z)}\right)\exp\left(-ik\frac{\rho^2 z}{2\left(z_R^2+z^2\right)}\right)\times$$

$$\times\exp\left(i\ell\phi\right)\exp\left[-i(2\rho+|\ell|+1)\chi(z)\right]\exp\left(ikz\right)\exp\left(-i\omega t\right) \tag{2.17}$$

where

$$C_{\ell p} = \sqrt{\frac{2^{|\ell|+1}p!}{\pi(p+|\ell|)!}},\quad w^2(z) = w_0^2\left[1+\left(\frac{z}{z_R}\right)^2\right],\quad z_R = \frac{\pi w_0^2}{\lambda},\quad \tan(\chi) = \frac{z}{z_R} \tag{2.18}$$

w_0 is the initial beam waist and $L_p^{|\ell|}$ are the generalized Laguerre polynomials. The azimuthal index ℓ refers to the phase variation in the transverse plane and it represents the OAM topological charge. The radial index p refers to the number of zeros of $L_p^{|\ell|}$ in the radial direction. $C_{\ell p}$ is a normalization constant for the beam power, $w(z)$ is the beam waist in the longitudinal position z, z_R is the Rayleigh length and χ is the Gouy phase [30].

Using Eqs. 2.17 and 2.18, we calculate the electric field intensity and phase profile for the OAM beams of Fig. 2.4(b) with $p = 0$, $\lambda = 1550\,\text{nm}$ and $w_0 = 7\,\mu\text{m}$. The results obtained can be seen in Fig. 2.5. As we can see, except for $\ell = 0$, which is equivalent to a Gaussian beam, these modes have a ring-shaped intensity profile, whose radius increases with the amplitude of ℓ. The phase profile is composed by the phase surface of ℓ beams, shifting the phase ℓ times from $-\pi$ rad to $+\pi$ rad. The sign of ℓ indicates the handedness of the phase shift.

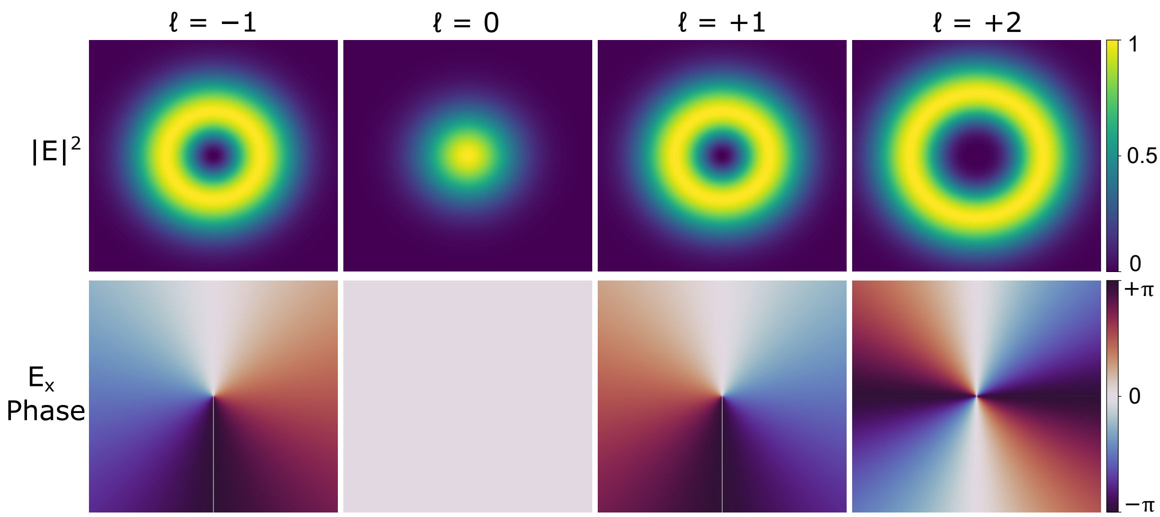

Figure 2.5: Electric field intensity and phase profile of OAM beams with different topological charges.

HG beams are also solutions of the paraxial wave equation, but in Cartesian coordinates [33]. The intensity distribution of these beams shows a petaloid structure and they can be superposed to obtain LG beams [29, 33]. Bessel beams are non-difractive beams, which are exact solutions of the wave equation in cylindrical coordinates and, similar to LG beams, they are also OAM beams with helical phase structure [33]. The complex amplitude of Bessel beams are described by a Bessel function of the first kind and it is given by [33]:

$$BB_\ell(r, \phi, z) = A_\ell J_\ell(k_r r) e^{-ik_z z} e^{i\ell\phi} \tag{2.19}$$

where A_ℓ is a constant, k_r is the wave number in the radial direction and k_z is the wave number in the beam propagation direction. Both wave numbers are satisfied by the wave number k [33]:

$$k_r^2 + k_z^2 = k^2 = \frac{4\pi^2}{\lambda^2} \tag{2.20}$$

However, as Bessel beams have infinitely extended light field structure and infinity energy, they are only theoretical models and cannot be generated in practise [33]. BG beams, which are solutions of the paraxial wave equation, are used as a finite-energy approximation of Bessel beams and they are obtained by the apodization of those beams [35]. The complex amplitude of BG beams is given by [33]:

$$BG_\ell(r, \phi, z) = A_\ell J_\ell(k_r r) e^{-ik_z z} e^{i\ell\phi} e^{\frac{-r^2}{w_0^2}} \tag{2.21}$$

This expression has only one more real term $e^{\frac{-r^2}{w_0^2}}$ than the Bessel beams, which indicates that BG beams have the same phase structure and non-diffraction characteristic of Bessel beams in a finite propagation distance.

2.2.2 OAM Modes in Optical Fibers

OAM modes in optical fibers can be described by the superposition of two degenerated eigenmodes with orthogonal azimuthal dependence. As detailed in [28], HE and EH modes have a pair of degenerated modes with identical radial dependence, but orthogonal azimuthal dependence in the form of $\sin(\ell\phi)$ and $\cos(\ell\phi)$ [28, 30].

The combination of the two degenerated modes with $\sin(\ell\phi)$ and $\cos(\ell\phi)$ azimuthal dependence can lead to a mode with a phase dependence in the form of $e^{i\ell\phi}$ and a basis change from linear to circular polarization [28, 30]. In this sense, the OAM modes supported by the fiber can be determined with the following superpositions [36]:

$$\mathrm{OAM}^{\pm}_{\pm\ell,m} = \mathrm{HE}^{\mathrm{even}}_{\ell+1,m} \pm i\mathrm{HE}^{\mathrm{odd}}_{\ell+1,m} \tag{2.22a}$$

$$\mathrm{OAM}^{\mp}_{\pm\ell,m} = \mathrm{EH}^{\mathrm{even}}_{\ell-1,m} \pm i\mathrm{EH}^{\mathrm{odd}}_{\ell-1,m} \tag{2.22b}$$

where ℓ refers to the azimuthal index, which is also called the OAM order or topological charge; the radial index m refers to the number of concentric radial rings in the intensity field profile; the subscript sign indicates the handedness of the helical phase; and the superscript sign indicates the handedness of the circular polarization [2, 36], as illustrated in Fig. 2.6. The cases when the OAM phase and the circular polarization have the same direction are denoted spin-orbit aligned, as shown in Fig. 2.6(a,c). On the other hand, in Fig. 2.6(b,d), we have the cases when the OAM phase and circular polarization have opposite directions, which is called spin-orbit anti-aligned [2, 28, 30].

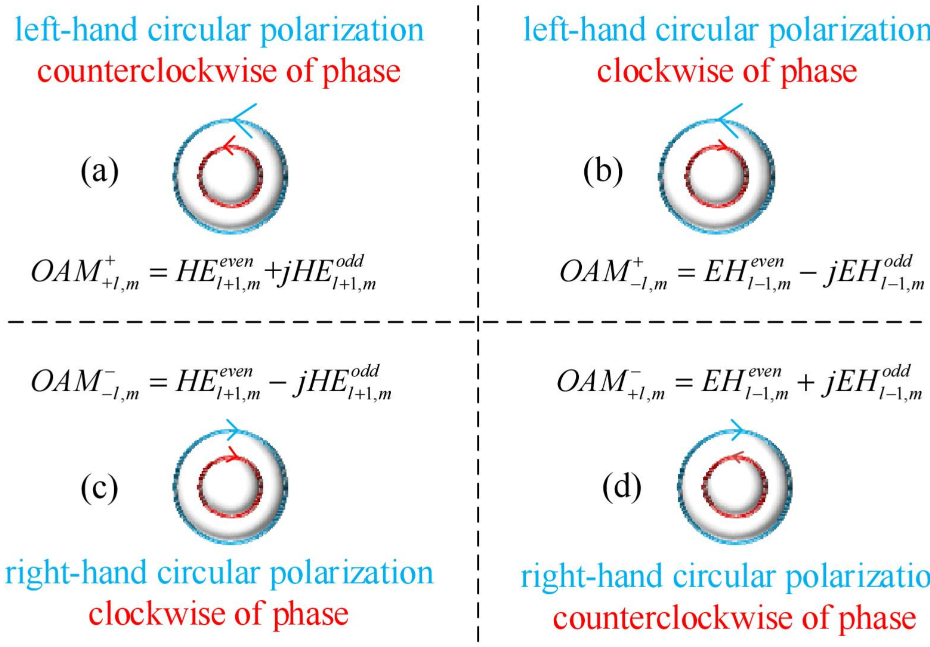

Figure 2.6: OAM phase and circular polarization possible conditions. (a) Spin-orbit aligned OAM with left-hand circular polarization and counterclockwise of phase. (b) Spin-orbit anti-aligned OAM with left-hand circular polarization and clockwise of phase. (c) Spin-orbit aligned OAM with right-hand circular polarization and clockwise of phase. (d) Spin-orbit anti-aligned OAM with right-hand circular polarization and counterclockwise of phase. "Reprinted with permission from [2]". © The Optical Society.

In general, any multimode fiber is able to propagate light with OAM [30]. However, it does not guarantee the stable transmission of these modes. When adjacent modes have very similar effective indices, they can couple during propagation due to perturbations in the guide structure, such as deformations, manufacturing inaccuracies and curvatures [30]. This coupling can eliminate the properties of the OAM modes, i.e.

the helical phase surfaces. As a consequence, in the fiber output we only obtain LP modes composed of several mixed quase-degenerated states, as illustrated in Fig. 2.3 [30].

Digital Signal Processing (DSP) could be used to recover the OAM modes, however, it increases time and power consumption [30]. As an alternative, special fibers have been investigated for stable transmission of OAM modes. A practical criterion usually used to analyse the propagation stability of these modes is $\Delta n_{\text{eff}} > 10^{-4}$. If the effective index difference between adjacent modes is at least this order of magnitude, it is possible to transmit the modes with low coupling over distances on the order of several kilometers [30]. This optical approach to solve the mode coupling problem is specially applied for short-reach optical communications, such as data center applications. For long-haul applications, there are other effects that compromise the data transmission and DSP would be required [30].

Stable propagation of OAM modes over distances on the order of kilometers was first demonstrated using vortex fibers, which is a special type of fiber with a ring-shaped guiding region that separate the effective indices of the OAM modes and reduce the coupling between them [21, 28]. Vortex fibers can have a solid core or an air core. For low-order OAM modes, stable propagation can be obtained using solid-core vortex fibers [21, 30]. However, for higher-order OAM modes, a larger n_{eff} splitting is required [21, 30]. This is reached using air-core vortex fibers. In these fibers, the central air hole provides a larger refractive index contrast, maximizing the number of guided OAM modes [28].

Another special type of fiber that have been considered for stable OAM transmission is the Photonic Crystal Fiber (PCF). PCFs are fibers that have a periodic transverse microstructure with a defect introduced to provide light confinement [9]. Depending on the nature of the defect (solid or hollow), the PCF is called Solid-Core Photonic Crystal Fiber (SC-PCF) or HC-PCF [9]. SC-PCFs, generally, guide light thought total internal reflection between the low index cladding structure and the high index core. The SC-PCF creates the index difference incorporating holes into the cladding glass, causing the effective index "seen" by the mode to be lower than that of the core [9]. HC-PCFs use the bandgap effect to guide light. Due to the periodic structure in the cladding, there is the occurrence of a bandgap analogous to the electronic bandgap in semiconductors. This photonic bandgap in the cladding acts as a loss-free mirror to confine light into the hollow core [9]. The large index difference between the core and the cladding in this type of fiber can maintain a stable propagation of OAM modes. Due to its adjustable parameters, PCFs can offer more flexible design structures to provide unique fiber properties [37]. Various structures, (such as hexagonal, circular, kagome) and materials (such as As_2S_3, SiO_2 and polymer), having promising features have been designed and even fabricated to ensure good transmission quality of OAM modes [37]. In this work, we use a HC-PCF, as it will be detailed in Chapter 3.

2.2.3 OAM Generation and Detection

Light with OAM can be generated using different strategies. Even a laser can generate OAM beams by placing a component in the laser cavity, forcing it to resonate in a specific OAM mode [4]. However, the most common way is to convert a Gaussian beam to a OAM beam using, for example, SPPs, CGH programmed on SLMs, cylindrical lenses, metamaterials, metasurfaces, q-plates and, more recently, integrated devices. SPPs are the easiest way of generating OAM beams. As shown in Fig. 2.7, a rotating step is used to increase the thickness of the SPP with the azimuth angle. SPPs have a high conversion efficiency and they can be used with high power lasers beams, however they can generate only a single OAM beam and they have very tight precision requirements [4].

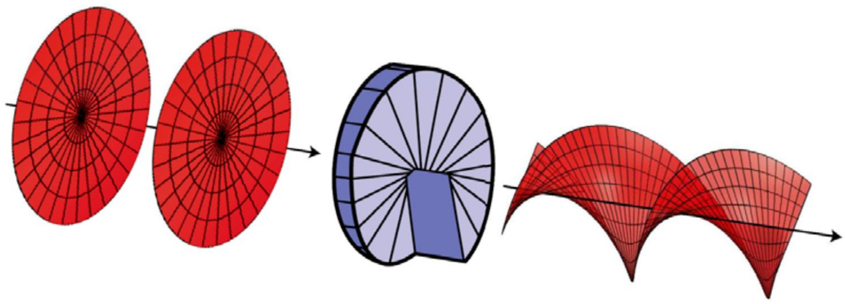

Figure 2.7: Generation of an OAM beam using a SPP. “Adapted with permission from [3]”. © The Optical Society.

The SLM is a liquid crystal device that can be programmed to change the incident beam parameters, such as the beam phase in the transverse plane, to create OAM beams [4]. SLMs can load phase holograms in the form of spiral phase, ℓ-fold forked or binarized ℓ-fold forked grating holograms, as illustrated in Fig. 2.8. Although SLMs can be programmed to generate a wide range of OAM beams, they have some limitations, such as the refreshment image rate, which can be slow for some applications in communications [36]; their energy threshold, making impossible the usage with high power lasers beams; and the relatively expensive cost [4].

The detection of OAM beams can be performed using the reverse process of their generation. For example, an OAM beam with topological charge ℓ illuminating a $-\ell$ forked hologram, produces a plane wave Gaussian beam. Other techniques to detect the topological charge of an OAM beam include the use of interferometry, such as the interferometry with a Gaussian beam or other OAM beams [3, 21]; and passing the OAM beams through apertures, such as a triangular aperture [38–40].

Besides being very bulky and sensitive to misalignment, these free-space techniques also require additional components, such as lenses, to couple the OAM beams into fibers. To achieve more efficient and more compact solutions, OAM generators and detectors have been proposed using integrated devices. In the next section, we discuss

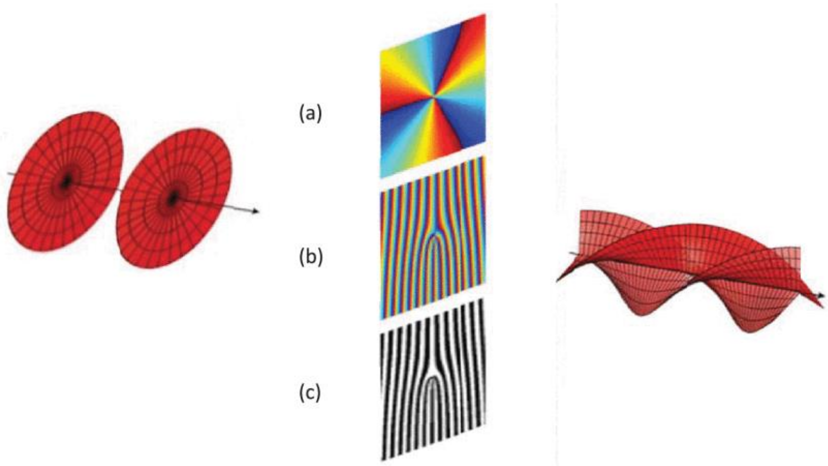

Figure 2.8: Generation of OAM beams using SLMs: a) Spiral phase hologram; b) ℓ-fold forked hologram; c) binarized ℓ-fold forked grating. “Reprinted with permission from [4]” © 2020 IEEE.

the main strategies in the literature to generate and detect OAM beams using integrated couplers.

2.3 Integrated OAM Couplers

The light can be coupled to photonic chips using three types of strategies: edge coupling, out-of-plane coupling and evanescent coupling. In edge coupling, Fig. 2.9(a), the light is coupled to the chip using the lateral facets of the chip. This technique provides high coupling efficiency, high bandwidth and low sensitivity to the light polarization [41]. However, due to waveguide dimensions, edge coupling is very sensitive to misalignment with optical fibers and it requires chip facets with low roughness. In out-of-plane coupling, Fig. 2.9(b), a diffracting element is used to modify the propagation direction of the light. Diffraction gratings are the most widely adopted solution for out-of-plane coupling [41]. They are less sensitive to misalignment and easier to fabricate than edge-coupling solutions, but they usually have narrow optical bandwidth and they are polarization dependent. Evanescent coupling, Fig. 2.9(c), is based on the transfer of power from one waveguide to another by the overlap of the evanescent fields. By changing the distance and coupler length between the waveguides, it is possible to couple any desired fraction of power from one waveguide to another [42].

For OAM generation and detection, solutions based on edge coupling are limited by the fabrication complexity. The currently solutions for this type of coupling are based on either specially-designed integrated waveguides for OAM modes [43] or controlling the phase of a 3D waveguide array [6], as illustrated in Fig. 2.10. The main drawback of OAM modes propagating in integrated waveguides is the radial asymmetry of these waveguides,

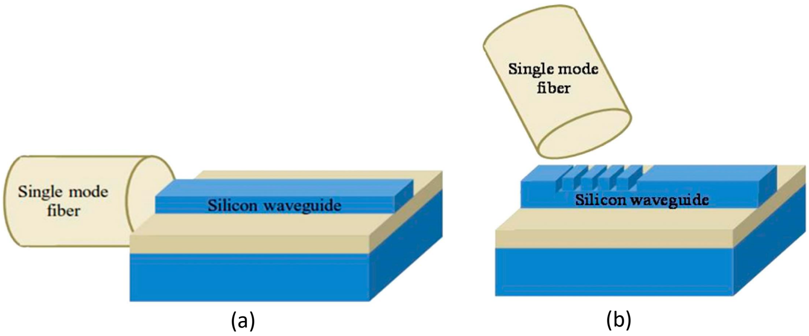

Figure 2.9: Different coupling strategies. (a) Edge coupling. (b) Out-of-plane coupling. (c) Evanescent coupling. “Adapted with permission from [5]”. © 2016 Elsevier.

which compromises the purity of the OAM modes and its propagation stability [30]. The 3D waveguide array proposed in [43] is a relatively wide device and it was designed for free-space applications. For fiber coupling, additional lenses would be necessary. Both approaches require complex fabrication processes.

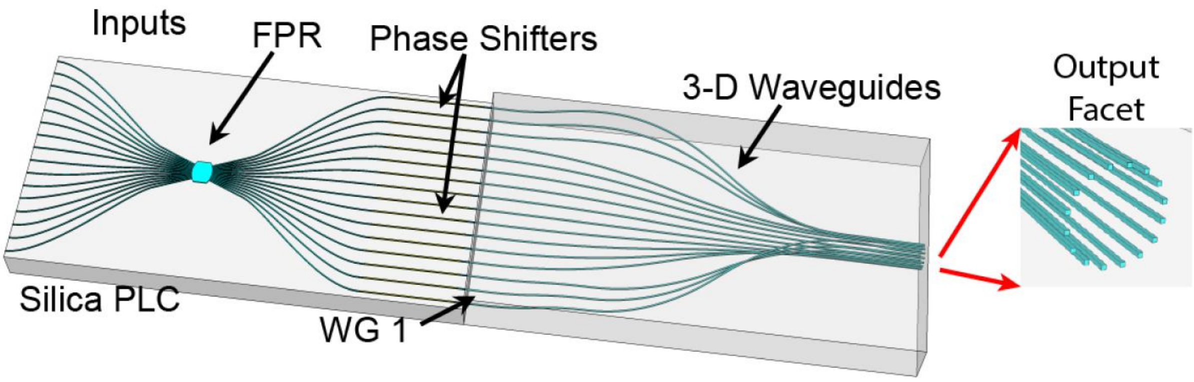

Figure 2.10: Edge OAM coupler based on 3D waveguides. “Reprinted with permission from [6]”. © The Optical Society.

Using out-of-plane coupling, a wide variety of OAM couplers have been proposed. The majority of them for free-space applications. In [7], a circular grating with sixteen inputs, which is capable of generating different OAM states for free-space optical transmission was demonstrated. This device is illustrated in Fig. 2.11. The coupler has an outer radius of 25 µm and the OAM state can be tuned by changing the phase of the thermally-controlled input waveguides.

In [20], a phased array using nanoantennas was developed to generate different OAM states and couple them to free-space. To obtain a more compact OAM coupler, in [19] an angular grating patterned along the inner wall of a microring resonator was proposed. This device was also designed for free-space applications and it has the limitation of OAM order dependence on the resonant wavelength. For fiber transmission, a forked

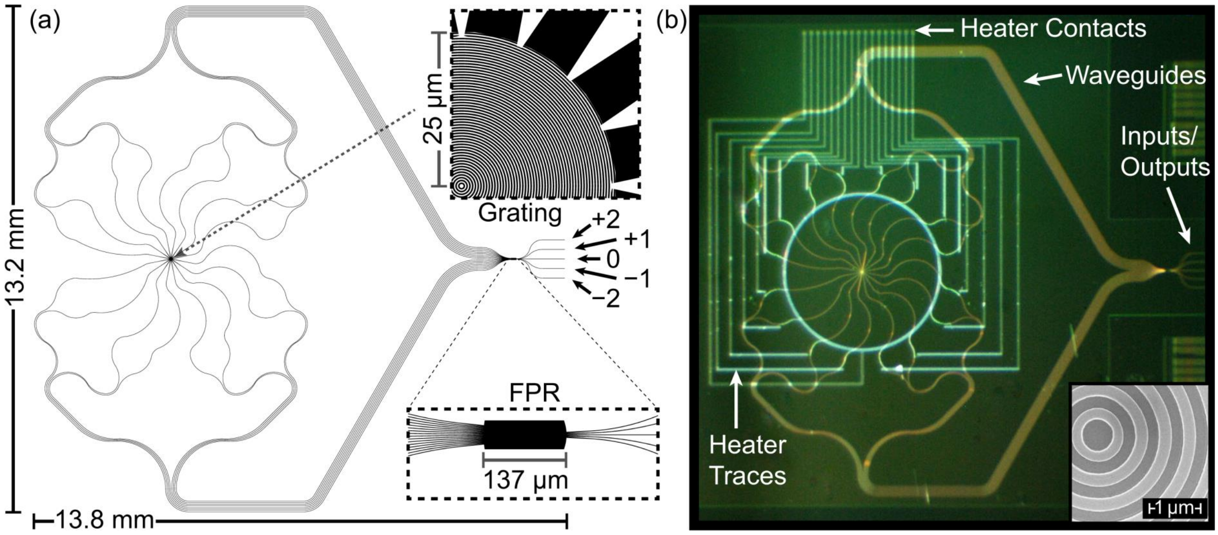

Figure 2.11: Out-of-plane OAM coupler for free-space optical communication. (a) Layout with dimensions of the proposed device. (b) Image of the fabricated device. "Reprinted with permission from [7]". © The Optical Society.

grating coupler using a diffraction grating with a calculated hologram was developed in [22]. This design can directly couple an OAM mode into a vortex fiber, but it couples only a single OAM mode. In [21], an array of grating couplers was developed for the coupling of more OAM modes into a vortex fiber, but due to the array dimensions, an external lens is necessary to focus the beam. A circular OAM generator for OAM fiber coupling using 2D-grating couplers was proposed in [23]. The number of components in the array is limited by the 2D-grating dimensions, which limits the number of OAM modes that can be generated and the modes purity. Finally, in [24], a circular grating coupler for OAM fiber modes was proposed, but for a specially designed fiber. In this work, we aim to design and demonstrate compact OAM couplers that can be capable of generating different OAM modes and directly couple them into optical fibers. We start from the strategies of using an array of compact antennas and a circular grating to generate the OAM fiber modes. Then, we explore the use of topology optimization for the design of OAM couplers. In the next chapter, we present the proposed devices, detailing their design process and the simulation results.

Chapter 3

Design and Simulation of OAM Couplers

In this Chapter, we present the design process of our proposed OAM couplers. We start analysing the supported OAM modes by our multimode fiber, which are used as the reference modes in the couplers' design. The proposed couplers are then presented and detailed, showing design considerations and simulation results.

3.1 OAM Fiber Modes

The OAM fiber modes are analysed in a HC-PCF available in the LCO at Unicamp. The HC-PCF used is a 7-cell Hollow-Core Photonic Bandgap Fiber (HC-PBGF) fabricated by Corning. This fiber was also used in [44] and, as described by the author, a Scanning-Electron Microscope (SEM) image (Fig. 3.1) was used to estimate its geometric parameters as the air-core-diameter of 16 µm, the cladding pitch of 4.9 µm and the air-fill fraction of 92%.

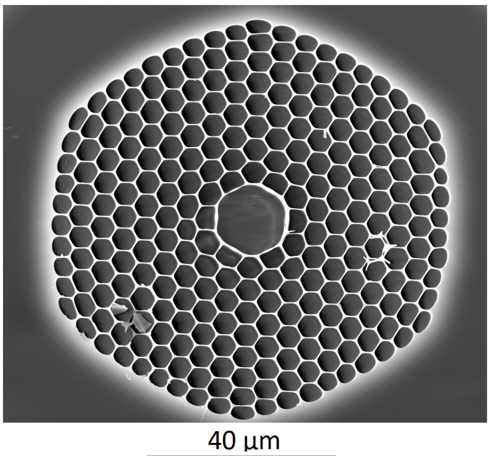

Figure 3.1: HC-PBGF SEM image.

The SEM image and the geometric parameters were used to perform a modal analysis using the FEM solver provided by COMSOL Multiphysics [1]. FEM solves Maxwell's equations by the division of the simulation domain into smaller subdomains, in a process called meshing [45]. This simplifies the field equations into an algebric system of equations which are then solved for their eigenvalues [45]. As a result, we obtain the supported core-guided modes of this fiber at 1550 nm. In Table 3.1 we can see the obtained fundamental modes and Higher-Order Modes (HOM) of this fiber and their respective effective index (n_{eff}).

Table 3.1: Simulation results of the supported core-guided modes of the HC-PBGF at 1550 nm.

Fundamental modes	HE_{11}^{x}	HE_{11}^{y}		
n_{eff}	0.997 76	0.997 76		
Higher-order modes	HE_{21}^{even}	HE_{21}^{odd}	TM_{01}	TE_{01}
n_{eff}	0.994 57	0.994 57	0.994 48	0.994 31

The electric field intensity and polarization direction for these modes can be seen in Fig. 3.2. The superscripts x and y indicate the polarization axis, while the superscripts *even* and *odd* refer to the parity symmetry of the polarization lines.

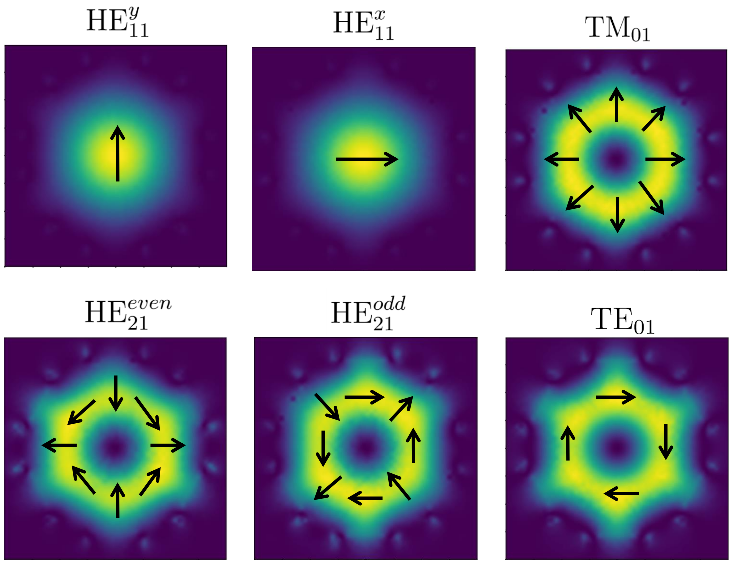

Figure 3.2: HC-PBGF core modes. Electric field intensity and polarization.

The HOMs supported by this fiber are the ones that compose the set of LP_{11} modes in the scalar approximation, for that reason they are called LP_{11}-like modes [9, 30].

[1]https://br.comsol.com/

Based on these supported core-guided modes, we can recover some spin-orbit aligned OAM modes using Eq. 2.22a. Starting from the $HE_{1,1}$ modes, we can obtain the $OAM^{+}_{0,1}$ and $OAM^{-}_{0,1}$ modes, differing by the circular polarization direction: left-handed and right-handed, respectively. Starting from the $HE_{2,1}$ modes we can obtain the $OAM^{+}_{1,1}$ mode, which has counterclockwise OAM phase and left-hand circular polarization, and the $OAM^{-}_{-1,1}$ mode, which has clockwise OAM phase and right-hand circular polarization.

The $OAM^{+}_{0,1}$, $OAM^{+}_{1,1}$ and $OAM^{-}_{-1,1}$ modes are used as the modal basis reference for the couplers' design. For simplification, as all of these modes have only one radial ring, we will call them from here on as OAM_0, OAM_1 and OAM_{-1} modes, respectively. The electric field intensity ($|E|^2$) and x-component (E_x) phase profiles for those modes can be seen in Fig. 3.3.

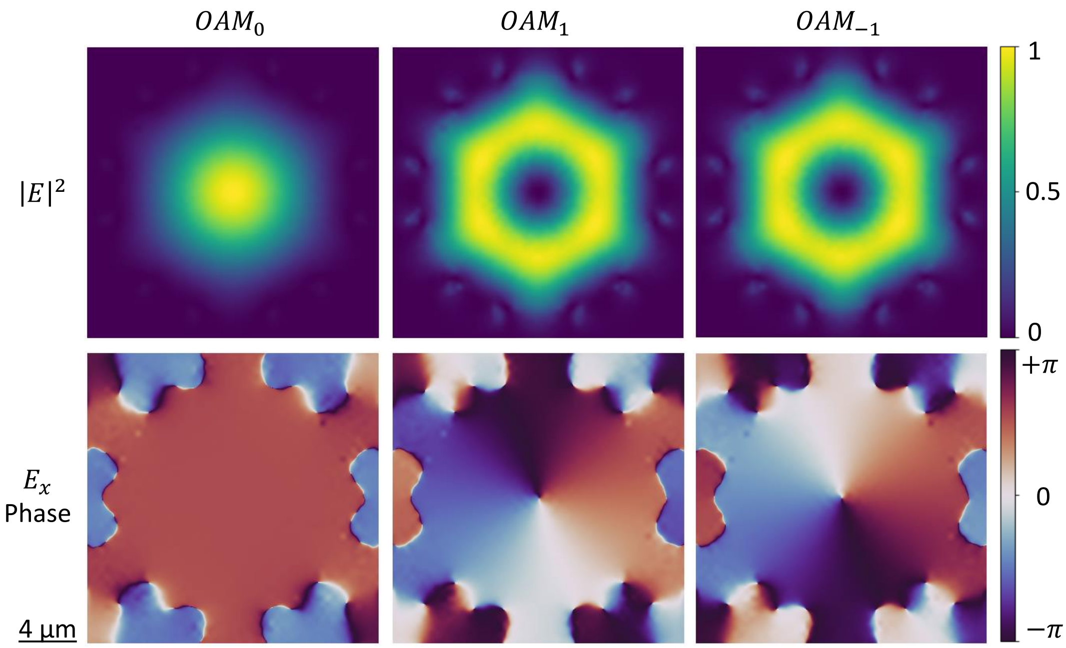

Figure 3.3: Simulation results of $|E|^2$ and E_x phase profile for OAM fiber modes.

As expected, we can see the OAM_0 fiber mode with a Gaussian intensity profile and a constant phase front. We can also observe that the OAM_1 fiber mode is ring-shaped with an optical singularity in the center of the intensity profile and a counterclockwise phase shift from $-\pi$ rad to $+\pi$ rad in the phase front profile. Finally, the OAM_{-1} mode differs from the OAM_1 by its opposite phase shift direction.

3.2 OAM Coupler using an Antenna Array

The first proposed approach to design an OAM coupler consists in using an array of compact antennas with dimensions corresponding to the dimensions of the OAM fiber modes. Each antenna is responsible to generate a part of the beam intensity and a specific phase in a way that the combination of different phase shifts excites a selected OAM fiber mode. As the fiber core radius is 8 µm, the antennas required to compose the proposed coupler must be much more compact than this value. The antenna developed in [46] satisfies this requirement, being an interesting option. It has a size of only 1.78 µm × 1.78 µm, which allows us to place up to eight antennas in the proposed array. This antenna is illustrated in Fig. 3.4.

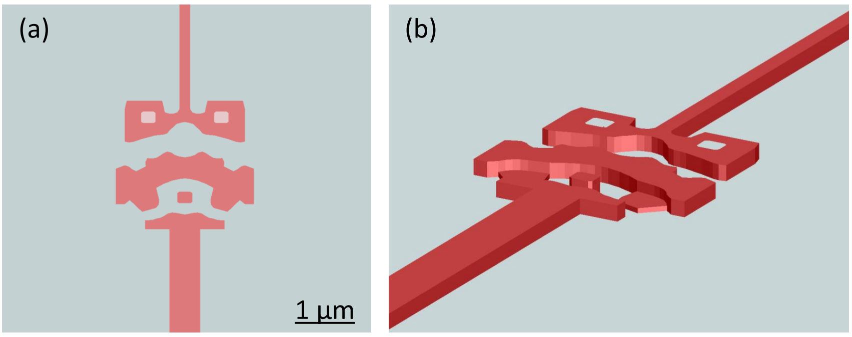

Figure 3.4: Compact antenna. (a) Top view and (b) perspective view.

To analyse the antenna performance, we simulated it in the 3D-FDTD solver provided by Lumerical Inc [2]. Besides providing direct time and space solutions for the Maxwell's equations in complex geometries, the FDTD method can also give other useful quantities, such as the frequency response, the Pointing vector and the transmission/reflection [47]. The design parameters were: 220 nm-SOI platform with a 2 µm Buried Oxide (BOX) layer, 2 µm Top Oxide (TOX) layer, 150 nm step-etch and 450 nm width for the input waveguide. The simulation volume was 6 µm × 6 µm × 6 µm with a 20 nm mesh and a 5 nm mesh refinement in the antenna volume. The antenna is positioned in the center of the simulation volume, thus it also includes the BOX, the TOX, a portion of the substrate and a monitor in a slice 2 µm above the antenna. A Perfectly Matched Layer (PML) was used as the boundary condition to absorb all the propagating waves in the edge of the simulation volume [48].

Using a mode source at the antenna input waveguide, a TE mode, at 1550 nm, propagates in the waveguide and, as a result, a linear polarized beam is emitted by the antenna. The results of the emitted beam are taken in the slice 2 µm above the antenna. When the antenna is aligned with the y-axis, the electric field is higher in the x-component, as we can see in Fig. 3.5(a). On the other hand, when the antenna is aligned with the x-axis, the electric field is higher in the y-component, as we can see in Fig. 3.5(b).

As described in section 3.1, the OAM fiber modes have circular polarization, i.e. same electric field intensity in both x and y components. To contribute equally in both polarizations, eight antennas are disposed in a circular array with the antennas pointing to the center. The proposed array can be seen in Fig. 3.6. The array radius

[2]https://www.lumerical.com/products/fdtd/

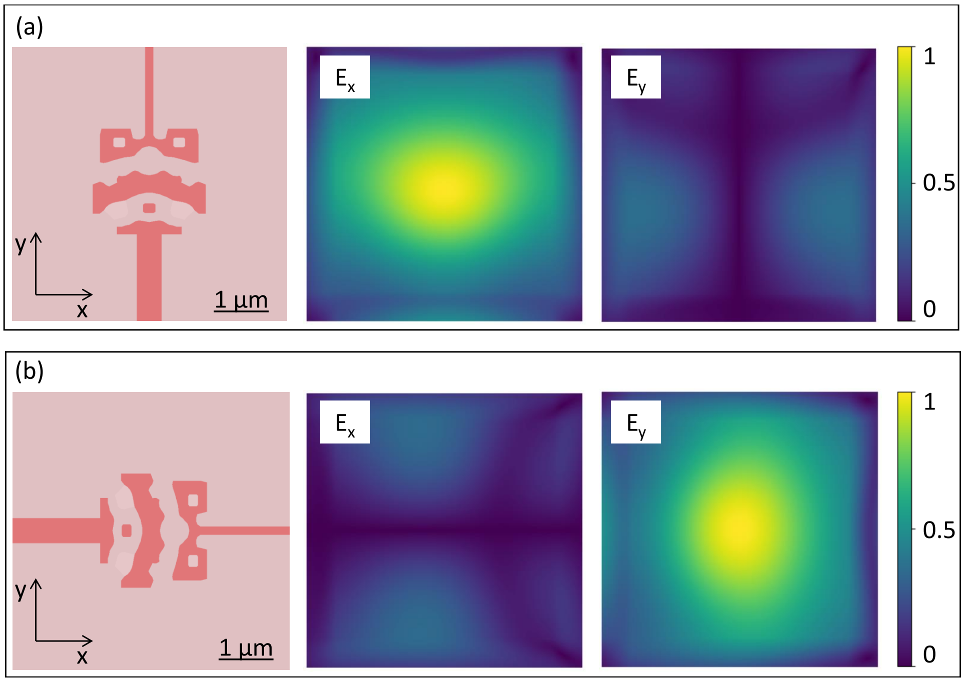

Figure 3.5: Electric field results from the antenna simulation. (a) antenna aligned with the y-axis and (b) antenna aligned with the x-axis.

is here defined as the distance between the antenna input and the center of the array. Different values of array radius were analysed, from 5 µm (the minimum value allowed by fabrication constraints) to 8 µm (the fiber air-core-radius).

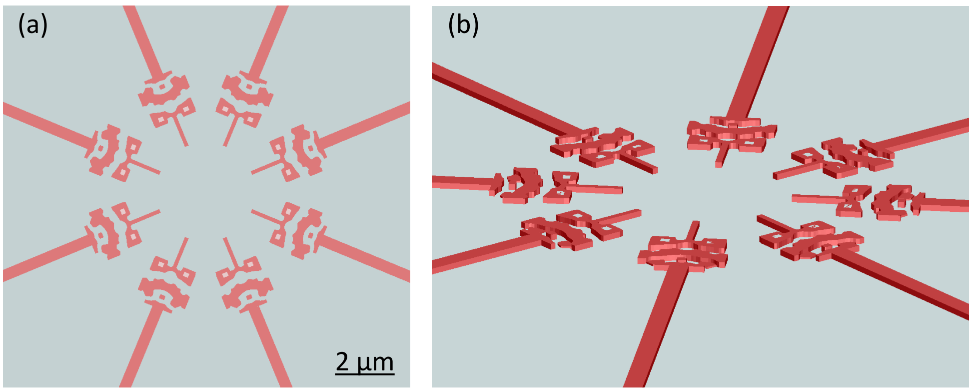

Figure 3.6: Proposed OAM coupler using an antenna array. (a) Top view and (b) perspective view.

For the array simulation, the simulation parameters were modified to satisfy computational requirements. The simulation volume was increased to 20 µm × 20 µm × 6 µm with a 20 nm mesh and a 10 nm mesh refinement in each antenna volume. A mode source is used in each input waveguide and a monitor, in a slice 2 µm above the array, is used to analyse the emitted beam. The phase of each mode source is changed according to the OAM mode to be generated. For OAM_0, the phase is the same for all antennas. For OAM_1, the phase in each antenna is increased by $\frac{\pi}{4}$ rad in the counterclockwise direction, accomplishing a 2π rad phase shift. For OAM_{-1}, the phase in each antenna is also increased by $\frac{\pi}{4}$ rad, but in the clockwise direction. The electric field results, at 1550 nm, of the antenna array with a radius of 5 µm for these three OAM modes can be seen in Fig. 3.7.

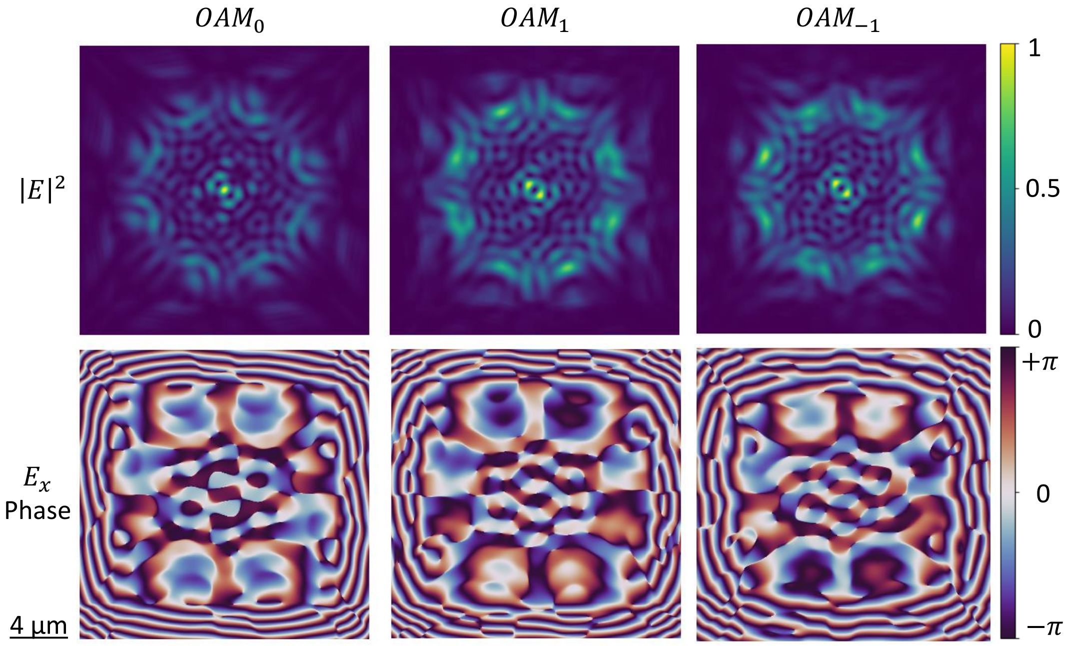

Figure 3.7: $|E|^2$ and E_x phase results of the antenna array with a radius of 5 µm simulated at 1550 nm.

As we can see in Fig. 3.7, to generate the OAM_0 mode, the combination of the beams emitted by the antennas forms a beam with a higher intensity in the center of the array and a constant phase in each antenna position. On the other hand, to generate the OAM_1 and OAM_{-1} modes, the combination of the antennas' beams forms a beam with a higher intensity in a ring pattern and the phase in the position of each antenna changes in the counterclockwise and clockwise direction, respectively. It is also noticeable, for all three modes, that an undesirable interference pattern occurs outside the antennas' positions in both intensity and phase profile. This happens due to the antenna directivity. At this height, 2 µm, the scattered field of each antenna is enough to generate a non-negligible interference. For a more detailed analysis of this interference pattern, we simulate the array with 1, 2 and 4 antennas, as we can see in Fig. 3.8 for the OAM_1 mode.

As we can see in Fig. 3.8, when we increase the number of antennas, the combination of the scattered field from each antenna generates some interference fringes and an interference pattern in the center of the array, which can impact the device performance. We can also see in Fig. 3.8(a) some discontinuities in the antenna field profile, especially in its phase profile. These discontinuities can be attributed to the mesh. In this case the antenna was simulated in an angle of 22.5° in relation to the x-axis while the mesh lines are parallel to the x and y axes. Simulating the antenna aligned with the x-axis, we can see in Fig. 3.9 that the discontinuities were reduced. To simulate the antenna array

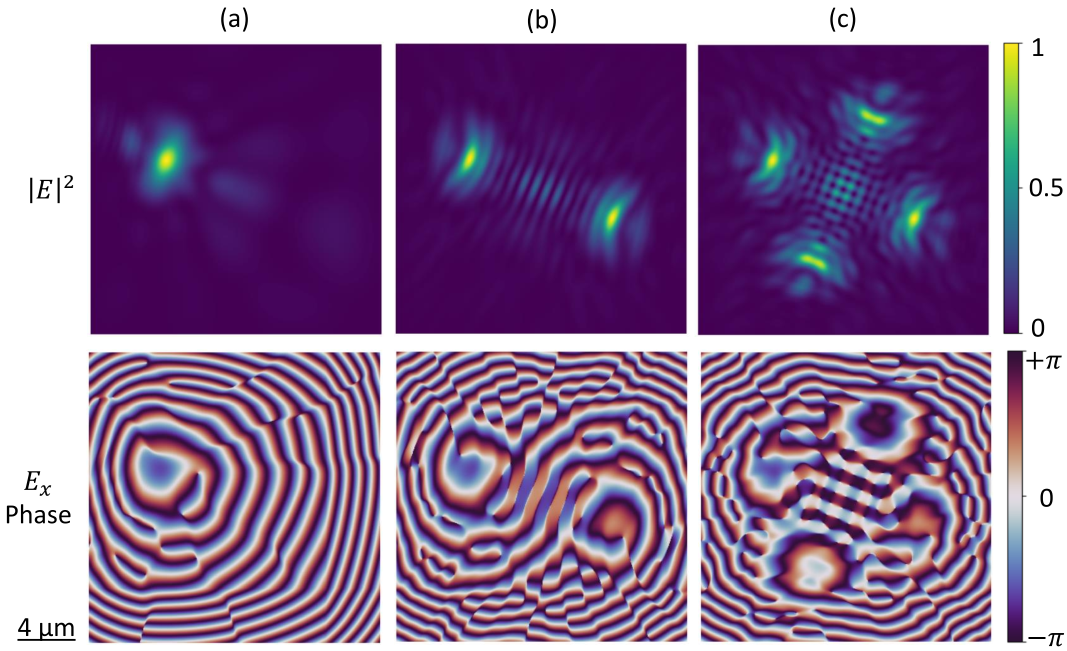

Figure 3.8: $|E|^2$ and E_x phase results of the antenna array with a radius of 5 µm simulated at 1550 nm for the OAM_1 mode with (a) 1 antenna, (b) 2 antennas and (c) 4 antennas.

with eight antennas, we will always have some antennas that are not aligned with the axes, then, to maintain the symmetry, we simulate the array with all antennas in a angle of 22.5° in relation to an axis. The discontinuities can also be reduced by further refining the mesh, however the mesh refinement is already at the limit of our computational resources (CPU: Intel Xeon E5-2650 with 6 cores, 12 threads and 2 GHz; RAM: 128 GB).

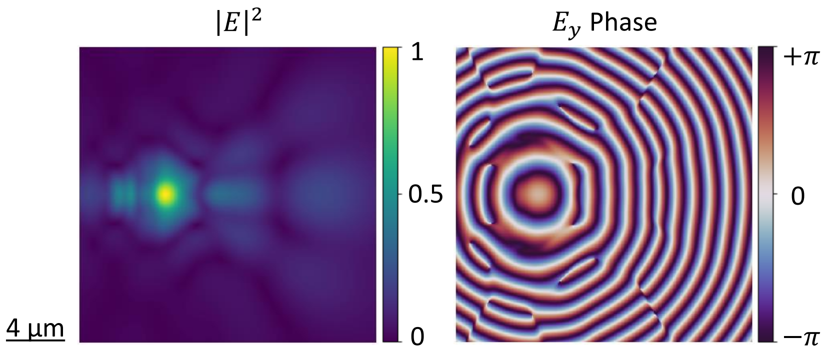

Figure 3.9: $|E|^2$ and E_y phase results of one antenna aligned with the x-axis and simulated at 1550 nm.

The coupling performance is analysed by the calculation of the overlap integral between the generated OAM modes and the OAM fiber modes. The overlap integral is calculated according to the following equation [49]:

$$C = \left| \Re \left\{ \frac{\left(\int \vec{E}_1 \times \vec{H}_2^* \cdot \mathrm{d}\vec{S}\right)\left(\int \vec{E}_2 \times \vec{H}_1^* \cdot \mathrm{d}\vec{S}\right)}{\int \vec{E}_1 \times \vec{H}_1^* \cdot \mathrm{d}\vec{S}} \right\} \frac{1}{\Re\left\{\int \vec{E}_2 \times \vec{H}_2^* \cdot \mathrm{d}\vec{S}\right\}} \right| \tag{3.1}$$

where $\vec{E}_1$ and $\vec{H}_1$ are the electric and magnetic fields, respectively, from the generated beam by the proposed device, while $\vec{E}_2$ and $\vec{H}_2$ are the electric and magnetic fields from the OAM fiber modes. C is the overlap result and the surface integrals are calculated in an area of $20\,\mu\mathrm{m} \times 20\,\mu\mathrm{m}$ discretized in a matrix with 1001 rows and 1001 columns. In Appendix A, we discuss the implementation of the algorithm to perform this calculation and its validation by comparing with the overlap calculation in a commercial software.

For the proposed array, we have simulated and calculated the overlap for different values of array radius. The result obtained of mode overlap in function of array radius for the three OAM modes can be seen in Fig. 3.10.

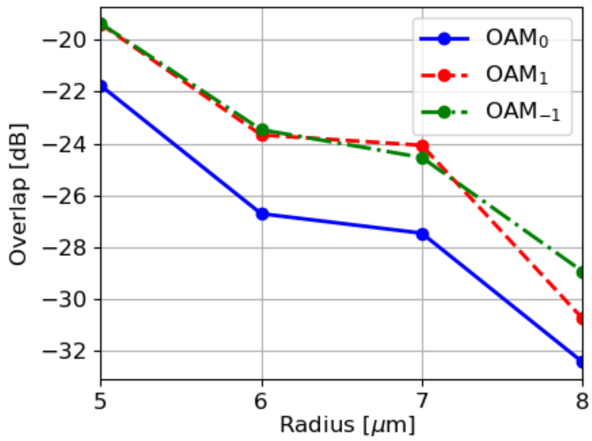

Figure 3.10: Mode overlap in function of radius for the antenna array simulated at 1550 nm.

As we can see, the results for the OAM_1 and OAM_{-1} modes are better than for the OAM_0 mode in all cases, this can be attributed to the circular arrangement that makes more efficient the coupling with a ring-shaped beam than with a Gaussian beam. By symmetry, the OAM_1 and OAM_{-1} modes should have the same results, but that was not the case because the fiber simulation was based in a SEM image. In practical, the fiber is not perfectly symmetric and it can have some defects. The radius of 5 μm provided the best results of mode overlap for all modes. For this radius the values obtained were: -21.76 dB for OAM_0, -19.39 dB for OAM_1 and -19.37 dB for OAM_{-1}. The overlap between the generated OAM mode and other OAM fiber modes was below -63.38 dB in the case of the OAM_1(or OAM_{-1}) with the OAM_0, and below -27.52 dB in the case of the OAM_1 with the OAM_{-1}. These results are summarized in Table 3.2.

The the proposed OAM coupler can be used for a two-mode transmission with very low intermodal crosstalk. Considering the transmission of the OAM_1 (or OAM_{-1})

Table 3.2: Overlap between fiber modes and antenna array with a radius of 5 µm at 1550 nm.

	OAM_0 Fiber (dB)	OAM_1 Fiber (dB)	OAM_{-1} Fiber (dB)
OAM_0 antenna array	-21.76	-71.29	-64.01
OAM_1 antenna array	-63.38	-19.39	-27.89
OAM_{-1} antenna array	-80.16	-27.52	-19.37

mode with the OAM_0 mode, the crosstalk is in the range of -40 dB. A three-mode transmission is also possible, however with a worse intermodal crosstalk due to the -8 dB crosstalk between the OAM_1 and OAM_{-1} modes.

As described in [46], the compact antenna is broadband, covering a wide wavelength range from 1300 nm to 1700 nm, however it has a higher transmission efficiency at shorter wavelengths, which starts to decrease after 1500 nm. The transmission spectrum was also obtained from the FDTD simulations and the result in a height 2 µm above the antenna can be seen in Fig. 3.11.

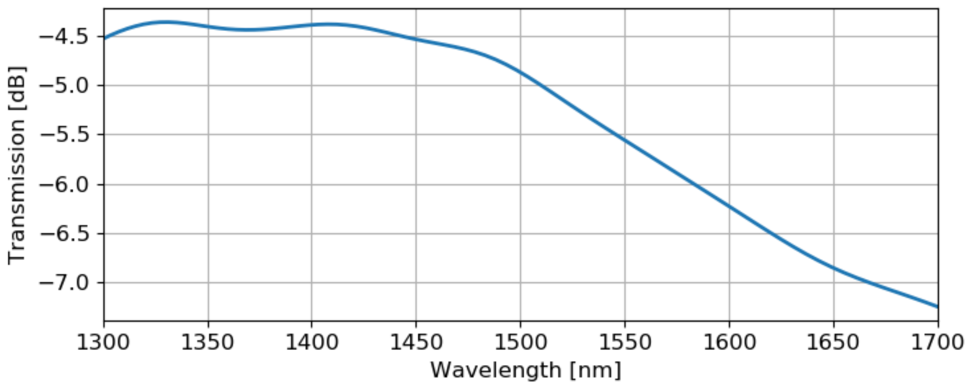

Figure 3.11: Simulation result of the antenna transmission spectrum.

Simulating the antenna array at 1470 nm, the electric field results obtained can be seen in Fig. 3.12. As we can see, the change in the wavelength also resulted in a change in the antenna directivity. We see a higher constructive interference among the beams of each antenna and less scattered field in relation to the results at 1550 nm.

The impact in the device performance is evaluated performing a new modal analysis of the fiber for this new wavelength and calculating the new overlap values between the OAM fiber modes and the generated beams. For this condition, the results obtained of mode overlap in function of array radius for the three OAM modes can be seen in Fig. 3.13.

As we can see, at 1470 nm we obtained better results for all OAM modes, about 5 dB greater than at 1550 nm. The radius of 5 µm also provided the best results at this wavelength. For this radius, we obtained a mode overlap of -16.32 dB for OAM_0,

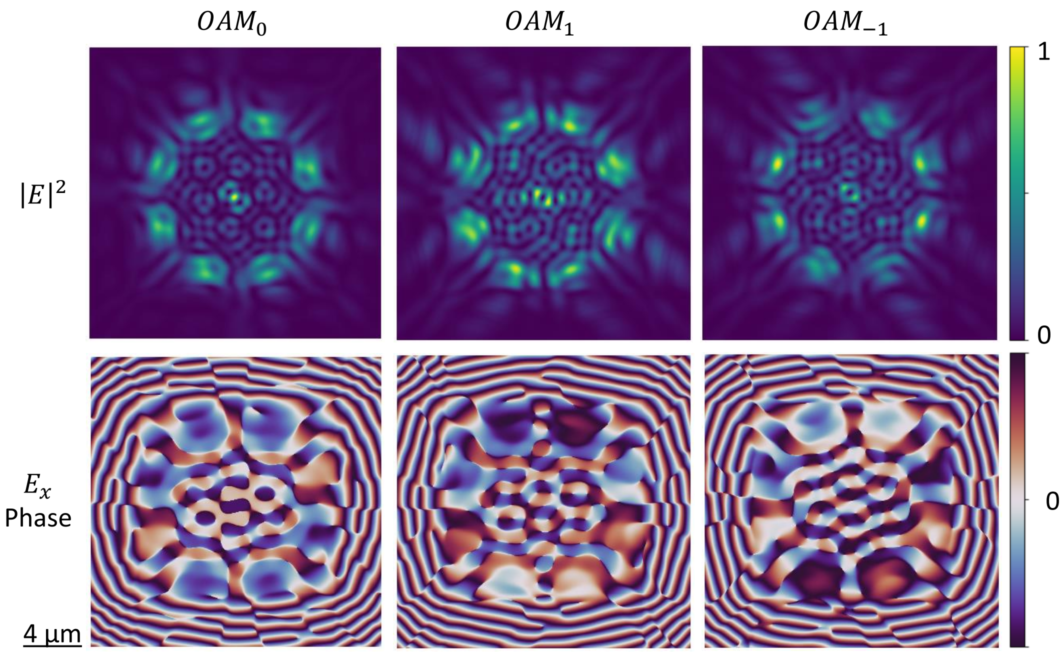

Figure 3.12: $|E|^2$ and E_x phase results of the antenna array with a radius of 5 µm simulated at 1470 nm.

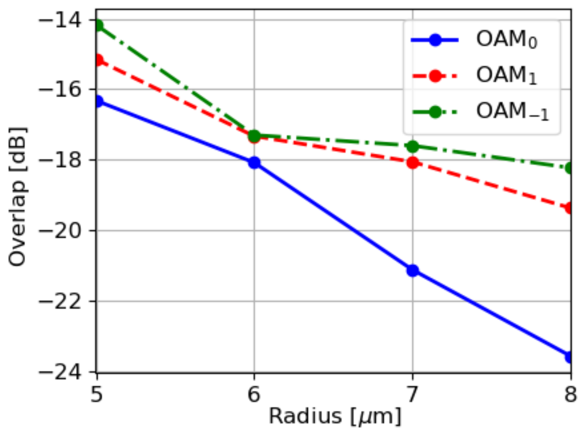

Figure 3.13: Mode overlap in function of radius for the antenna array simulated at 1470 nm.

-15.15 dB for OAM_1 and -14.17 dB for OAM_{-1}. The overlap between the generated OAM mode and other OAM fiber modes was below -40.92 dB in the case of the OAM_1 (or OAM_{-1}) with the OAM_0, and below -21.73 dB in the case of the OAM_1 with the OAM_{-1}. These results are summarized in Table 3.3.

Although we obtained better results of mode transmission, the crosstalk was impacted and worse values were obtained at this wavelength: about -25 dB for a two-mode transmission and about -6 dB for a three-mode transmission.

As we can see, the device can operate in both wavelengths analysed as long as it meets the requirements of the optical system. Besides that, it could generate 7 OAM modes (OAM_{-3}, OAM_{-2}, OAM_{-1}, OAM_0, OAM_1, OAM_2 and OAM_3) for the coupling with a fiber that supports all these modes. In this work, as our current library of photonic components

Table 3.3: Overlap between fiber modes and antenna array with a radius of 5 µm at 1470 nm.

	OAM_0 Fiber (dB)	OAM_1 Fiber (dB)	OAM_{-1} Fiber (dB)
OAM_0 antenna array	−16.32	−45.24	−40.92
OAM_1 antenna array	−41.88	−15.15	−21.73
OAM_{-1} antenna array	−88.54	−22.12	−14.17

(splitters, SMF couplers, etc.) are designed to operate at the C-band (1530 nm–1565 nm), we fabricated and characterized the device operating at 1550 nm. The test structures designed for the characterization of this OAM coupler and the achieved experimental results are described in Chapter 4.

In the following sections, in a way to improve the coupling efficiency, we explore the design of OAM couplers using other approaches.

3.3 OAM Coupler using a Circular Grating

Another approach used for the design of OAM couplers is a circular grating with multiple input waveguides, as illustrated in Fig. 3.14. Assigning a specific phase shift in each input, the combination of the beams can generate the desired OAM mode. This approach was used in [7] for free space optical communication and in [24] for a specific ring-core fiber. In this work, the circular grating coupler is designed based on the OAM fiber modes supported by our hollow-core fiber, as described in section 3.1.

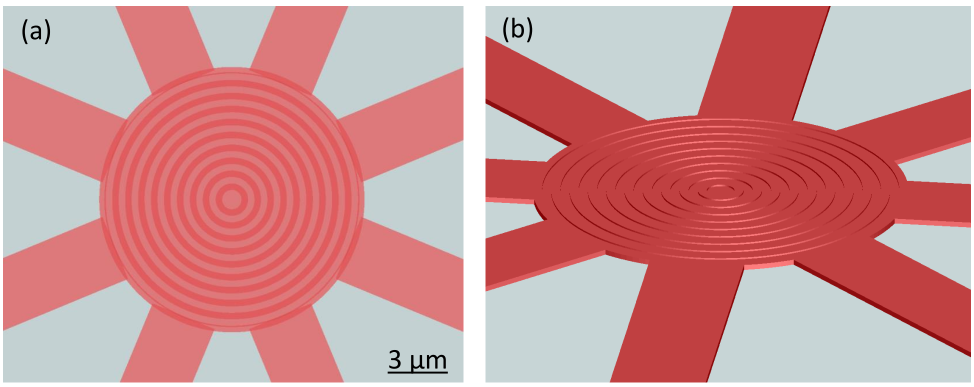

Figure 3.14: Proposed OAM coupler using a circular grating. (a) Top view and (b) perspective view.

This OAM coupler is designed based on the same 220 nm-SOI platform used for the antenna array design, but with a step etch of 70 nm. The circular grating also has eight input waveguides with a width of 3 µm. All waveguides are adiabatically tapered to connect with the standard 0.45 µm-wide PIC waveguides. To determine the grating parameters, we start from an analytical analysis, where the grating period is calculated according to the following equation [50]:

$$\Lambda = \frac{\lambda}{n_{\text{eff}} - \sin\theta} \tag{3.2}$$

where Λ is the period, λ is the wavelength, n_{eff} is the effective index and θ is the fiber angle. The fiber angle is normal to the device surface, then θ is 0°. The duty cycle was started with 0.5 for the first design. The n_{eff} was determined as 2.682 by modal simulation in Lumerical Mode Solution [3]. With these parameters and considering the operating wavelength of 1550 nm, a grating period of 578 nm is obtained.

The circular grating was simulated in Lumerical's FDTD solver with the same simulation parameters used in the antenna array simulation, except for the mesh refinement. For this device a mesh refinement of 50 nm in the grating region is enough. The circular grating was also simulated for different values of outer radius. The electric field results obtained with these parameters and an outer radius of 6 µm can be seen in Fig. 3.15.

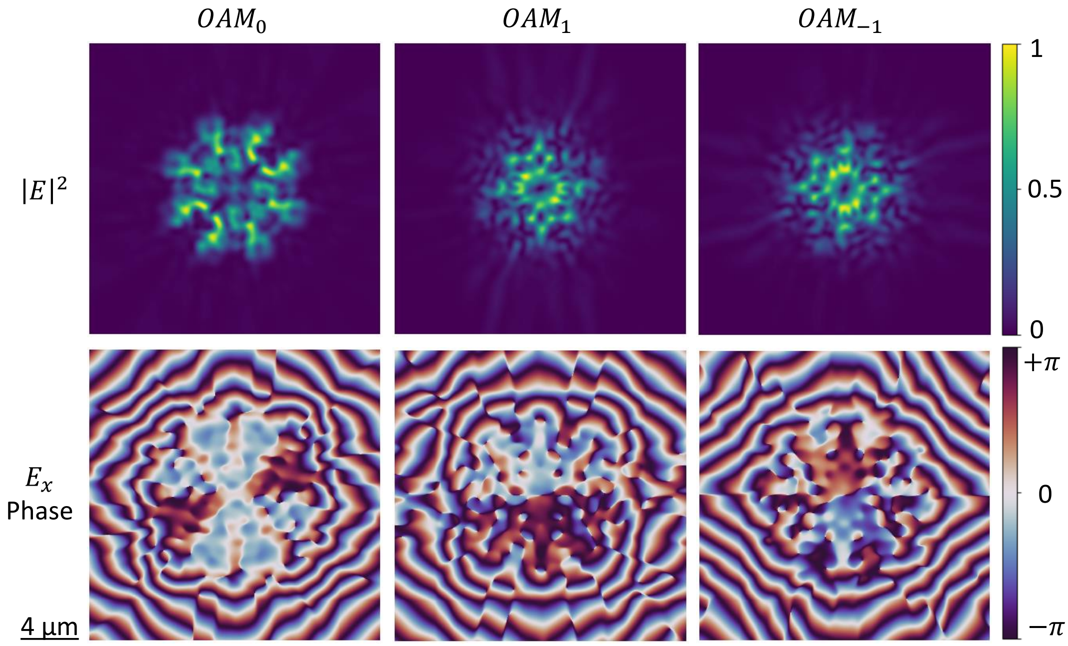

Figure 3.15: $|E|^2$ and E_x phase results of the circular grating simulated at 1550 nm with duty cycle = 0.5, Λ = 578 nm and outer radius = 6 µm.

Calculating the overlap integral with the fiber modes for different values of outer radius, we obtained the results of Fig. 3.16. As we can see, the overlap for the OAM_0 mode has significantly improved in relation to the results of the antenna array (about 11 dB), but for the OAM_1 and OAM_{-1} modes there was just a slight improvement (about 3 dB). This large difference can be attributed to the intensity profile of the emitted beam. As we can see in Fig. 3.15, the combination of the beams, that comes from the waveguides

[3]https://www.lumerical.com/products/mode/

and diffracts in the grating, converge to a more centered beam. This contribute to a higher coupling with a Gaussian beam than with a ring-shaped beam.

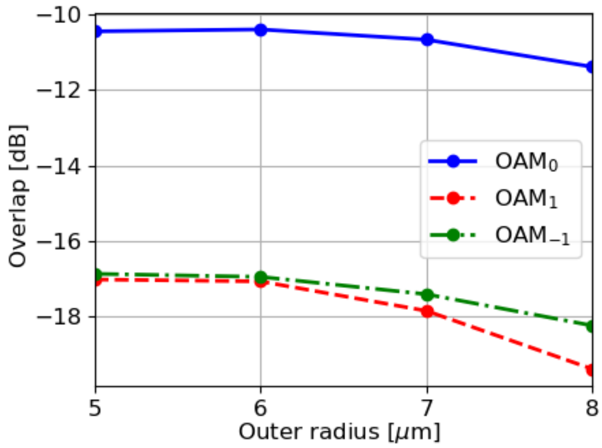

Figure 3.16: Mode overlap in function of outer radius for the circular grating simulated at 1550 nm with duty cycle = 0.5 and $\Lambda = 578$ nm.

The outer radius of 6 μm provided the best results of mode overlap. For this outer radius, we obtained −10.39 dB for OAM_0, −17 dB for OAM_1 and −16.95 dB for OAM_{-1}. The intermodal overlap was below −54.73 dB for the OAM_0 mode with the other modes, and below −24.68 dB for the OAM_1 mode with the OAM_{-1} mode. These values are listed in Table 3.4.

Table 3.4: Overlap between fiber modes and circular grating simulated at 1550 nm with duty cycle = 0.5, $\Lambda = 578$ nm and outer radius = 6 μm.

	OAM_0 Fiber (dB)	OAM_1 Fiber (dB)	OAM_{-1} Fiber (dB)
OAM_0 circular grating	−10.39	−54.73	−56.12
OAM_1 circular grating	−63.83	−17.00	−24.68
OAM_{-1} circular grating	−79.71	−25.00	−16.95

As previously observed, this device is much more efficient for the OAM_0 transmission, almost 7 dB, than for the other modes. To improve the device performance for the OAM_1 and OAM_{-1} modes, we performed an optimization of the grating parameters using the algorithm of Particle Swarm Optimization (PSO) integrated to the Lumerical's FDTD solver [4]. PSO is an evolutionary optimization algorithm that was initially inspired by the social behavior of flocks of birds and schools of fishes, but now it is more similar to a swarm of mosquitoes due to the irregular movements of the particles in the problem space [51]. During the optimization, a random population of particles flies through the problem hyperspace with different velocities. The velocities of each particle are then

[4]https://support.lumerical.com/hc/en-us/articles/360034922953-Optimization-utility

stochastically adjusted during the iterations according to the historical best position of the particle and its neighborhood, evolving to an optimal or near-optimal solution [51]. In our problem, the duty cycle and period were used as the optimization parameters and the transmission efficiency as the Figure of Merit (FOM). As a result, we obtained the following optimized values: duty cycle = 0.46 and $\Lambda = 566\,\mathrm{nm}$.

Simulating and calculating the overlap of the circular grating with these parameters and for different outer radius, we obtained the results of Fig. 3.17. The electric field results for an outer radius of 8 µm is shown in Fig. 3.18.

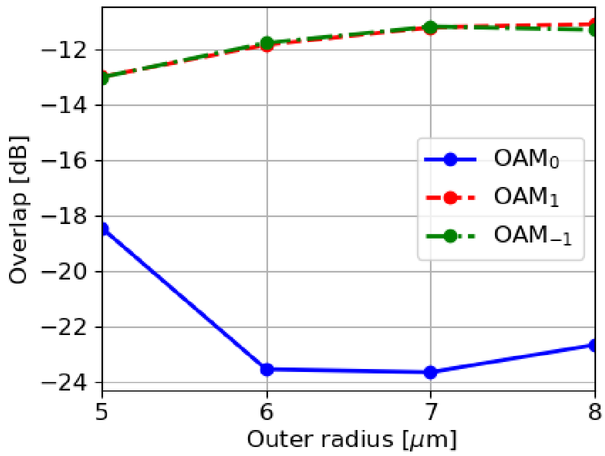

Figure 3.17: Mode overlap in function of outer radius for the circular grating simulated at 1550 nm with duty cycle = 0.46 and $\Lambda = 566\,\mathrm{nm}$.

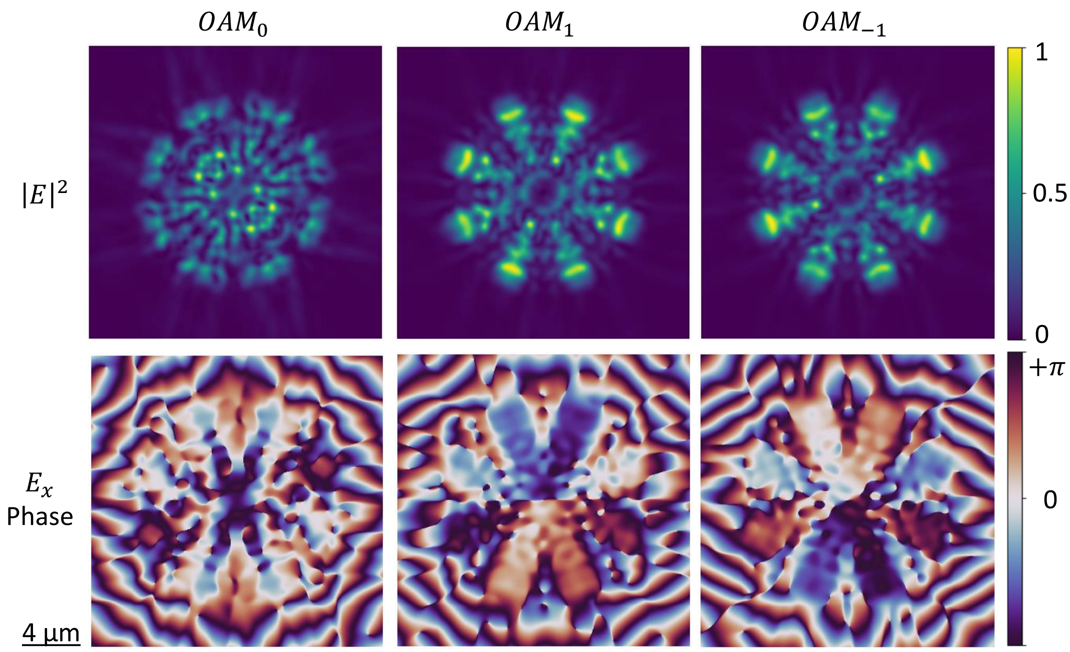

Figure 3.18: $|E|^2$ and E_x phase results of the circular grating simulated at 1550 nm with duty cycle = 0.46, $\Lambda = 566\,\mathrm{nm}$ and outer radius = 8 µm.

As we can see in Fig. 3.17, the overlap results for the OAM_1 and OAM_{-1} modes have significantly improved at the expense of worse results for the OAM_0 mode. This can again be attribute to the intensity profile of the emitted beams. With this parameters, the circular grating emits a beam with a higher intensity near the input waveguides, as we can see in Fig. 3.18. This contribute to a higher coupling with a ring-shaped beam than with a Gaussian beam. The outer radius of 5 µm provided the best overlap result for the OAM_0 mode, while the outer radius of 8 µm provided the best results for the OAM_1 and OAM_{-1} modes. For the latter, we obtained −22.67 dB for OAM_0, −11.08 dB for OAM_1 and −11.28 dB for OAM_{-1}. The intermodal overlap was below −56.1 dB for the OAM_0 mode with the other modes, and below −18.51 dB for the OAM_1 mode with the OAM_{-1} mode. This corresponds to an intermodal crosstalk of −33.43 dB for a two-mode transmission and −7.23 dB for a three-mode transmission. These values are listed in Table 3.5.

Table 3.5: Overlap between fiber modes and circular grating simulated at 1550 nm with duty cycle = 0.46, Λ = 566 nm and outer radius = 8 µm.

	OAM_0 Fiber (dB)	OAM_1 Fiber (dB)	OAM_{-1} Fiber (dB)
OAM_0 circular grating	−22.67	−58.13	−65.33
OAM_1 circular grating	−56.10	−11.07	−18.51
OAM_{-1} circular grating	−73.25	−18.53	−11.28

We can conclude that with the circular grating we can achieve better results of mode overlap than with the antenna array, but at the expense of a higher dependence on the OAM order and a slightly worse crosstalk. For the transmission within a fiber that supports more OAM modes, we could suppress the OAM_0 mode and use only the other 6 OAM modes (OAM_{-3}, OAM_{-2}, OAM_{-1}, OAM_1, OAM_2 and OAM_3), that we can generate with the circular grating.

In the next section, we explore the use of topology optimization for the design of OAM couplers.

3.4 OAM Couplers using Topology Optimization

Topology optimization is a design method used for the optimization of structures in different fields [52–54]. In this method, the materials in a discretized region are modified to satisfy some constraints and optimize a FOM [52,53]. Differing from shape optimization, where only a few boundary parameters between materials in a predefined structure are optimized, in topology optimization there is no need to specify a predefined structure and the optimized region is free to assume any shape that satisfy the constraints and optimize the figure of merit [54]. This can lead to more efficient structures with non-intuitive shapes.

Topology optimization plays an important role in structural mechanics, where, for more than 30 years, it has been used by mechanical and civil engineers for the minimization of material and strain energy in structures, while maintaining the mechanical strength [52–54]. More recently, it has been used in integrated photonics applications for the design of more compact and efficient devices [54, 55].

Topology optimization can be performed using different optimization algorithms. However, evolutionary algorithms, as the genetic and the PSO, would only be feasible for simple geometries, since they rely on a random test of a large number of parameters sets in order to find a satisfactory solution [56]. For complex problems, these algorithms became infeasible due to the large number of degrees of freedom, which would imply in a very large number of simulations to explore all the possible designs [55]. Furthermore, the electromagnetic simulation of photonics devices with complex geometries has a high computational cost. In order to perform topology optimization for complex geometries in a more efficient way and in a reasonable amount of time, gradient-based algorithms are applied [56].

With gradient-based algorithms, the gradient, which represents the sensitivity of the figure of merit with respect to the changes in the permittivity distribution, can be used to determine the best direction and guide the optimization process [55]. For topology optimization, we need the gradient for all points of the discretized region, i.e. the topological derivative.

This topological derivative can be computed with only two electromagnetic simulations using the adjoint method. The adjoint method consists in performing a forward simulation, i.e. a normal simulation of the structure with the fields propagating in the normal direction, as illustrated in Fig. 3.19(a), and an additional simulation, called adjoint simulation, where the simulation is inverted, placing the source at the monitor position and the fields propagate in the opposite direction, as we can see in Fig. 3.19(b).

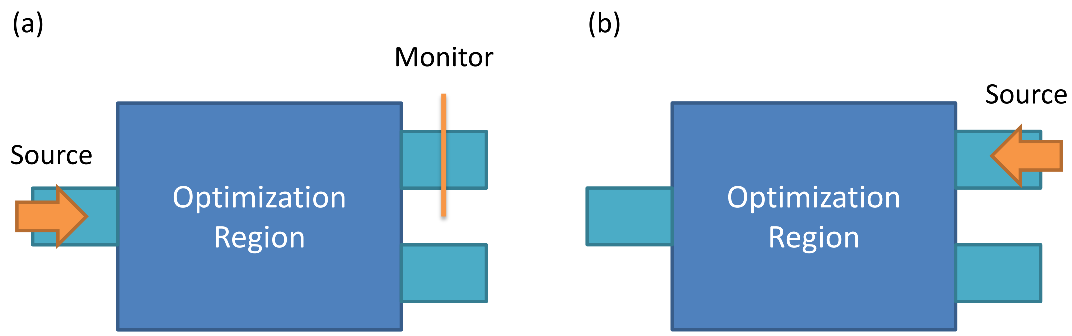

Figure 3.19: Topology optimization using the adjoint method. (a) Forward simulation and (b) adjoint simulation.

These two simulations can be performed parallelized during each iteration. From each simulation we take the field distribution in the optimization region. Combining the forward and adjoint fields results, we can obtain the derivative of the figure of merit with respect to the change in the dieletric permitivity for every point at the design region [56].

In this work, we performed topology optimizations using LumOpt [5], which is an open-source Python implementation of the adjoint method based on [56]. It communicates with Lumerical FDTD Solutions via the lumapi [6], a Python Application Programming Interface (API) for Lumerical, to perform the electromagnetic simulations. LumOpt offers a friendly user interface where is defined the optimization parameters, such as the materials dielectric permittivities, the number of points of the discretized optimization region, the initial conditions and the figure of merit. With LumOpt it is also possible to perform parametric shape optimization, when the goal is to optimize the shape boundaries or design parameters of a known device. For problems where the fields propagate in only one plane (for example, a taper or splitter) or when the structure is constant along one axis (for example, a linear grating coupler), we can start with a faster optimization in 2D. After the 2D optimization concludes, a 3D optimization can be performed to refine the optimized structure and obtain a more realistic result.

Using LumOpt, the topology optimization is divided in three phases. The first one is called the greyscale phase, when the discretized points can assume any value of dielectric permittivity between the minimum and maximum defined, which corresponds to the cladding and waveguide permittivities, respectively. In this phase, a circular top-hat filter with a user-defined radius, as illustrated in Fig. 3.20(a), is also employed to ensure manufacturability by continuously smoothing the design, removing sharp corners, small holes and small islands. After a defined number of iterations is reached, the optimization goes to the second phase called binarization. In the binarization, the permittivity distribution is mapped using a heaviside filter. As illustrated in Fig. 3.20(b), the curve of permittivity mapping is affected by a parameter β. For small values of β, we have a more continuous mapping, while for high values of β, the mapping becomes more restricted to the minimum and maximum permittivities, as in a step function. During the greyscale phase $\beta = 1$, producing a linear mapping. In the binarization, β is increased in small steps, while for each increase a set of optimization iterations is performed to correct the perturbation that might have degraded the FOM [8].

The third and last phase is called Design for Manufacturing (DFM). In the DFM, the design minimum feature size is constrained to allow manufacturing. Based on a user-defined minimum feature size parameter, which is related to the lithography process limitations, an indicator function is added as a penalty term in the FOM and the design is optimized to also satisfy this constraint. In the end, small features are eliminated and the optimized device is ready for manufacturing.

[5] https://github.com/chriskeraly/lumopt

[6] https://support.lumerical.com/hc/en-us/articles/360037824513-Python-API-overview

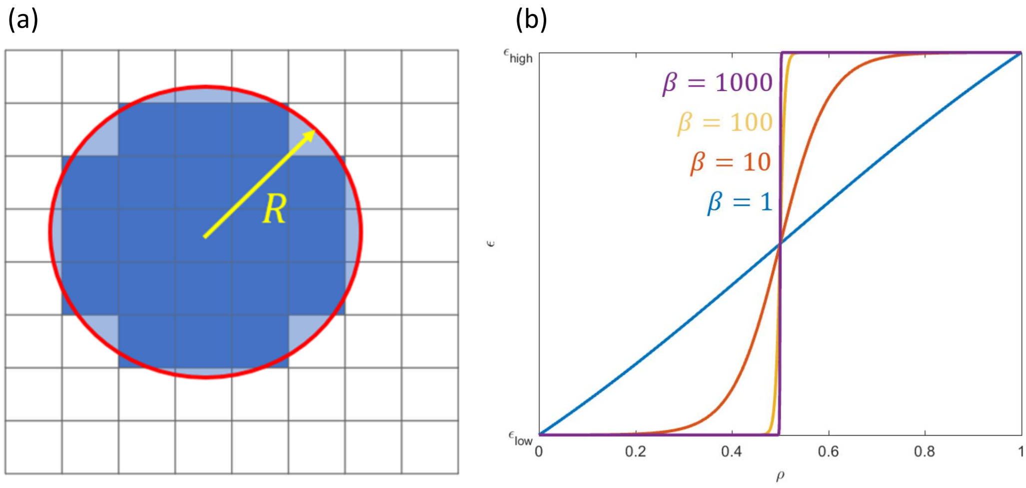

Figure 3.20: (a) Circular top-hat filter and (b) heaviside filter for different values of β. "Adapted from [8]"

In section 3.4.1, we present the optimization of a compact antenna using LumOpt, that can be used as an alternative antenna with only one etch level for the proposed OAM coupler of section 3.2. In section 3.4.2, we use LumOpt for the inverse design of integrated devices that directly couple the OAM fiber modes.

3.4.1 Single-Step-Etched Compact Antenna

In this section, we describe the design of a new compact antenna to be used in the antenna array of section 3.2. Our goal in this design is optimize the power transmission of the antenna at 1550 nm and reduce the fabrication complexity using a single etch step. With a single etch step we can fabricate the device in-house using the Unicamp facilities. The first step to design our compact antenna by topology optimization in LumOpt is to define the optimization parameters and simulation settings. We define an optimization region of 2 µm × 2 µm × 0.22 µm with a 0.45 µm-wide input/output waveguide, as we can see in Fig. 3.21.

We can use axial symmetry in relation to the x-axis to reduce the optimization region and, in consequence, the simulation time. We optimize only the top half of the region of Fig. 3.21(a) and mirror it at the end of the optimization to obtain the bottom half and the full structure. The optimization region is discretized with a step of 20 nm. The simulation region is 2.6 µm × 3 µm × 1.2 µm. A Gaussian source in a height of 0.4 µm above the center of the optimization region is used to feed the device with a Gaussian beam of 10.4 µm Mode Field Diameter (MFD). The output signal is measured through a 3D-FDTD simulation using a monitor in the waveguide, which is used to calculate the FOM. The FOM is defined as the mode overlap between the output mode and the fundamental TE mode of the waveguide in the wavelength range from 1450 nm to 1650 nm. The waveguide permittivity (ε_{max}) is 3.48^2 and the cladding permittivity (ε_{min}) is 1.44^2.

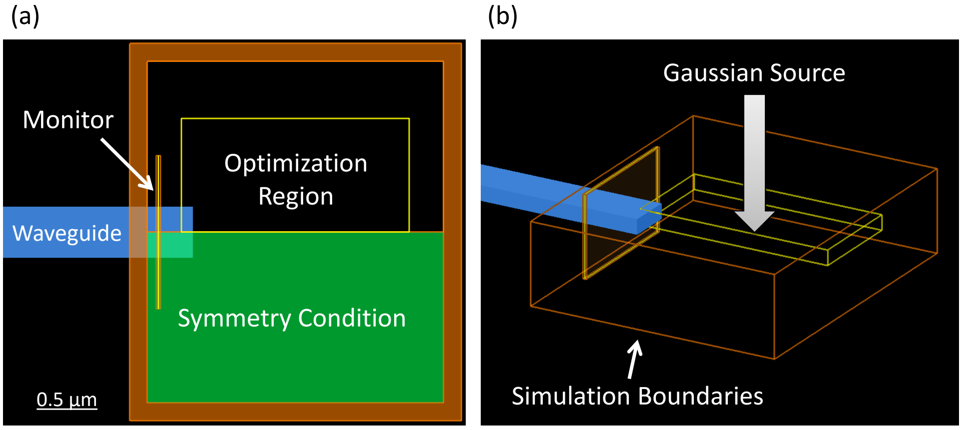

Figure 3.21: Simulation setup for the topology optimization of the single-step-etched compact antenna using LumOpt. (a) Top view. (b) Perspective view.

The start condition for the optimization region is all points with ε_{max}. A value of 150 nm is used for both circular filter and minimum feature size. The maximum number of iterations during the greyscale phase is defined as 60 and the maximum number of iterations per binarization step is 40. The FOM is handled in linear scale, than the target value is 1. The optimization will stop when changes in the error function, which is the difference between the target value and the FOM are less than 10^{-4}. The evolution of the error in function of the number of iterations is shown in Fig. 3.22. In the insets of Fig. 3.22 we can see the evolution of the optimized structure in different stages.

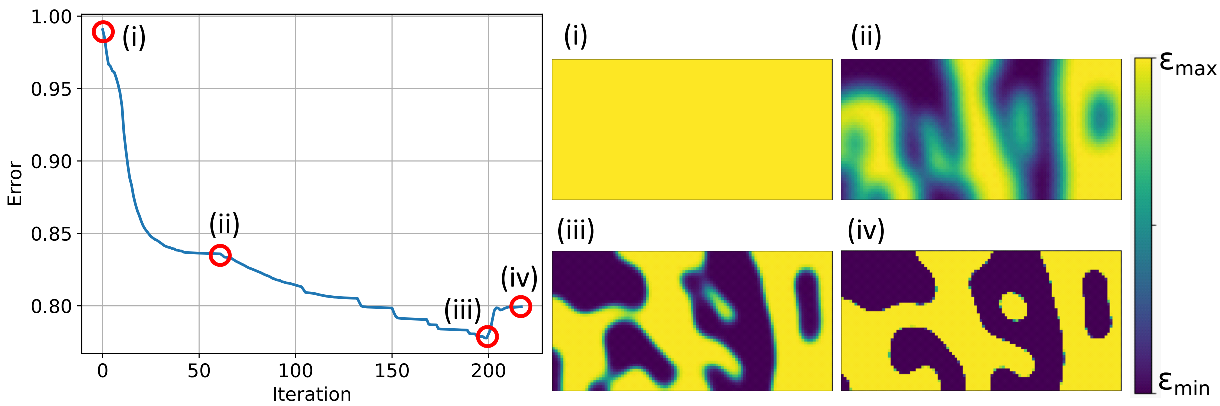

Figure 3.22: Single-step-etched compact antenna optimization. Evolution of the FOM in function of the iteration number. Insets show the optimized structure in different stages: (i) Iteration 0, (ii) Iteration 60, (iii) iteration 199 and (iv) iteration 218.

The inset (i) of Fig. 3.22 represents the start condition, where all structure is filled with ε_{max}. After 60 iterations and at the end of the greyscale phase, we have the optimized structure of Fig. 3.22(ii) with the permittivity assuming any value between ε_{max} and ε_{min} in the optimization region. The binarization phase goes from the iteration 61 until the iteration 199, where we obtain the binarized structure of Fig. 3.22(iii). When the DFM phase starts and the design is constrained to fulfill the minimum feature size, the FOM slightly decreases and a few more iterations are performed to optimize the constrained structure. The final optimized structure is obtained at the iteration 218, as we can see in Fig. 3.22(iv).

A refraction index monitor covering all the optimization region is used to extract the final parameters of the optimized structure and export it to GDSII format. The final structure of the single-step-etched compact antenna is shown in Fig. 3.23.

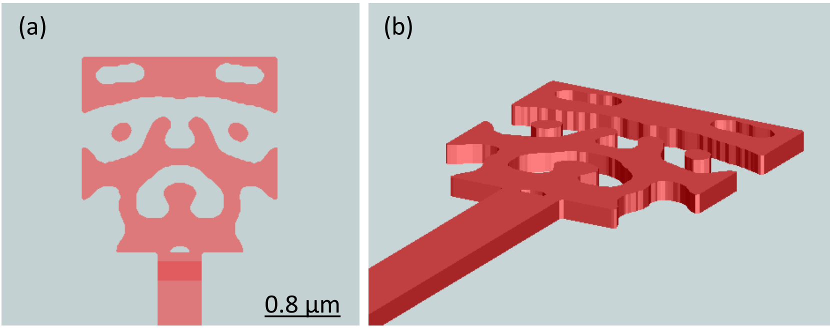

Figure 3.23: Single-step-etched compact antenna. (a) Top view. (b) Perspective view.

The transmission results feeding the antenna with a mode source in the input waveguide and measuring the output power with a monitor in a height 2 µm above the device is shown in Fig. 3.24(a). As we can see, this antenna is also broadband, covering the wavelength range from 1300 mn to 1700 nm with the transmission varying between −4.2 dB and −5 dB with peaks at the wavelengths of 1450 nm and 1625 nm. The electric field intensity profile at the same height is shown in Fig. 3.24(b). We design the OAM coupler based on an antenna array using this antenna and we perform the same analysis of section 3.2 for this new antenna array, which is shown in Fig. 3.25.

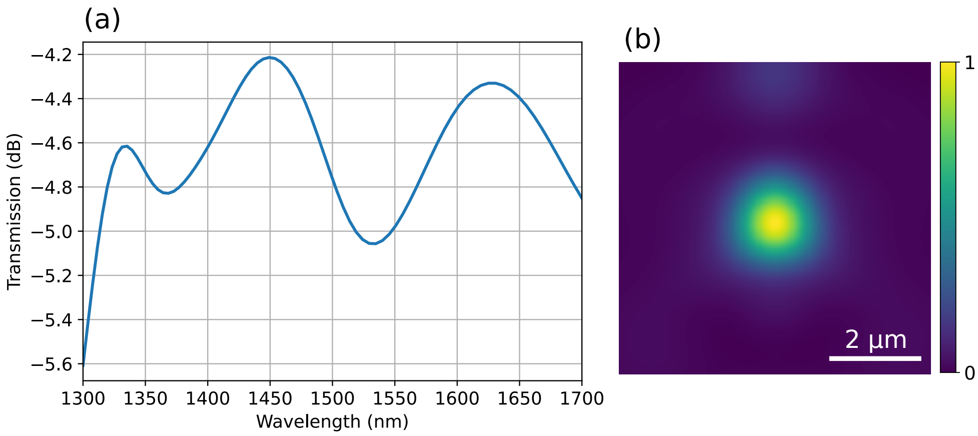

Figure 3.24: (a) Simulation results of the optimized single-step-etched compact antenna. (a) Transmission and (b) Electric field intensity.

The results of mode overlap in function of array radius can be seen in Fig. 3.26(a) at the wavelength of 1550 nm and in Fig. 3.26(b) at the wavelength of 1470 nm. As we can

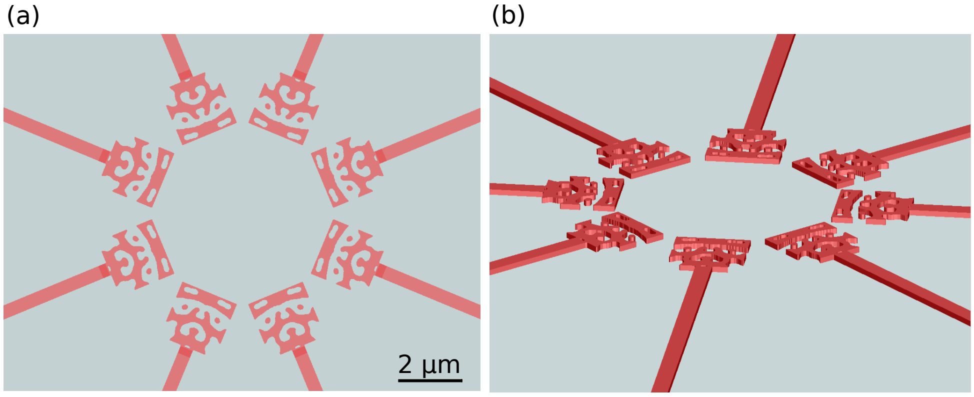

Figure 3.25: (a) Antenna array using the optimized single-step-etched compact antenna. (a) Top view. (b) Perspective view.

see, both wavelengths the radius of 5 µm provided the best results for the OAM_0 mode, while the radius of 6 µm provided the best results for the OAM_1 and OAM_{-1} modes. The values obtained for the radius of 5 µm are listed in Table 3.6 for 1550 nm and in Table 3.7 for 1470 nm. As we can see, the results for the OAM_1 and OAM_{-1} modes are very close to the ones obtained in section 3.2, a difference less than 1 dB. However, for the OAM_0 mode, we obtained slightly better results with this new antenna, an increase of 4 dB at 1550 nm and 2 dB at 1470 nm.

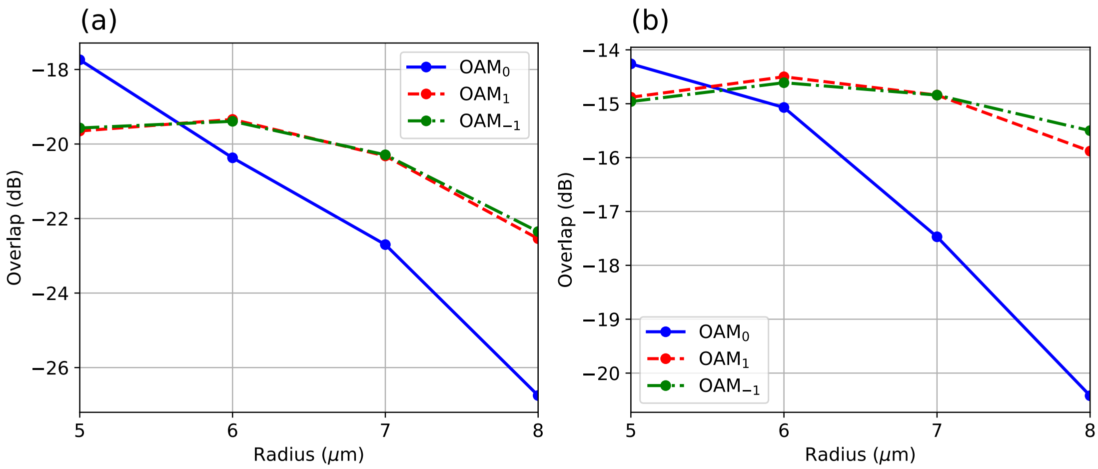

Figure 3.26: Mode overlap in function of array radius for the antenna array with the single-step-etched compact antenna simulated in (a) at 1550 nm and in (b) at 1470 nm.

The obtained crosstalk values are also very low for the OAM_0 mode with the OAM_1 or OAM_{-1} modes, almost −45 dB at 1550 nm and almost −50 dB at 1470 nm. The crosstalk values between the OAM_1 and OAM_{-1} modes are almost the same obtained with the antenna of section 3.2, almost −8 dB. The electric field results for the proposed array with the optimized single-step-etched compact antenna can be seen in Fig. 3.27 at 1550 nm and in Fig. 3.28 at 1470 nm.

As we can see in Fig. 3.27 and in Fig. 3.28, the field profiles of the array with

Table 3.6: Overlap between fiber modes and antenna array using the optimized single-step-etched compact antenna with a radius of 5 µm at 1550 nm.

	OAM_0 Fiber (dB)	OAM_1 Fiber (dB)	OAM_{-1} Fiber (dB)
OAM_0 antenna array	−17.74	−66.22	−62.32
OAM_1 antenna array	−64.58	−19.65	−27.37
OAM_{-1} antenna array	−81.78	−27.40	−19.57

Table 3.7: Overlap between fiber modes and antenna array using the optimized single-step-etched compact antenna with a radius of 5 µm at 1470 nm.

	OAM_0 Fiber (dB)	OAM_1 Fiber (dB)	OAM_{-1} Fiber (dB)
OAM_0 antenna array	−14.26	−66.45	−64.15
OAM_1 antenna array	−65.00	−14.88	−22.30
OAM_{-1} antenna array	−90.79	−22.41	−14.96

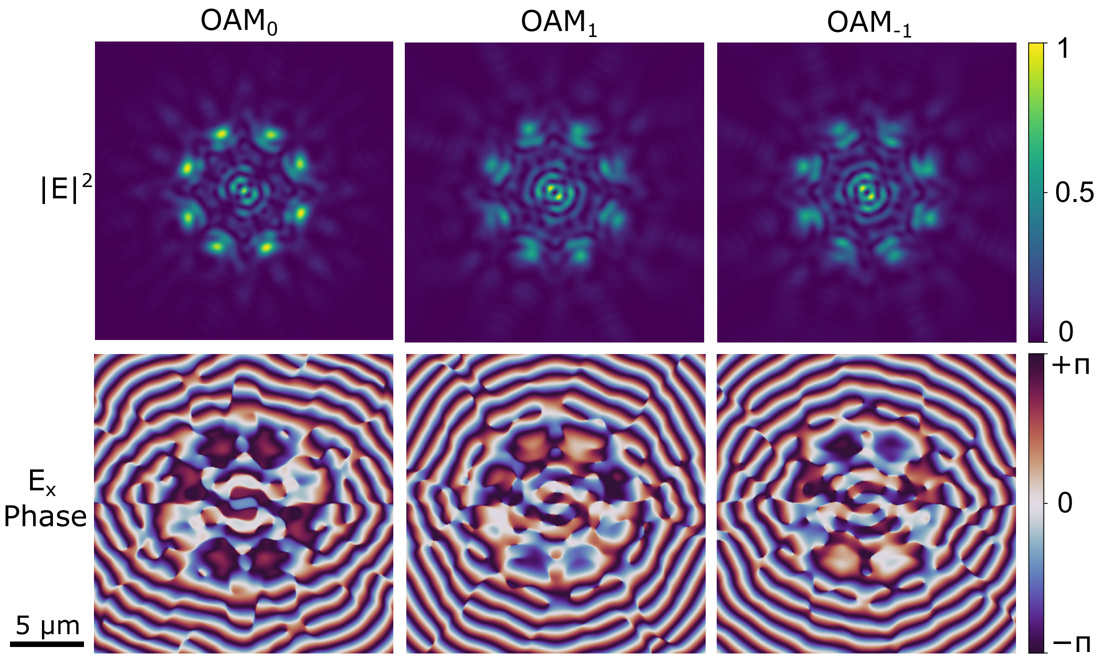

Figure 3.27: $|E|^2$ and E_x phase results of the antenna array using the optimized single-step-etched compact antenna with a radius of 5 µm simulated at 1550 nm

this new antenna is similar to the ones obtained using the antenna of section 3.2 (Fig. 3.7 and Fig. 3.12), but with a few differences. First, this antenna seems to have a higher directivity once the the fields of each antenna are more concentrated in each antenna region. This is more evident when comparing the phase profiles, where the phase surface of each antenna is wider in the case of section 3.2. Besides, the interference pattern in the region between the antennas and the center of the array due to the scattered field seems

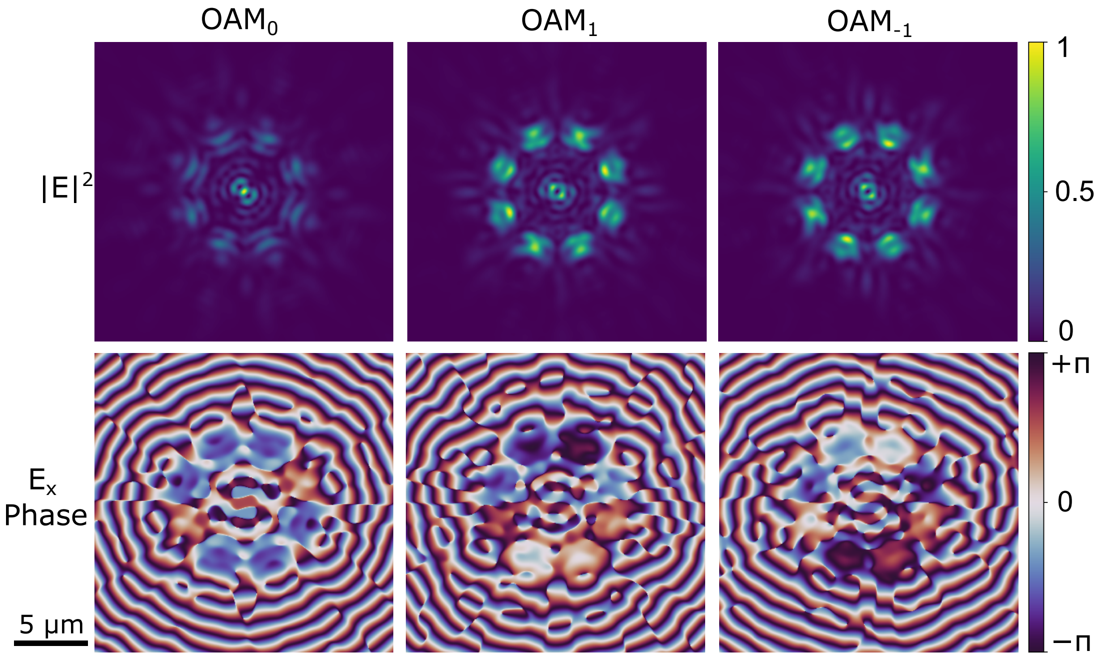

Figure 3.28: $|E|^2$ and E_x phase results of the antenna array using the optimized single-step-etched compact antenna with a radius of 5 µm simulated at 1470 nm

to be weaker with the new antenna and the constructive interference seems to be stronger in the center, especially for the OAM_0 mode. Another point is that the new antenna is slightly larger than the one of section 3.2, 0.22 µm larger. As the array radius was defined as the outer radius, i.e. the distance between the antenna input and the center of the array, this antenna is 0.22 µm closer to the array center and the antenna beam is approximately 0.11 µm closer to array center. That closer proximity to the array center could be another reason why we obtanined better results for the OAM_0 mode with this new antenna.

In summary, our optimized antenna proved to be a feasible alternative to the antenna of section 3.2, since its array has almost the same efficiency for the OAM_1 and OAM_{-1} modes and a higher efficiency for the OAM_0 mode. Besides, it only has one etch level, which reduces the complexity of the manufacturing process.

3.4.2 Inverse Design of OAM Couplers

For the inverse design of integrated devices that directly couple the OAM fiber modes, we define an optimization region of 10 µm × 10 µm × 0.22 µm with a 0.45 µm-wide input/output waveguide, as we can see in Fig. 3.29.

We use an imported source, where we specify a custom spatial field profile for the source injection plane. The custom field profile is defined by the electric and magnetic field of each OAM fiber mode, according to coupler to be designed. We start with the inverse design of a coupler for the OAM_{-1} fiber mode. As the optimization region is much larger in this case, we discretized it with a step of 50 nm to satisfy the computational

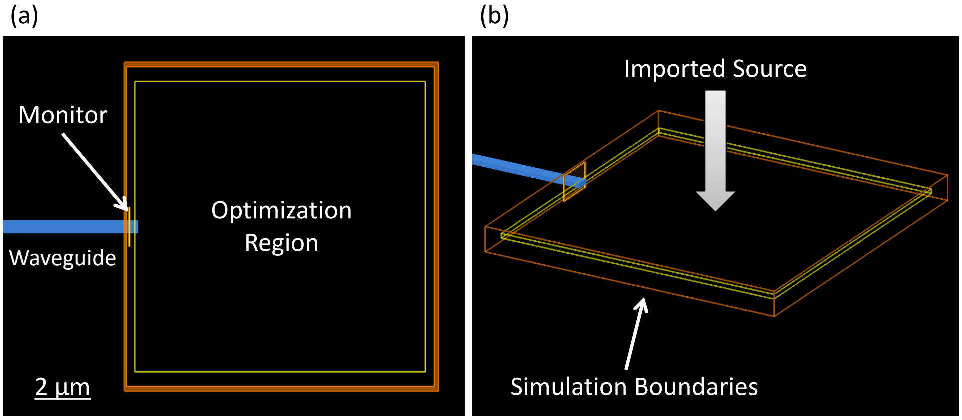

Figure 3.29: Simulation setup for the inverse design of OAM couplers using topology optimization in LumOpt. (a) Top view. (b) Perspective view.

requirements and to be able to perform the optimization in a reasonable amount of time. The simulation region is 10.6 µm × 11 µm × 1.2 µm. No symmetry conditions can be used in this case. The imported source is in a height of 0.4 µm above the center of the optimization region and the output signal is measured using a monitor in the waveguide, which is used to calculate the FOM. As in the single-step-etched compact antenna optimization, the FOM is also defined as the mode overlap between the output mode and the fundamental TE mode of the waveguide in the wavelength range from 1450 nm to 1650 nm. In this case, the start condition is the average value between ε_{max} and ε_{min} because using this condition the optimization converged faster. The remaining optimization parameters are the same used in section 3.4.1. At the end of the optimization, we can see the evolution of the error in function of the iteration number, as shown in Fig. 3.30. In the insets of Fig. 3.30, we see the evolution of the optimized structure in different stages.

As we can see in Fig. 3.30(i), at iteration 0 the structure is filled with a permittivity which is the average value between ε_{max} and ε_{min} as defined in the start conditions. After 60 iterations, the greyscale phase is concluded and we obtained the structure of Fig. 3.30(ii). The optimization proceeds to the binarization phase until the iteration 247, where we obtain the binarized structure of Fig. 3.30(iii). As we can see, during the binarization phase, the perturbation in the permittivity mapping caused several peaks of degradation of the FOM. The FOM is partially corrected in the iterations after each perturbation. The DFM phase causes another small degradation in the FOM and we obtain the final optimized structure at iteration 301, as we can see in Fig. 3.30(iv). Using a refractive index monitor and exporting the optimization region result to the GDSII format, we obtain the OAM coupler device for the OAM_{-1} mode, which is shown in Fig. 3.31.

We simulate this device using a mode source with the TE fundamental mode in the input waveguide and we measure the output field profile with monitors in different heights. The obtained results at 1550 nm can be seen in Fig. 3.32.

As we can see in the electric field intensity and phase profiles, as the emitted

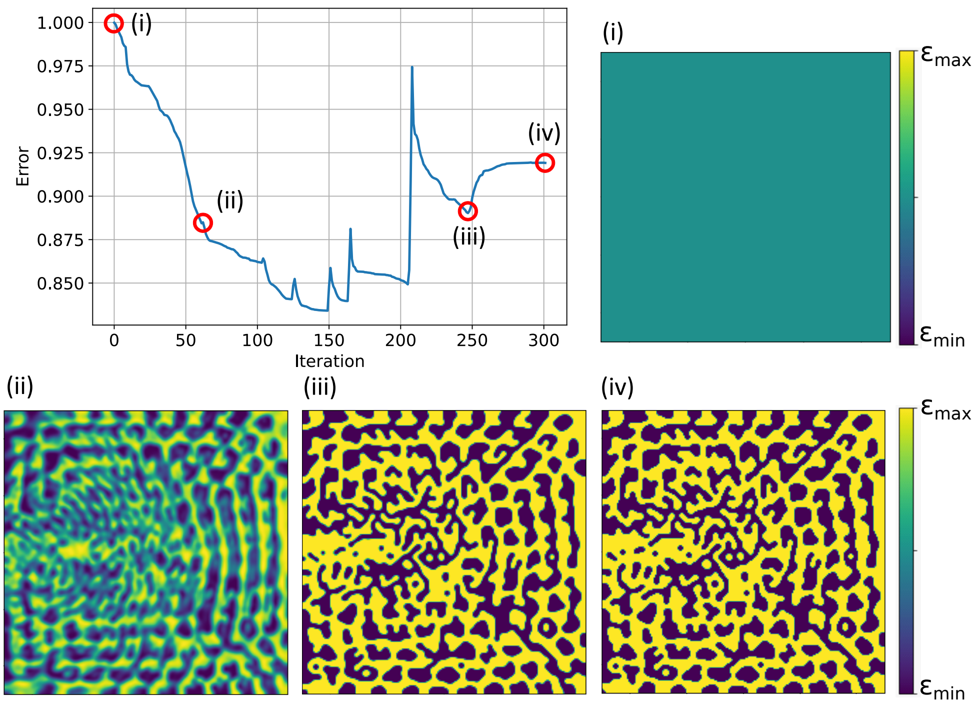

Figure 3.30: OAM coupler topology optimization for the OAM_{-1} mode. Evolution of the error in function of the iteration number. Insets show the optimized structure in different stages: (i) Iteration 0, (ii) Iteration 60, (iii) iteration 247 and (iv) iteration 301.

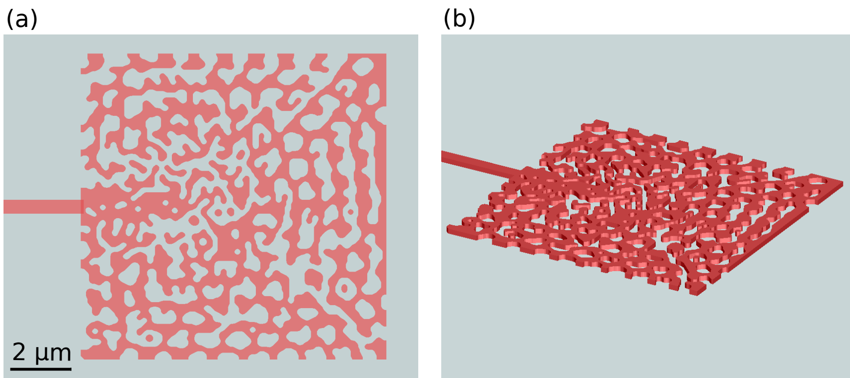

Figure 3.31: Inverse designed OAM coupler for the OAM_{-1} fiber mode. (a) Top view. (b) Perspective view.

OAM beam propagates, it becomes more and more similar to the OAM fiber mode. As a consequence, the mode overlap increases with the monitor height, as we can see in Table. 3.8. We start with a mode overlap of −8.45 dB at the height of 2 µm and it increases until the height of 50 µm, where we obtain a maximum mode overlap of −3.99 dB. This is an interesting behaviour of this OAM coupler. As it is composed by different diffracting elements in its structure, the emitted beam is very irregular and it starts to become more uniform after some propagation distance, which increases the overlap. On the other hand, the emitted beams by the OAM couplers based on antenna array and circular grating diverge faster and the mode overlap only decreases after a few micrometers of propagation.

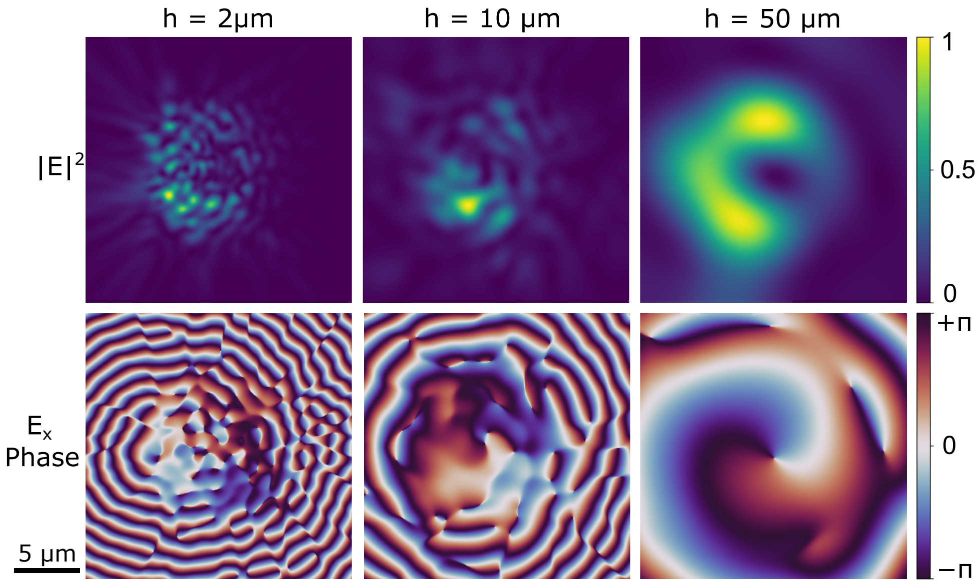

Figure 3.32: $|E|^2$ and E_x phase results of the inverse designed OAM coupler for the OAM$_{-1}$ mode at 1550 nm in different heights (h).

But even comparing at the same height of 2 µm, the inverse designed OAM$_{-1}$ coupler has a better result of mode overlap than the previous OAM$_{-1}$ couplers, approximately 11 dB better than the antenna array and 3 dB better than the circular grating at the wavelength of 1550 nm. Considering the maximum obtained overlap, at the height of 50 µm, the inverse designed OAM$_{-1}$ coupler is 15.5 dB and 7.5 dB better than the antenna array and the circular grating, respectively.

Table 3.8: Overlap, between the OAM$_{-1}$ fiber mode and the inverse designed OAM$_{-1}$ coupler, and transmitted power at 1550 nm in different heights (h).

	h = 2 µm (dB)	h = 10 µm (dB)	h = 50 µm (dB)
Mode overlap	−8.45	−6.40	−3.99

Vertically flipping the OAM$_{-1}$ coupler of Fig. 3.31(a), i.e. mirroring the coupler with respect to the x-axis, we can obtain the OAM$_1$ coupler, as shown in Fig. 3.33. Simulating this OAM$_1$ coupler, we obtain the same results of mode overlap and electric field intensity profile of the OAM$_{-1}$ coupler, but opposite clockwise orientation in the phase profile, as expected.

For the inverse design of the OAM$_0$ coupler, we perform a new topology optimization using the OAM$_0$ fiber mode as the imported source. The error evolution in function of the iteration number is shown in Fig. 3.34. The insets of Fig. 3.34 show the evolution of the optimized structure in different stages.

In the inset (i) of Fig. 3.34 we have the start condition of the optimized structure.

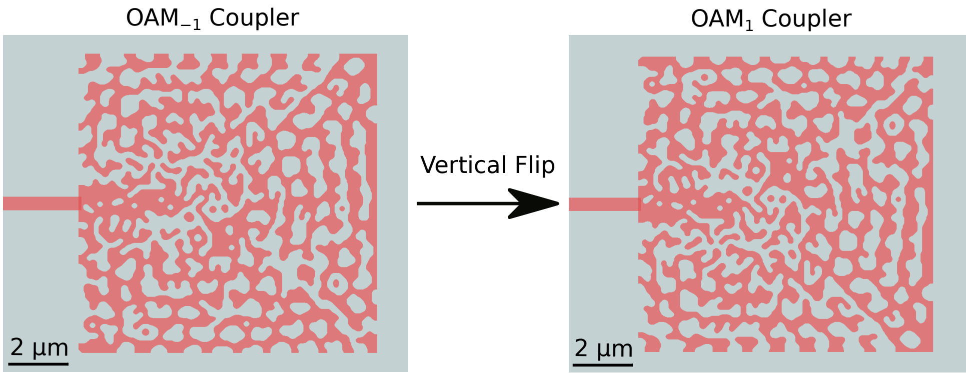

Figure 3.33: OAM_1 coupler obtained by the vertical flip of the OAM_{-1} coupler.

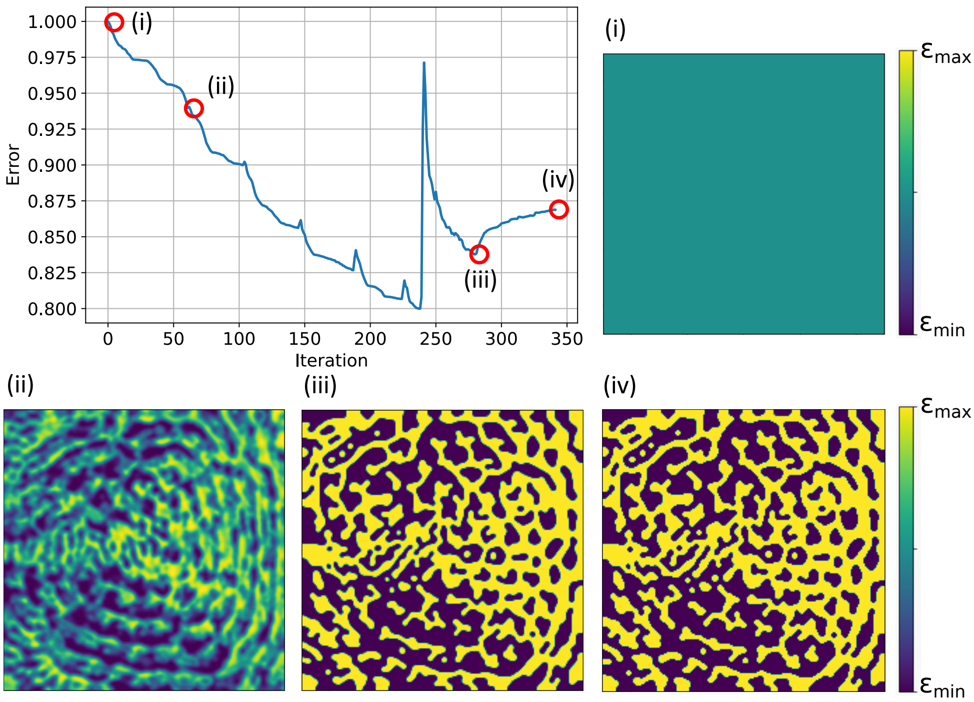

Figure 3.34: OAM coupler topology optimization for the OAM_0 mode. Evolution of the error in function of the iteration number. Insets show the optimized structure in different stages: (i) Iteration 0, (ii) Iteration 60, (iii) iteration 281 and (iv) iteration 341.

Fig. 3.34(ii) shows the result of the greyscale phase after 60 iterations. In Fig. 3.34(iii), we have the binarized structure after 281 iterations. The final structure, after the DFM phase, is obtained at iteration 341, as shown in Fig. 3.34(iv). We also simulate this OAM_0 coupler using a mode source with the fundamental TE mode in the input waveguide. The results of electric field intensity and phase profile at 1550 nm for different heights can be seen in Fig. 3.35. The results of mode overlap for each height is listed in Table. 3.9.

As we can see in Fig. 3.35, the emitted beam by the OAM_0 coupler also becomes more and more similar with the fiber mode as it propagates until the height of 50 µm. As a consequence, the mode overlap also increases with the height, as shown in Table 3.9. We obtained a mode overlap of −5.80 dB at the height of 2 µm, which is approximately

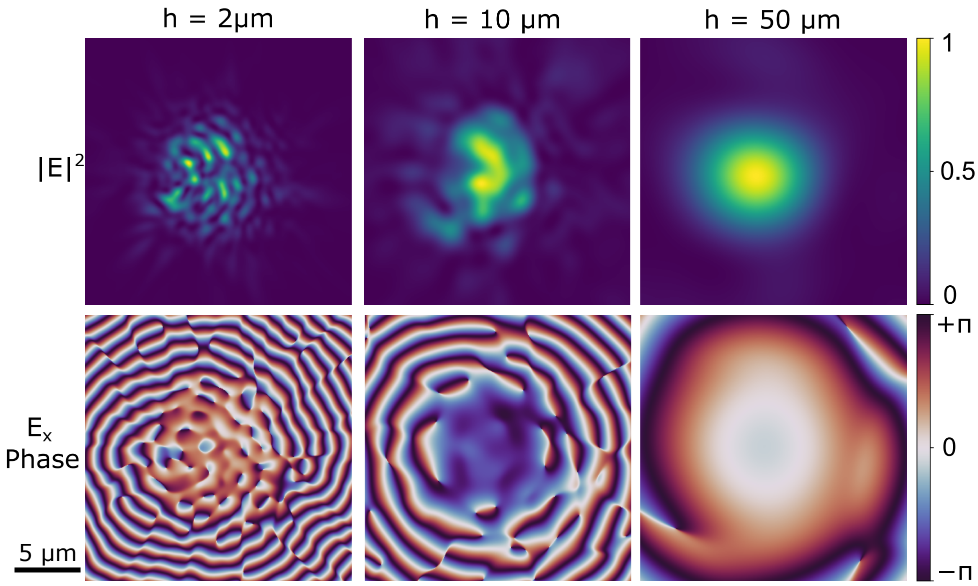

Figure 3.35: $|E|^2$ and E_x phase results of the inverse designed OAM coupler for the OAM_0 mode at 1550 nm in different heights (h).

Table 3.9: Overlap, between the OAM_0 fiber mode and the inverse designed OAM_0 coupler, and transmitted power at 1550 nm in different heights (h).

	h = 2 μm (dB)	h = 10 μm (dB)	h = 50 μm (dB)
Mode overlap	−5.80	−4.42	−2.24

12 dB better than the antenna array and 4.4 dB better than the circular grating at the wavelength of 1550 nm. At the height of 50 μm, we obtained the best value of mode overlap (−2.24 dB), which is 15.5 dB and 7.9 dB better than the antenna array and the circular grating, respectively. In Table 3.10, we summarize the obtained values of mode overlap and crosstalk for the inverse designed OAM couplers.

Table 3.10: Overlap between fiber modes and inverse designed OAM couplers at 1550 nm for a monitor height of 50 μm.

	OAM_0 Fiber (dB)	OAM_1 Fiber (dB)	OAM_{-1} Fiber (dB)
OAM_0 coupler	−2.24	−20.34	−23.65
OAM_1 coupler	−17.70	−3.99	−20.51
OAM_{-1} coupler	−24.62	−20.49	−3.99

The simulation results indicate that the topology optimization can potentially be used for the design of OAM couplers, showing better results of mode overlap than the previous approaches. However, the antenna array and the circular grating are tunable for different OAM modes, while the inverse designed couplers are fixed to a particular OAM mode.

In relation to the crosstalk, we obtained a value of $-13.7\,\mathrm{dB}$ in the worst case, as we can see in Table 3.10. This is a worse result than the obtained for the previous devices when considering the transmission of two OAM modes, but it is a better result when considering the transmission of three OAM modes. It could be improved in a topology optimization where the crosstalk is also considered as a parameter of optimization.

Chapter 4

Characterization of OAM Couplers

In this Chapter, we present the PIC layouts and experimental procedures for the characterization of our OAM couplers. The devices were manufactured in IMEC by a MPW run from the EUROPRACTICE IC SERVICE. By the time of the chip tapeout, we only have designed the OAM coupler using the antenna array approach of section 3.2, then, in this work, we only have experimental results for this proposed OAM coupler. In section 4.1, we present the proposed circuits for the OAM couplers' characterization. In section 4.2, we present the characterization results of coupling efficiency for the manufactured devices. Finally, in section 4.3, we analyse the OAM modes coupled from chip to fiber and from fiber to chip using different methods.

4.1 PIC Layout

For the characterization of the OAM couplers based on the antenna array, two types of circuits were developed. The first one is completely passive and the waveguides paths to the antennas are designed to change the phase of each antenna for the coupling of a specific OAM mode. The second type is an active circuit as it has metal heaters that can be used to change the phase of each antenna and tune different OAM modes.

The passive circuit layout is illustrated in Fig. 4.1. The circuit is composed by four parts. A SMF coupler, that consists in a focused grating coupler available in IMEC's Process Design Kit (PDK) and it is used for the coupling of the input optical signal from an external laser source to the chip. A cascade of power splitters divides the optical signal from one waveguide to eight waveguides. These power splitters are based on a Multimode Interferometer (MMI), which is also provided by the IMEC's PDK. A length control region is designed to adjust the phase of each antenna by changing its waveguide length. Finally, the eight waveguides connect to the OAM coupler that is composed by the antenna array.

For the length control region, an initial structure is designed in a way that all waveguides have the same length and the same number of bends. The 90° bends have a

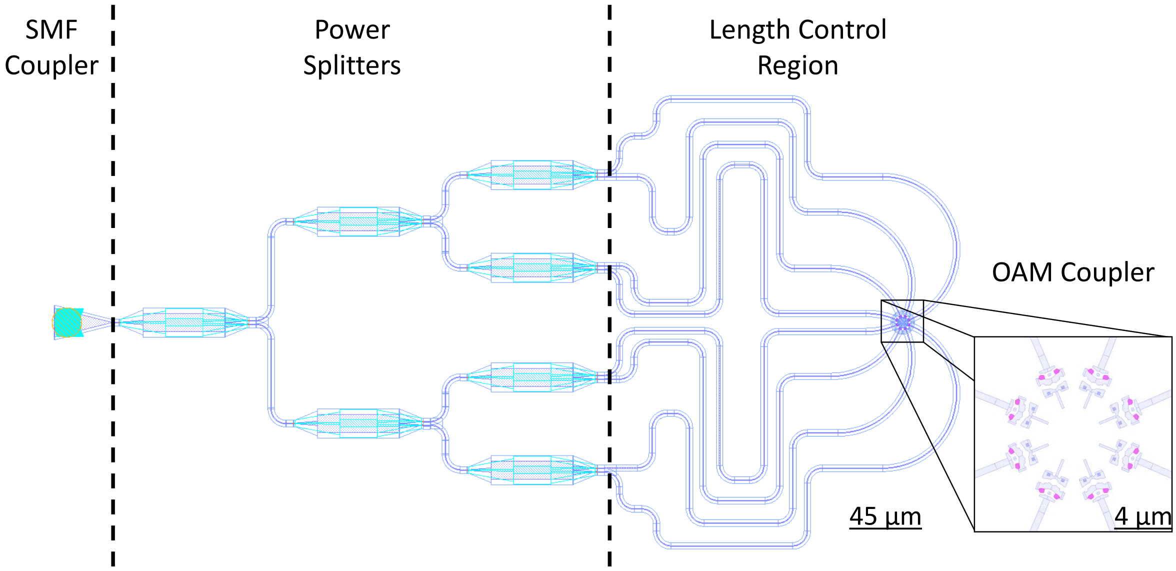

Figure 4.1: Passive circuit layout for the characterization of OAM couplers.

radius of 10 µm while the bends that connect the waveguides to the antennas have a radius of 50 µm. As the antennas' bends have different angles, they are designed with a much larger radius to not compromise the phase control and their length are calculated along with the straight waveguides. The final structure is designed increasing the length of each waveguide according to the OAM mode to be generated. To calculate the length difference of each waveguide, we start from the fact that two modes with the same propagation constant β propagated in two different lengths L_1 and L_0 have a difference of phase $\Delta\phi$ given by [50]:

$$\beta \cdot L_1 - \beta \cdot L_0 = \Delta\phi \tag{4.1}$$

The length difference, ΔL, is then given by:

$$\Delta L = \frac{\Delta\phi}{\beta} = \frac{\Delta\phi \cdot \lambda}{2\pi \cdot n_{\text{eff}}} \tag{4.2}$$

where λ is the operating wavelength of 1550 nm and n_{eff} is the effective index provided by IMEC's PDK for the standard waveguide at this wavelength.

Except for the OAM_0 mode, which does not have any phase shift and the waveguides have the same length, each OAM mode have a specific set of phase shifts and, consequently, length differences for the waveguides. For example, for the OAM_1 mode, the values of phase shift and length difference of each waveguide path are listed in Table 4.1.

The active circuit layout is illustrated in Fig. 4.2. Besides the SMF coupler, the power splitters, the length control region and the OAM coupler, the active circuit also has metal heaters for the phase control of each antenna and bond pads for the input electrical signals from an external source.

Table 4.1: Phase shift $\Delta\phi$ and length difference ΔL of each waveguide (WG) for the OAM_1 mode.

	WG_0	WG_1	WG_2	WG_3	WG_4	WG_5	WG_6	WG_7
$\Delta\phi$	0°	45°	90°	135°	180°	225°	270°	315°
ΔL	0 nm	82 nm	165 nm	247 nm	329 nm	412 nm	494 nm	576 nm

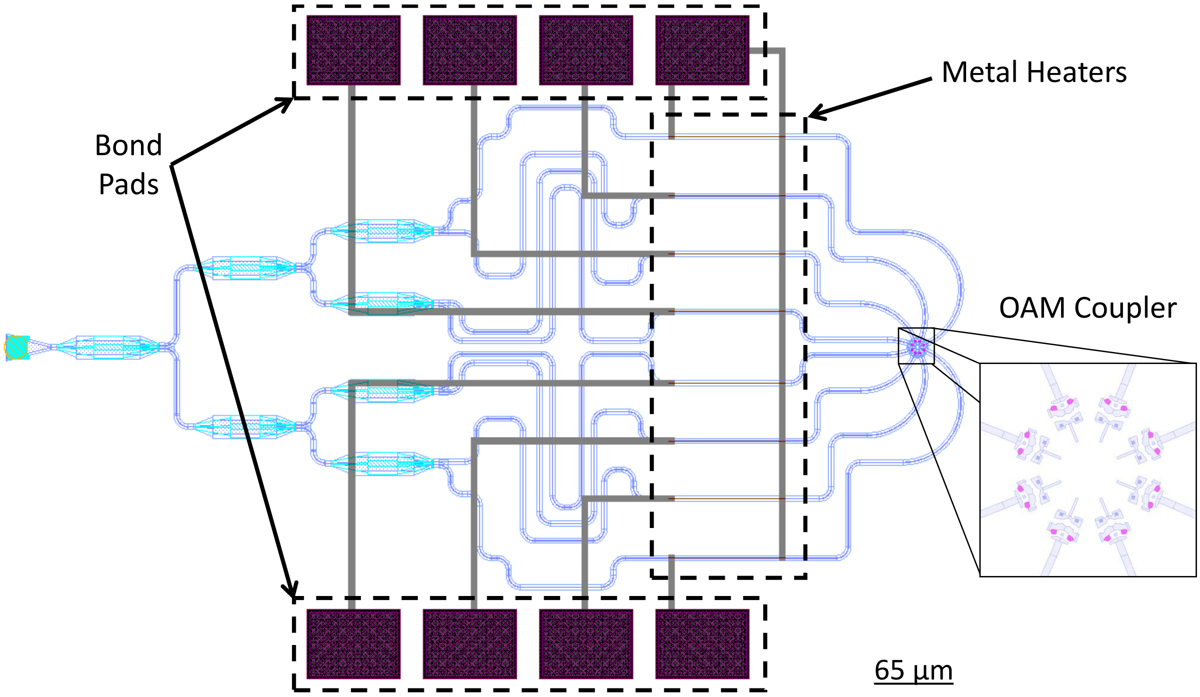

Figure 4.2: Active circuit layout for the characterization of OAM couplers.

The metal heaters are designed using a tungsten layer below the waveguides, they are 100 µm long and they are 50 µm apart from each other to avoid thermal crosstalk. One of the bond pads is the Ground (GND) reference, while the others can be used to inject electrical current and shift the phase of each waveguide.

For the passive circuit, we designed some variations, changing the length control region, to couple with different OAM modes. For both passive and active circuits, we also designed some variations of the OAM coupler changing the array radius (R). These variations are listed in Table 4.2. Although our Photonic Bandgap Fiber (PBGF) only supports the OAM_0, OAM_1 and OAM_{-1} modes, as described in section 3.1, we also included some circuits for the OAM_2 and OAM_3 modes for future tests.

We also included in the chip some circuits to characterize the waveguide and the SMF coupler. These circuits are illustrated in Fig. 4.3, where three waveguides of different lengths have SMF couplers for both input and output of the optical signal. They can be used to characterize the optical loss from the the waveguide and SMF coupler, as it is depicted in section 4.2.

Table 4.2: Variations of circuits for the OAM couplers' characterization.

Circuit	OAM	R
Passive	0	5 µm
Passive	0	8 µm
Passive	1	7 µm
Passive	1	8 µm
Passive	2	5 µm
Passive	3	7 µm
Passive	3	8 µm
Active		6 µm
Active		8 µm

Figure 4.3: Layout of circuits to characterize the waveguide and the SMF coupler.

The chip layout was designed in accordance with the layers description and design rules from IMEC's PDK. For the circuits design we used the python module gdspy [1], which writes the layout in the industry standard GDSII format. After the chip layout was ready, we sent it to IMEC for the manufacturing. In Fig. 4.4, we can see optical microscope images of the manufactured chip. Fig. 4.4(a) shows the passive circuit and Fig. 4.4(b) shows the OAM coupler based on antenna array with radius of 8 µm.

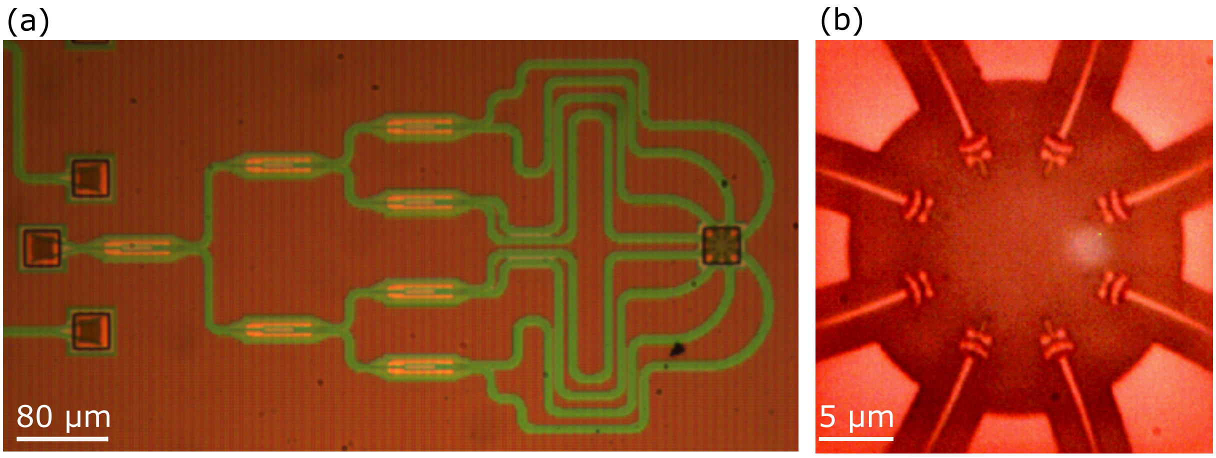

Figure 4.4: Optical microscope images of the manufactured chip. (a) Passive circuit. (b) OAM coupler based on antenna array with radius of 8 µm.

[1] https://gdspy.readthedocs.io/en/latest/

4.2 Coupling Efficiency Measurements

In this section, we first show the characterization results for the waveguide and SMF coupler (subsection 4.2.1). Then, in the subsection 4.2.2 we present the coupling efficiency results for all variations of OAM couplers and, using the results of waveguide propagation loss and SMF coupler efficiency, we analyse the coupling efficiency of each OAM coupler.

4.2.1 Waveguide and SMF Coupler

To characterize the waveguide propagation loss and the SMF coupler efficiency, we use the circuits of Fig. 4.3 and the experimental setup illustrated in Fig. 4.5.

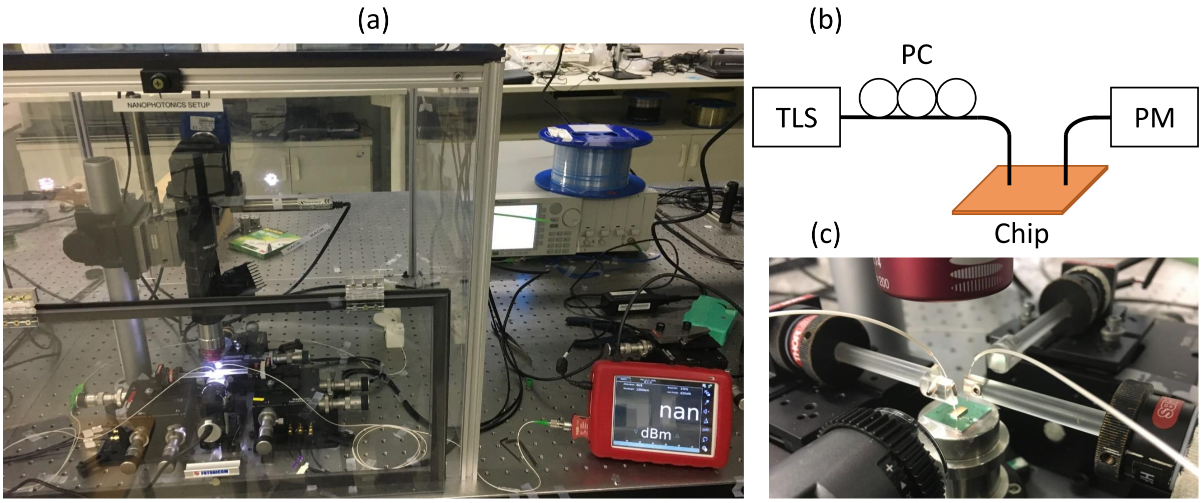

Figure 4.5: Experimental setup for the waveguide and SMF coupler characterization. (a) Image of the setup including all components and equipment. (b) Block diagram of the setup. (c) Image with zoom of the fiber-to-chip coupling.

As we can see in the block diagram of Fig. 4.5(b), a Tunable Laser Source (TLS) is used to generate a linear polarized optical signal whose polarization is rotated, using a Polarization Controller (PC), for the coupling of the TE mode in the chip through the SMF coupler. The optical signal propagates through the waveguides and exits the chip using another SMF coupler. The output optical signal is measured using a Power Meter (PM). Both input and output fibers are aligned with the couplers using 3-axis positioner stages, as we can see in Fig. 4.5(a) and Fig. 4.5(c). Two microscope cameras are also used for top and lateral view of the chip during the alignment.

The fiber angle is adjusted to minimize the optical loss at 1550 nm. This angle is approximately 10°. A wavelength sweep is performed in the TLS from 1450 nm to 1650 nm and the optical power is measured for each wavelength using the PM. This measurement is performed for the three circuits of Fig. 4.3. As the three circuits have different waveguide length, measuring the optical loss for the three waveguides length we can apply the cutback method and calculate the waveguide propagation loss as function of waveguide length. After obtaining the waveguide propagation loss, we can also calculate the coupling efficiency of the SMF coupler.

Considering a previous calibration to compensate the optical loss in the PC, the results of optical transmission at 1550 nm for the three waveguide lengths are illustrated in Fig. 4.6(a). Using the cutback method, we fit an approximate linear relation between the optical transmission and the waveguide length. The waveguide propagation loss is then given by the slope of the line and the transmission efficiency of both input and output SMF coupler together is given by the point where the line intercept the y-axis. To determine the coupling efficiency of each SMF coupler, we assume that both input and output couplers have almost the same efficiency and we divide the value equally for each one. The SMF coupler efficiency in function of wavelength is shown in Fig. 4.6(b). The final results obtained at 1550 nm were: 1.97 dB/cm of waveguide propagation loss and 4.55 dB of coupling efficiency for each SMF coupler. Both results are in agreement with the IMEC's PDK specifications.

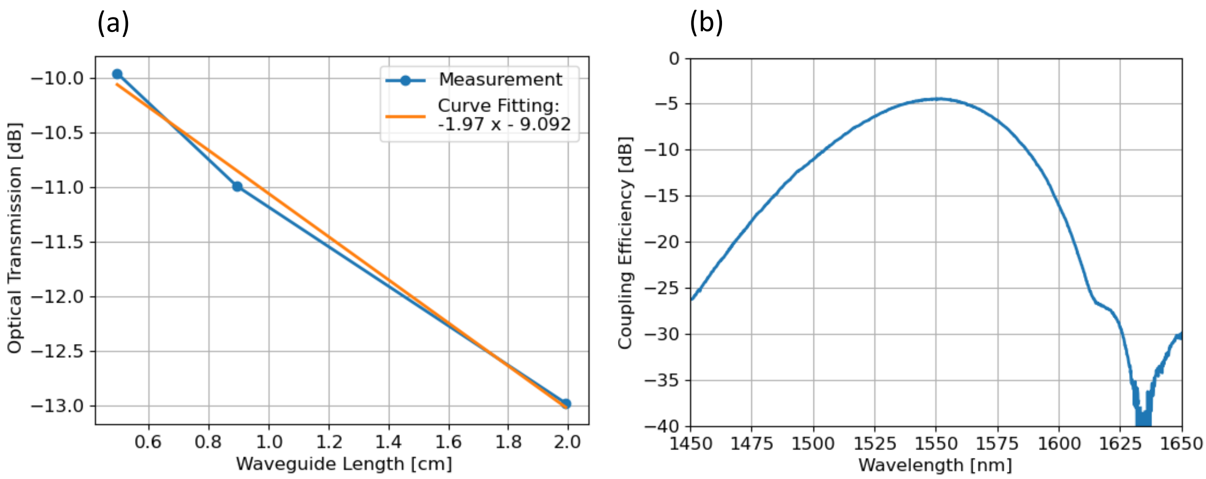

Figure 4.6: (a) Results of optical transmission versus waveguide length using the cutback method. (b) Coupling efficiency result for the SMF coupler.

4.2.2 Variations of OAM Couplers

The coupling efficiency measurements for all variations of OAM couplers are performed using the experimental setup of Fig. 4.5, but with a 230 m-long PBGF as the output fiber. Both input and output sides of the PBGF are cleaved. The input side is aligned with the OAM coupler and the output side is aligned with an Integrating Sphere (IS) connected to the PM for the measurement of the output power, as we can see in Fig. 4.7(a) and (b).

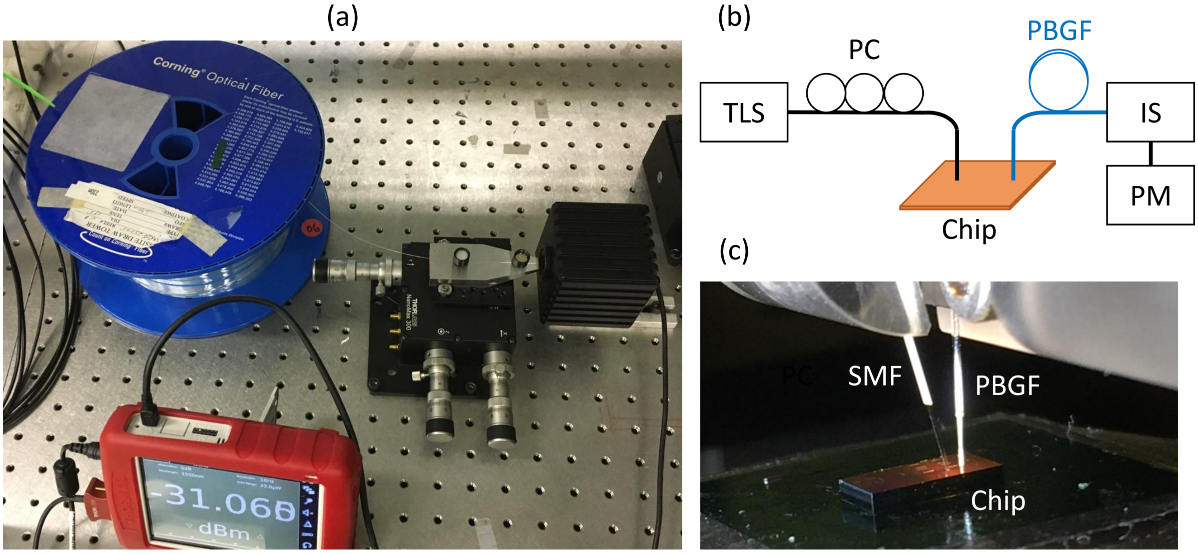

Figure 4.7: Experimental setup for the coupling efficiency measurements of OAM couplers. (a) PBGF as the output fiber aligned with an integrating sphere. (b) Block diagram of the setup. (c) Image with zoom of the SMF and PBGF coupling with the chip.

The PBGF angle is also adjusted to minimize the optical loss at 1550 nm, which in this case is 0°. Performing a wavelength sweep and measuring the output power in the PBGF for all variations of OAM couplers, we obtained the results of Fig. 4.8(a). To obtain the OAM coupler efficiency, we need to apply the calibration measurement, compensate the SMF coupler transmission spectrum and discount the losses from the waveguide propagation, from the cascade of power splitters and from the fiber propagation. The waveguide propagation loss is obtained from the results of subsection 4.2.1, which is approximately 0.14 dB. The loss from the cascade of power splitters is given by experimental results in the IMEC's PDK, which is approximately 9.12 dB for this case and the propagation loss in the PBGF is very high for this wavelength range, ∼20 dB/km according to [9], which corresponds to ∼4.6 dB in our 230 m-long PBGF. The results of coupling efficiency of each OAM coupler in function of wavelength can be seen in Fig. 4.8(b). In Table 4.3 we list the values of Coupling Efficiency (CE) at 1550 nm and 1470 nm for all OAM couplers.

As we can see in Fig. 4.8(b) and in Table 4.3, the OAM couplers with array radius of 5 µm have the best CE results. As we increase the radius, we obtain worse values of CE, which is in accordance with the simulation results presented in Chapter 3. We also obtained better results of CE at 1470 nm than at 1550 nm due to the higher transmission efficiency of the antennas at this wavelength. In fact, the spectral response of Fig. 4.8 is very similar to the one obtained for the antenna simulation (Fig. 3.11).

In the next section, we analyse the OAM modes coupled to the fibers to estimate the quantity of power that is coupled to the correct OAM mode.

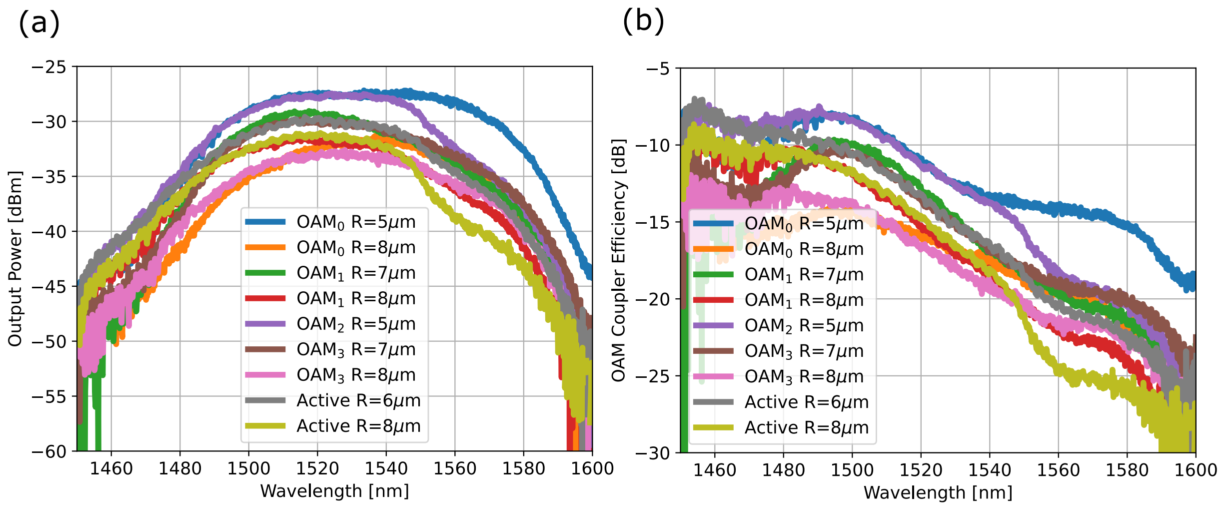

Figure 4.8: Coupling efficiency measurements for all variations of OAM couplers. (a) Results of output power versus wavelength. (b) Results of coupling efficiency versus wavelength.

Table 4.3: Coupling efficiency results for all variations of OAM couplers.

Circuit	OAM	R	CE at 1550 nm	CE at 1470 nm
Passive	0	5 µm	−13.95 dB	−10.99 dB
Passive	0	8 µm	−19.05 dB	−16.63 dB
Passive	1	7 µm	−18.45 dB	−13.93 dB
Passive	1	8 µm	−20.48 dB	−11.58 dB
Passive	2	5 µm	−15.64 dB	−8.63 dB
Passive	3	7 µm	−18.03 dB	−13.17 dB
Passive	3	8 µm	−20.42 dB	−14.45 dB
Active		6 µm	−18.59 dB	−8.94 dB
Active		8 µm	−21.16 dB	−10.4 dB

4.3 OAM Fiber Modes Characterization

For the analysis of the OAM modes coupled from the chip to the PBGF, we characterize the fiber modes using two different methods. In subsection 4.3.1, we use the Spatial and Spectral (S^2) imaging method to image and identify the fiber modes using an infrared camera. In the subsection 4.3.2, we use the OAM couplers as detectors, where the OAM modes are generated in free space using a SLM and focused into the PBGF.

4.3.1 Spatial and Spectral (S^2) Imaging Method

The S^2 imaging method [57] is an interferometry method used for the characterization of modal content in optical fibers. It can direct recover the relative power, amplitude and phase information of optical modes that propagates in the characterized fiber without previous knowledge of the modal content. It also does not need an additional interferometry path because it uses the dominant mode, usually the fundamental mode, as the reference [9, 21, 57].

The principle of operation of the S^2 imaging method is illustrated in Fig. 4.9. It relies on the fact that different fiber modes propagates with different group velocities. Performing a frequency sweep in the optical signal injected into the fiber and recording the output power with an infrared camera (Fig. 4.9(a)), we obtain the fiber modes interference pattern in function of wavelength for each pixel, as illustrated in Fig. 4.9(b). Calculating the Inverse Fourier Transform (IFT), we obtain the amplitude in function of differential delay (Fig. 4.9(c)), where each peak represents a beating tone for the interference between the fundamental mode and one HOM. The amplitude and relative phase of the HOM is then recovered as shown in Fig. 4.9(d).

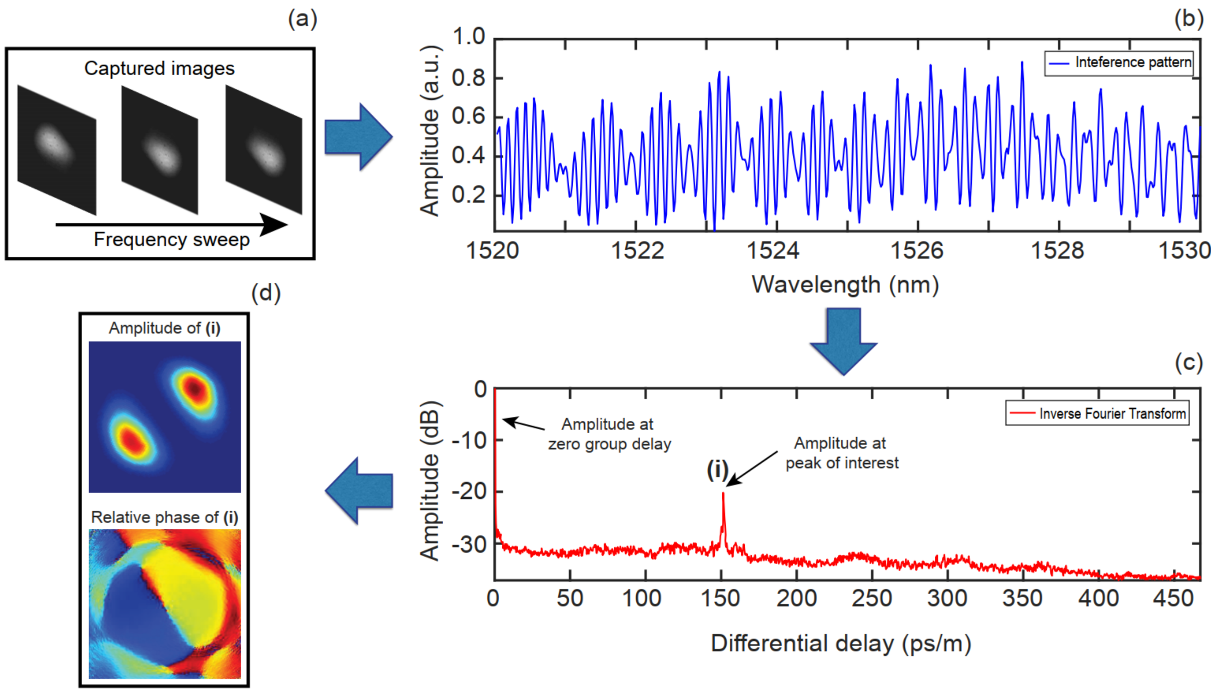

Figure 4.9: Principle of operation of the S^2 imaging method. (a) Capture of the beam profile at the fiber output during a frequency sweep. (b) Sepectrum of the interference pattern at an arbitrary pixel. (c) IFT of interference pattern with beating tones in function of differential delay. (d) Modal content of HOM that produced the beating tone (i). “Reproduced from [9]”

To perform the fiber modes characterization, we modify the experimental setup of Fig. 4.7 using a piece 80 cm-long of the PBGF and placing an additional positioner stage for a 20X Objective Lens (OL) with 20 mm of working distance. The OL transforms the fiber output light into a free-space collimated beam. The collimated beam pass through a Variable Attenuator (VA) and the beam profile is captured using an InGaAs camera, as we can see in Figure 4.10.

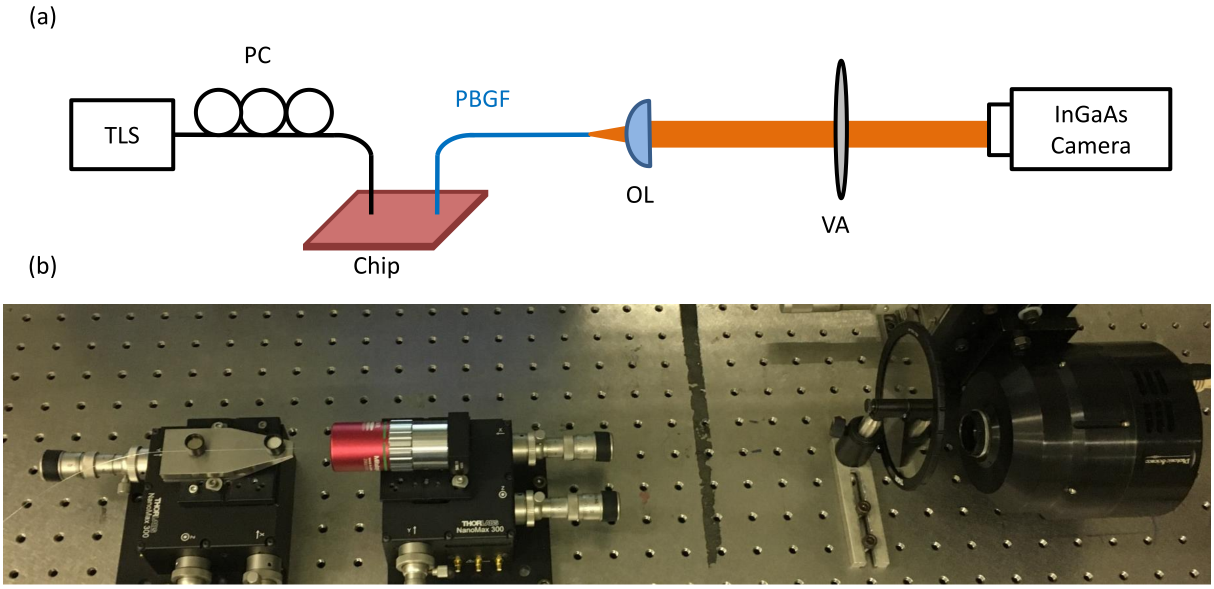

Figure 4.10: Experimental setup for OAM fiber modes characterization using the S^2 imaging method. (a) Block diagram of the setup. (b) Image of the setup showing the optical path from the output fiber to the InGaAs camera.

We perform the S^2 measurements in a wavelength range from 1510 nm to 1560 nm with a step of 10 pm. The results obtained for the OAM_0 coupler with a radius of 5 µm is illustrated in Fig. 4.11.

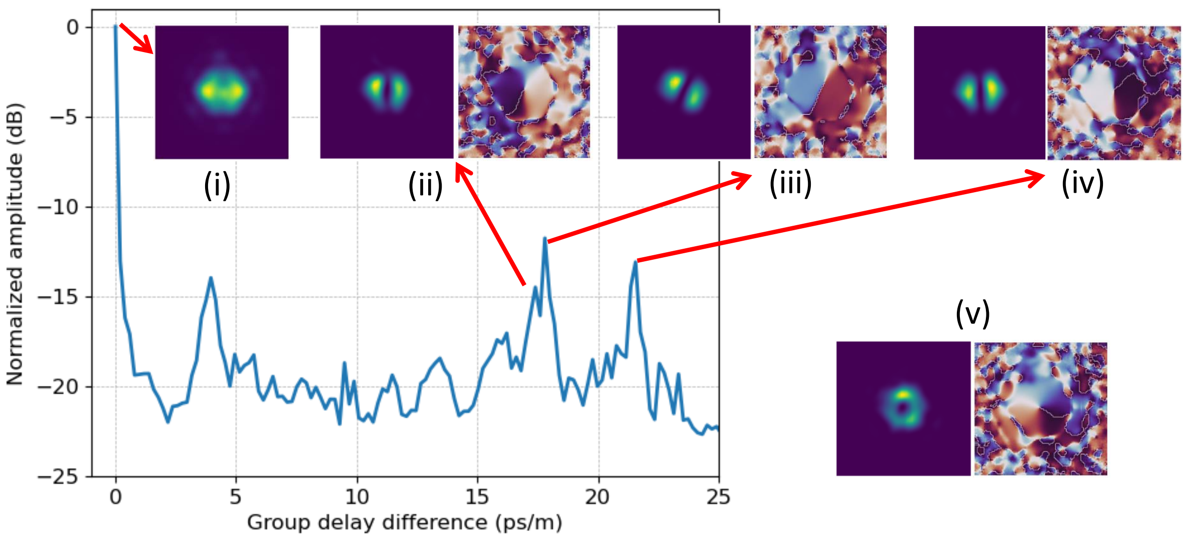

Figure 4.11: IFT result of S^2 measurement for the OAM_0 coupler with R=5 µm. Insets show the recovered modes from the beating peaks. (i) OAM_0/fundamental mode. (ii-iv) LP_{11}-like modes. (v) OAM_1 mode obtained by the combination of (iii) and (iv) modes.

From the IFT result we see that the OAM_0, i.e. the fundamental mode, is the dominant mode and the mode reference (Fig. 4.11(i)). The other peaks represent the beating tones between the fundamental mode and the HOMs or between HOMs. In the insets (ii-iv) of Fig. 4.11, we see the recovering modes from the beating tones with the fundamental mode. These modes are the LP_{11}-like modes for one polarization state. As described in section 3.1, the OAM_1 mode is obtained by the linear combination of two degenerated LP_{11}-like modes, the HE_{21}^{even} and HE_{21}^{odd} modes. Combining the (iii) and (iv) modes of Fig. 4.11, we obtained the OAM_1 mode as illustrated in Fig. 4.11(v).

We obtained the same results for the other passive OAM couplers, with the OAM_0 mode being the dominant mode in all cases. To investigate that and to test the active OAM couplers, we proceeded to the OAM fiber modes characterization using the method of subsection 4.3.2.

4.3.2 OAM Modes Detection

The second method implemented to analyse the coupling of OAM fiber modes consists in using the OAM couplers for the detection of pure OAM modes generated with a SLM. These pure OAM modes are coupled from free space to the PBGF using an OL and then coupled to the chip using our OAM couplers. The OAM coupler operates as an OAM receiver and the output power is measured in the SMF coupler.

The scheme of the experimental setup used for this method is illustrated in Fig. 4.12. The TLS generates the optical signal. A PC is used to rotate the polarization to a linear state. A 20X OL transform the light from the SMF into a collimated Gaussian beam. The Gaussian beam is transformed in a pure OAM beam when it is reflected by the SLM, where the OAM order is defined by the SLM phase mask. The OAM beam has its direction changed by a mirror (M). A moving mirror (MM) is also used to let the beam pass through, going to the InGasAs camera direction, or to reflect it, going to the PBGF direction. A variable attenuator is used before the camera and a $\lambda/4$ waveplate is used to convert the beam polarization from linear to circular before it is coupled into the fiber. Then, a 10X OL is used to focus the collimated OAM beam into the fiber. The other side of the PBGF is aligned with the OAM coupler and the output power is measured from the SMF coupler using a power meter. A picture of the experimental setup showing all the elements in the optical path from the TLS to the PBGF is illustrated in Figure 4.13.

In Fig. 4.14 we can see the field profile of different OAM beams captured by the camera. The OAM_0 beam corresponds to a Gaussian beam. The other OAM beams have a ring-shaped beam whose radius increases with the OAM order.

As the PBGF only supports the OAM_0, OAM_1 and OAM_{-1} modes, we use these modes as the inputs for the OAM couplers. We first measure the optical power after the PBGF for each OAM mode to calibrate the measurement. Then, we align the fibers with the respective couplers and we measure the output power in the SMF coupler. Applying the calibration measurement and discounting the losses from the SMF coupler,

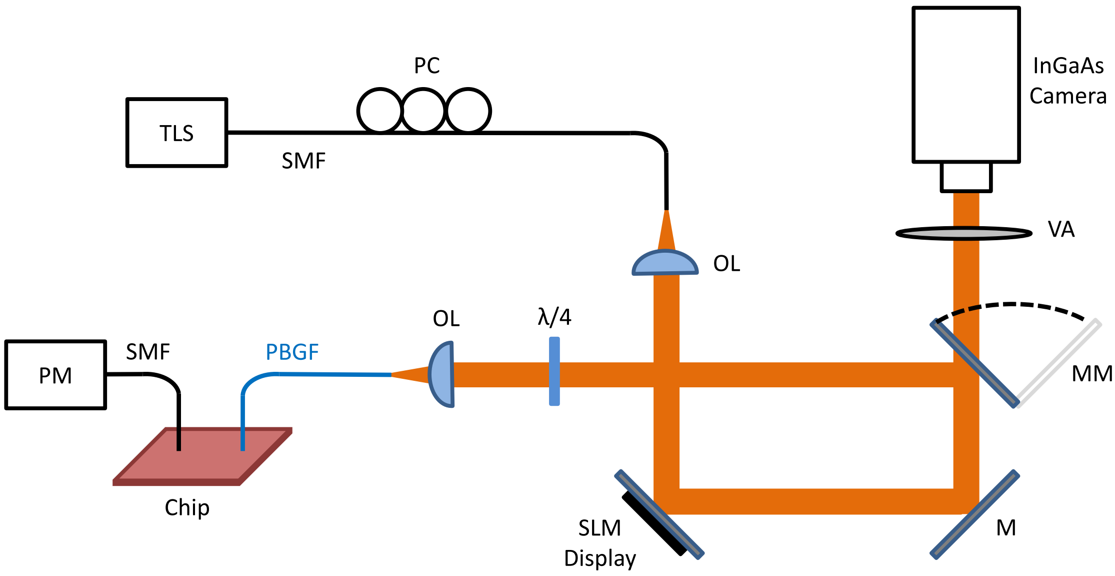

Figure 4.12: Scheme of the experimental setup for the OAM modes detection. TLS: Tunable Laser Source; PC: Polarization Controller; OL: Objective Lens; M: Mirror; MM: Moving Mirror; VA: Variable Attenuator; PM: Power Meter.

waveguide propagation and power splitters, we obtain the transmission results for each input OAM mode. The results obtained at 1550 nm for the passive OAM couplers can be seen in Fig. 4.15.

As we can see, the OAM_0 R=5 µm and OAM_1 R=8 µm couplers obtained better transmission results for the correct input OAM modes, but with intermodal crosstalks of −2.65 dB and −9.18 dB. The OAM_1 R=7 µm and OAM_0 R=8 µm couplers, on the other hand, obtained better transmission results for the incorrect input OAM modes. We also notice that the OAM couplers with radius of 5 µm and 7 µm obtained better results for the OAM_0 input mode, while the OAM couplers with a radius of 8 µm obtained better results for the OAM_1 mode. This can be attributed to an incorrect set of phase shifts in the antennas' waveguides due to fabrication variations. With an incorrect set of phase shifts, the radius could be more significant to define the best coupled OAM mode than the phases, since the OAM_1 and OAM_{-1} modes have a larger radius than the OAM_0 mode. This would also explain the worse values of crosstalk obtained for some OAM couplers. To verify this hypothesis, we performed an analysis of the relative phase shift in each antenna waveguide due to fabrication variations.

First, we calculate the effective index of the waveguide, simulating it in Lumerical Mode Solutions, for different widths according to the variation range after fabrication as specified by the foundry. The obtained result is shown in Fig. 4.16(a). Using the effective index results we can calculate the relative phase shift of each antenna waveguide. Calculating for the OAM_1 case, where the absolute phase shift and length difference of

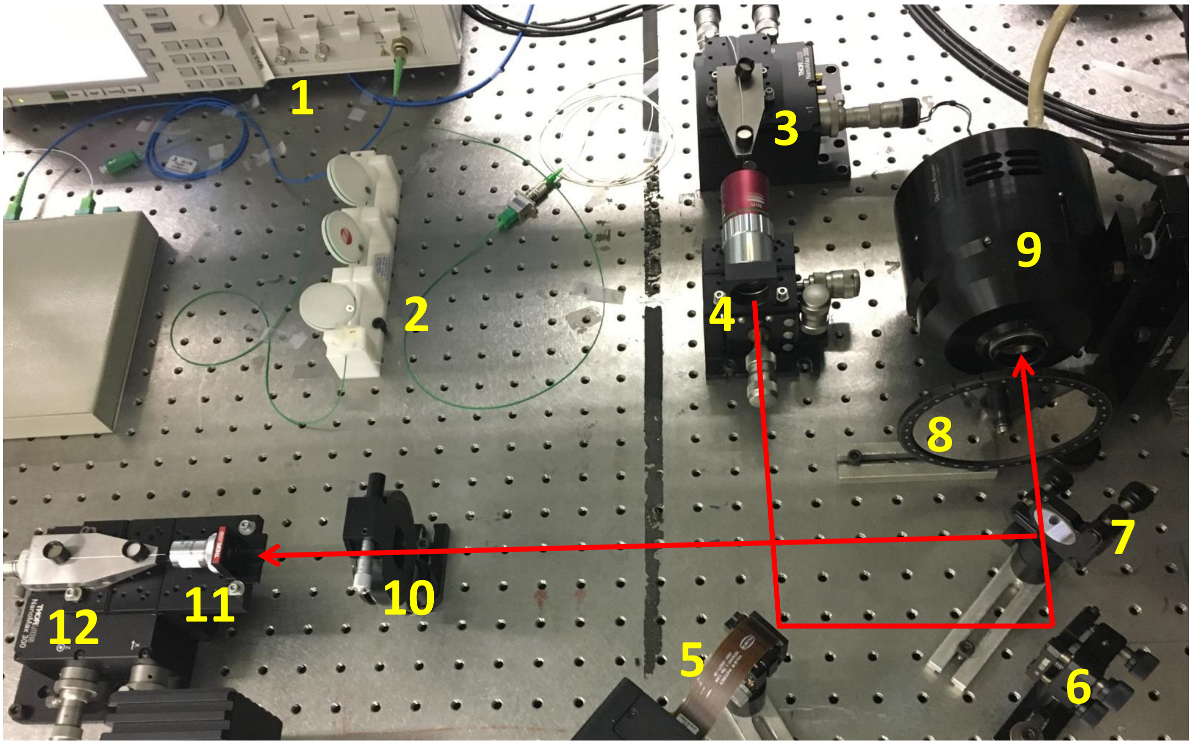

Figure 4.13: Picture of the experimental setup for the OAM modes detection. (1) Tunable laser source; (2) Polarization controller; (3) Single mode fiber (SMF); (4) 20X objective lens; (5) Spatial light modulator (SLM); (6) Mirror; (7) Moving Mirror; (8) Variable attenuator; (9) InGasAs camera; (10) $\lambda/4$ waveplate; (11) 10X objective lens; (12) Photonic bandgap fiber (PBGF).

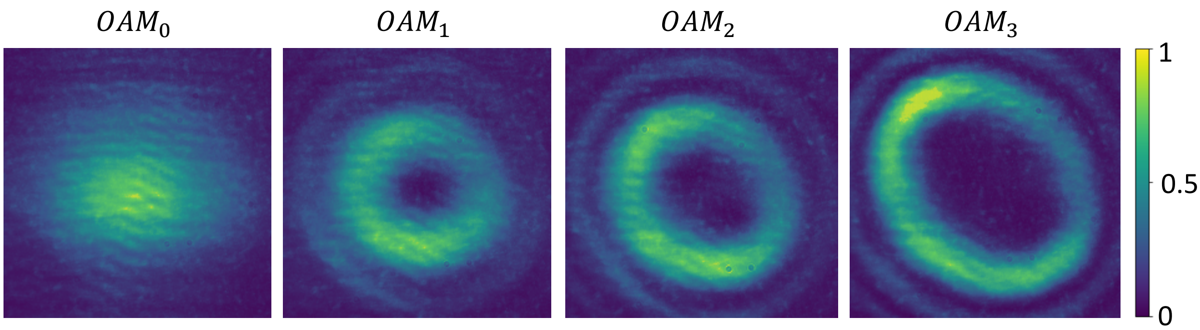

Figure 4.14: OAM beams generated with the SLM.

each waveguide is listed in Table 4.1, we obtained the results of Fig. 4.16(b). As we can see, the greater is the length difference (ΔL) of the waveguide, the greater is the relative phase shift. This is in accordance with Eq. 4.2, which can be rewritten as:

$$\Delta\phi = \beta \cdot \Delta L = \frac{2\pi \cdot n_{\text{eff}}}{\lambda} \cdot \Delta L \tag{4.3}$$

We see that we can have significant relative phase shifts due to fabrication

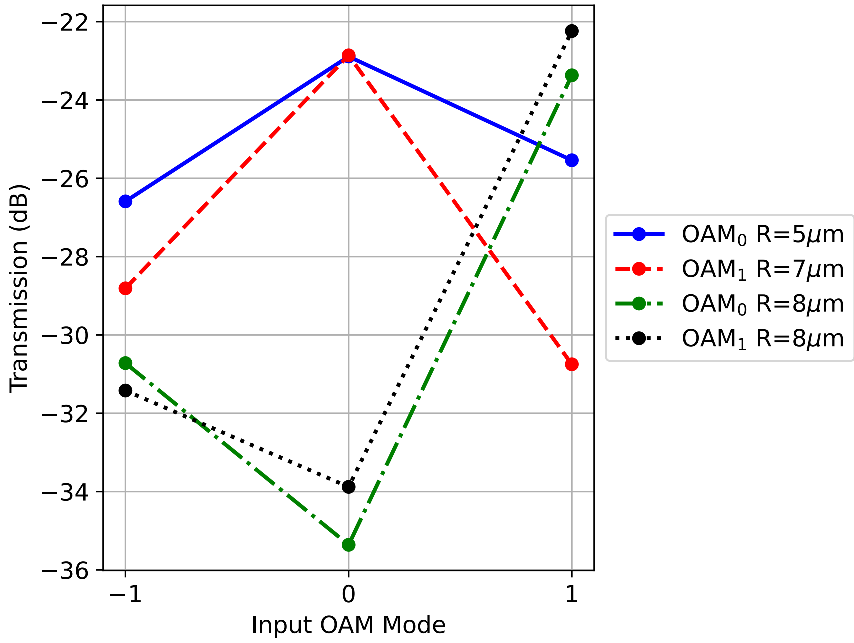

Figure 4.15: OAM modes detection results for the passive OAM couplers. Transmission at 1550 nm in function of the input OAM mode.

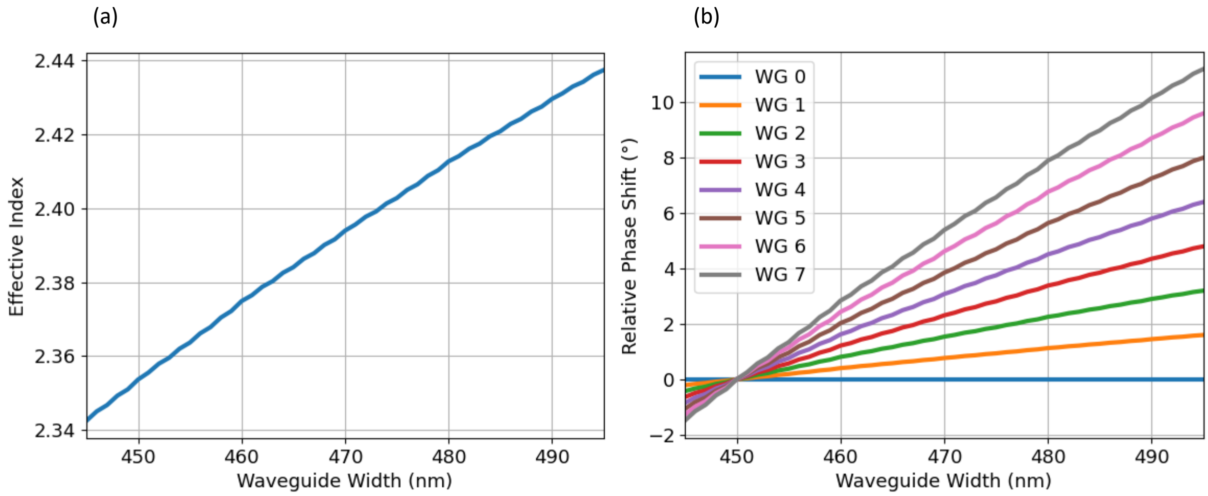

Figure 4.16: Analysis of the relative phase shift of each waveguide (WG) due to fabrication variations. (a) Waveguide effective index in function of width variation. (b) Relative phase shift in function of width variation.

variations, which can be greater than 10° for one of the waveguides. This would imply in a phase mismatch between the OAM fiber modes and the OAM couplers, which can degrade the mode overlap, degrade the intermodal crosstalk and even couple the incorrect OAM fiber mode, as it happened in some of the passive OAM couplers. Taking this possibility into account, we also designed the active OAM couplers, which have metal heaters to fine tune the phase shift of each antenna waveguide during the device operation.

To perform the measurements using the active OAM couplers, we packaged the chip into a standard butterfly package, as illustrated in Fig. 4.17(a). The chip was attached over a glass spacer to be positioned at the same height of the package electrical channels. A wire bonding is performed, using golden wires with 25 µm of diameter, to connect the electrical channels with the bond pads on the chip, as we can see in Fig. 4.17(b). Two lateral facets of the package are also removed for lateral viewing during the fibers alignment. In Fig. 4.17(c) we can see the fibers alignment for one of the active OAM couplers in the packaged chip.

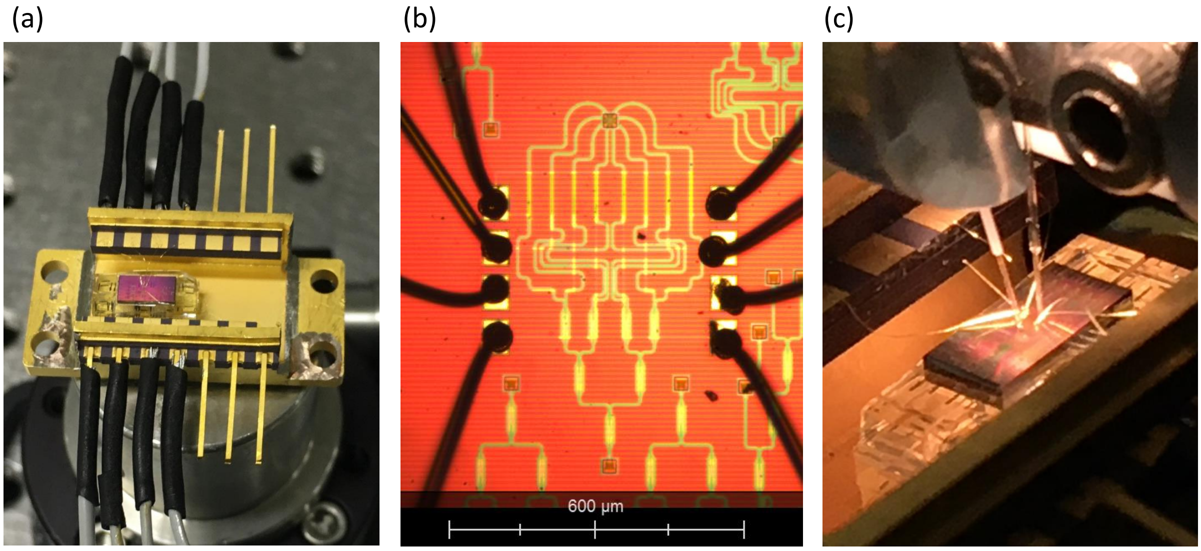

Figure 4.17: (a) Chip packaged into a standard butterfly package. (b) Image with zoom of the fabricated photonic circuit for the active OAM coupler after the wire bonding. (c) Image with zoom of the fibers alignment with the packaged chip.

We control the electrical power in each metal heater using DC sources. For a given input OAM mode, we adjust the electrical current of each metal heater, tuning the OAM coupler to maximize the optical power in the output. Then, for the optimized conditions, we measure the crosstalk with other input OAM modes. The results obtained at 1550 nm for the active OAM couplers in function of the OAM_0 and OAM_1 modes as the input modes can be seen in Fig. 4.18.

As we can see, we effectively coupled the correct OAM modes tuning the active OAM couplers. The OAM coupler with R=6 µm achieved the best transmission results for both OAM modes (−20.84 dB), but with crosstalk values of −7.97 dB and −14.88 dB when tuning the OAM_0 and OAM_1 modes, respectively. The OAM coupler with R=8 µm, on the other hand, achieved lower transmission results, −24.4 dB for the OAM_0 mode and −24.6 dB for the OAM_1 mode, but with both crosstalk values lower than −10 dB: −12.29 dB and −14.88 dB when tuning the OAM_0 and OAM_1 modes, respectively. In agreement with the simulation results, the OAM coupler with shorter radius obtained better transmission results. We also notice that for both couplers, when tuning the OAM_1

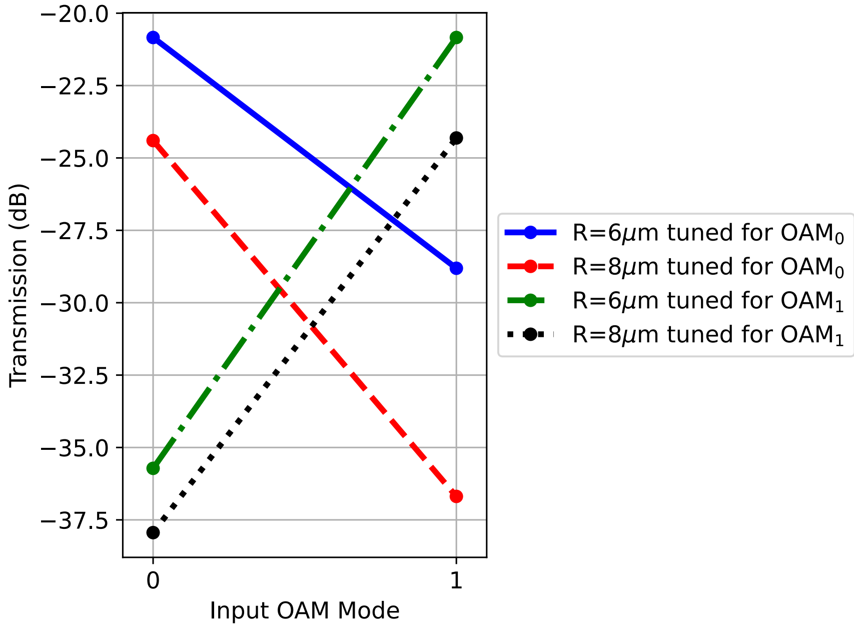

Figure 4.18: OAM modes detection results for the active OAM couplers tuned for different OAM modes. Transmission at 1550 nm in function of the input OAM mode.

mode, the crosstalk is lower than when tuning the OAM_0 mode. This makes sense once the couplers have the antennas in a ring distribution, making easier the coupling with a ring-shaped beam. The crosstalk results are also limited by the modes crosstalk inside the fiber, which is around −15 dB according to [9] and to the S^2 measurements results presented in subsection 4.3.1.

At 1470 nm the couplers have a better efficiency, but the output power has more noise from other optical components, especially from the SMF coupler, as we can see in the results of Fig. 4.8. Then we measure the active OAM coupler with R=8 µm at 1500 nm for the OAM_0, OAM_1 and OAM_{-1} modes as the input modes. The results obtained can be seen in Fig. 4.19.

As we can see, once again we effectively coupled the correct OAM modes, this time for the three OAM modes supported by the fiber. At this wavelength, we obtained a better transmission result for the OAM_0 mode (−18.41 dB) and a slightly worse value of crosstalk (−7.14 dB). For the OAM_1 mode we obtained almost the same result of transmission (−24.09 dB) and a worse value of crosstalk (−8.06 dB). For the OAM_{-1}, we obtained a transmission of −19.69 dB and a crosstalk of −7.23 dB. As discussed in Chapter 3, the transmission efficiencies would be better at shorter wavelengths at the expense of a higher crosstalk. The crosstalk also increases when using the three OAM modes supported by the fiber.

We also analysed the spectrum and bandwidth of the OAM couplers. For example, we analysed the active OAM coupler with R=8 µm tuned around 1550 nm for the OAM_1 mode (Fig. 4.20(a)) and the active OAM coupler with R=8 µm tuned around 1500 nm for the OAM_0 mode (Fig. 4.20(b)).

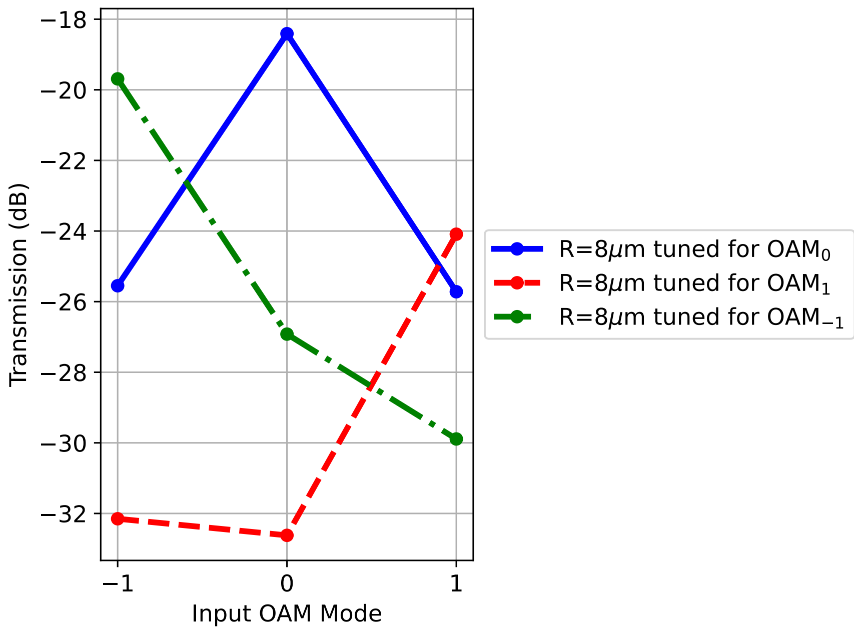

Figure 4.19: OAM modes detection results for the active OAM coupler with R=8 µm tuned for different OAM modes. Transmission at 1500 nm in function of the input OAM mode.

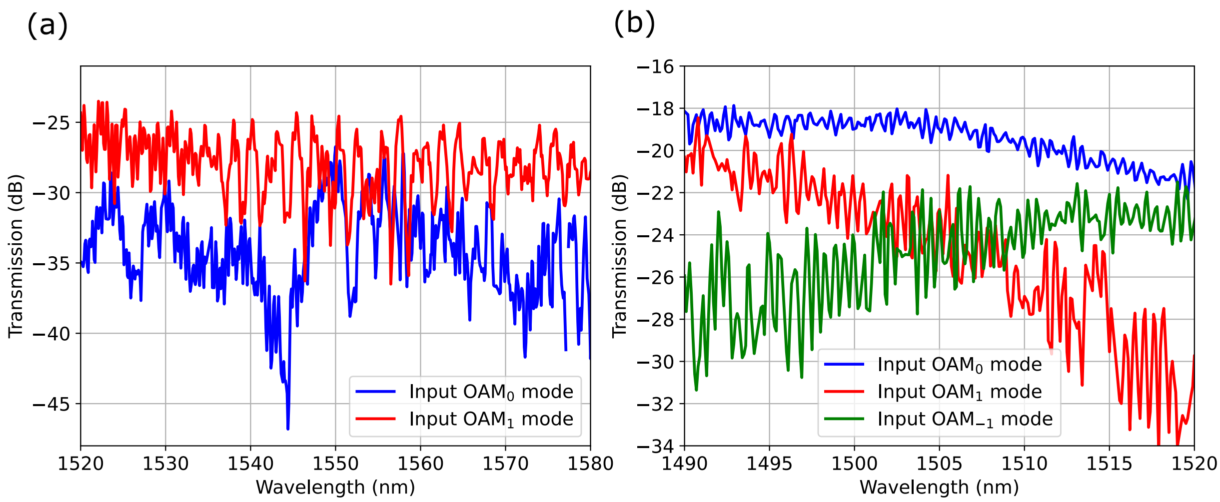

Figure 4.20: Spectrum results of the OAM couplers for OAM modes detection. (a) Active OAM coupler with R=8 µm tuned around 1550 nm for the OAM$_1$ mode. (b) Active OAM coupler with R=8 µm tuned around 1500 nm for the OAM$_0$ mode.

As we can see, all spectrum results have an interference pattern due to some reflection, which amplitude is greater for the incorrect OAM modes in the input. As the measured spectrum after the PBGF during the calibration measurements does not have this interference pattern, it can be attributed to reflections inside the chip. Calculating the Fast Fourier Transform (FFT) of the spectrum result of Fig. 4.20(a) for the input OAM$_1$ mode, we see that the main interference corresponds to a Free Spectral Range (FSR) of $\Delta\lambda = 0.4\,\text{nm}$. The length of the cavity that generates a Fabry-Pérot interferometer with this FSR is given by:

$$L_c = \frac{\lambda^2}{n_g \cdot \Delta\lambda} \tag{4.4}$$

where $n_g = 4.34$ is the waveguide group index, L_c is the distance travelled by the light in one roundtrip around the closed cavity and $L_c/2$ is the physical length of the cavity. We obtained a physical length of 692 µm, which is almost the same length of the waveguides between the OAM coupler and the power splitters. The spectrum also has another small interference with a FSR of 0.225 nm. This another FSR corresponds to a physical length of 1230 µm, which is almost the length between the OAM coupler and the SMF coupler.

We can also notice that the bandwidth is very narrow taking into account the degradation of the crosstalk. A wavelength change less than 5 nm is enough to degrade the crosstalk in more than 3 dB. This can be attributed to the wavelength dependence of the phase shift of each antenna. To verify this dependence we calculate the waveguide effective index for a wavelength range from 1450 nm to 1650 nm simulating it in Lumerical Mode Solutions. The obtained result is shown in Fig. 4.21(a).

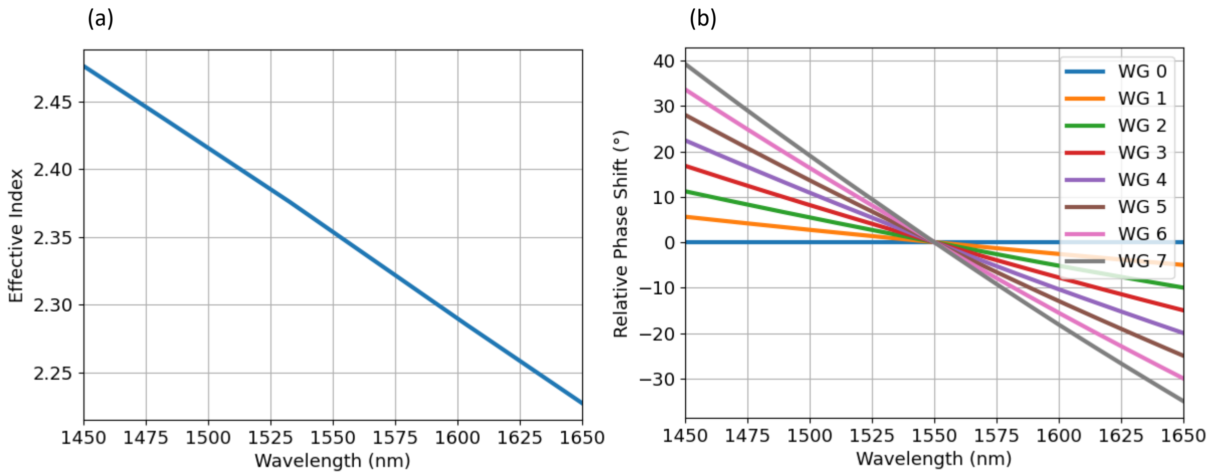

Figure 4.21: Analysis of the relative phase shift of each waveguide (WG) in function of the wavelength. (a) Waveguide effective index in function of the wavelength. (b) Relative phase shift in function of the wavelength.

With the results of effective index and the values of phase shift and length difference of Table 4.1 for the OAM_1 mode, we calculate the relative phase shift of each antenna waveguide in function of the wavelength using Eq. 4.3. The obtained result is shown in Fig. 4.21(b). As we can see, the wavelength change has a great impact on the phase shift. For one of the waveguides, a wavelenght change of only 25 nm implies in a relative phase shift of almost 10°, while a wavelength change of 100 nm implies in a relative phase shift of almost 40°. This explains why the obtained results have a narrow bandwidth. Then, the OAM coupler must be fine tuned for each operation wavelength.

Chapter 5

Conclusion

In this work, we discuss the use of SDM to address the increasing demand for data transmission capacity in fiber-optic communication systems. MDM is considered the most promising method to increase the number of communication channels and the family of modes that carry OAM is an attractive modal basis for MDM due to the robustness of those modes against perturbations. Although OAM modes can be easily generated in free-space, it requires very bulky and sensitive to misalignment setups. Then, we investigated the use of integrated couplers as compact and efficient solutions for the generation and detection of OAM fiber modes.

For the design of the integrated OAM couplers, we took as reference the OAM fiber modes supported by a HC-PCF available in our laboratory. We proposed three types of integrated OAM couplers using the SOI platform. The first proposed coupler is based on an array of compact antennas, where the phase of each antenna is tuned to maximize the coupling with the desired OAM fiber mode. The second proposed coupler is a circular grating with multiple input waveguides, where the phase of each input waveguide is tuned for the desired OAM fiber mode. We also explored the use of topology optimization for the design of OAM couplers. A new compact antenna was designed for the antenna array OAM coupler, where the power coupling at the wavelength of 1550 nm was optimized and the fabrication complexity was reduced using a single etch step. The third proposed coupler is based on the inverse design of the OAM coupler using topology optimization.

Simulation results showed the generation of OAM modes by all proposed couplers. The performance of the OAM couplers was evaluated calculating the overlap integral with the OAM fiber modes. The inverse designed OAM couplers showed the best results of mode overlap (-2.24 dB for the fundamental and -3.99 dB for the high-order OAM fiber modes), however each designed device can only couple a particular OAM fiber mode. On the other hand, the antenna array and the circular grating can be tuned for different OAM fiber modes. The circular grating showed better results of mode overlap than the antenna array, but at the expense of a higher dependence on the OAM mode, while the antenna array showed similar mode overlap results among all OAM modes. The intermodal crosstalk results were very lower between the fundamental and the high-order OAM modes using the antenna array ($<40\,\mathrm{dB}$) and the circular grating ($<-30\,\mathrm{dB}$) than using the inverse designed couplers ($<-13\,\mathrm{dB}$). However, the crosstalk between the high-order OAM modes were slighty higher for the antenna array and for the circular grating ($<-8\,\mathrm{dB}$) than for the inverse designed OAM couplers ($<-13\,\mathrm{dB}$).

We also fabricated one of the proposed couplers, the array of compact antennas, in a MPW run at IMEC. For the characterization of the OAM couplers, we designed two types of photonic integrated circuits. The first type was entirely passive, where the phase of each antenna is shifted by changing the length of the waveguides. The second type uses metal heaters beneath the waveguides to thermally control the phase of the antennas. Experimental results showed that the passive OAM couplers did not excite the correct OAM fiber modes. This was attributed to the fabrication variations in the waveguide width, which, as analysed, can cause a significant phase shift for a phase mismatch between the OAM fiber modes and the OAM coupler. Using the active OAM couplers, we could fine tune the phase shift of each antenna and excite the correct OAM fiber modes. The transmission results are in agreement with the simulation results. The couplers with shorter radius obtained slightly better transmission results and the couplers with larger radius obtained slightly better crosstalk results ($<-10\,\mathrm{dB}$). The crosstalk results are also limited by the intermodal crosstalk inside the fiber, which is around $-15\,\mathrm{dB}$.

As suggestions for future works, we propose the implementation of an automated system to control the electrical current of the metal heaters and optimize the coupling with the OAM fiber modes. This could be done using a control loop mechanism with power feedback such as a Proportional Integral Derivative (PID) controller or training a neural network to determine the set of electrical current values for each OAM mode. To design more efficient OAM couplers, we suggest to proceed with the inverse design approach. Using more etching levels and considering smaller minimum feature sizes achieved with electron-beam lithography, more efficient couplers could be obtained. We also suggest the inverse design of a device that couples multiple OAM fiber modes at the same time. This device could have multiple inputs, one for each OAM fiber mode, or a single multimode input and the OAM modes could be multiplexed using an integrated mode multiplexer.

References

[1] Y. Shen, X. Wang, Z. Xie, C. Min, X. Fu, Q. Liu, M. Gong, and X. Yuan, "Optical vortices 30 years on: Oam manipulation from topological charge to multiple singularities," *Light: Science & Applications*, vol. 8, p. 90, Oct 2019.

[2] X. Wang and Y. Song, "Encoding and decoding by the states of vector modes for vortex beams propagating in air-core fiber," *Opt. Express*, vol. 25, pp. 29342–29355, Nov 2017.

[3] A. M. Yao and M. J. Padgett, "Orbital angular momentum: origins, behavior and applications," *Adv. Opt. Photon.*, vol. 3, pp. 161–204, Jun 2011.

[4] R. Chen, H. Zhou, M. Moretti, X. Wang, and J. Li, "Orbital angular momentum waves: Generation, detection, and emerging applications," *IEEE Communications Surveys Tutorials*, vol. 22, no. 2, pp. 840–868, 2020.

[5] H. S. Dutta, A. K. Goyal, V. Srivastava, and S. Pal, "Coupling light in photonic crystal waveguides: A review," *Photonics and Nanostructures - Fundamentals and Applications*, vol. 20, pp. 41–58, 2016.

[6] B. Guan, R. P. Scott, C. Qin, N. K. Fontaine, T. Su, C. Ferrari, M. Cappuzzo, F. Klemens, B. Keller, M. Earnshaw, and S. J. B. Yoo, "Free-space coherent optical communication with orbital angular, momentum multiplexing/demultiplexing using a hybrid 3d photonic integrated circuit," *Opt. Express*, vol. 22, pp. 145–156, Jan 2014.

[7] T. Su, R. P. Scott, S. S. Djordjevic, N. K. Fontaine, D. J. Geisler, X. Cai, and S. J. B. Yoo, "Demonstration of free space coherent optical communication using integrated silicon photonic orbital angular momentum devices," *Opt. Express*, vol. 20, pp. 9396–9402, Apr 2012.

[8] "Lumerical - optimizable geometry - python api." https://support.lumerical.com/hc/en-us/articles/360052044913-Optimizable-Geometry-Python-API. Accessed 2021-09-03.

[9] E. A. L. Rubio, *Characterization and manipulation of optical modes in photonic crystal fibers : Caracterização e manipulação de modos ópticos em fibras de cristal*

fotônico. Campinas, SP: 1 recurso online (133 p.). Tese (doutorado) - Universidade Estadual de Campinas, Instituto de Física Gleb Wataghin, 2019. Accessed 2021-10-16.

[10] "Cisco annual internet report (2018–2023) white paper." https://www.cisco.com/c/en/us/solutions/collateral/executive-perspectives/annual-internet-report/white-paper-c11-741490.html. Accessed 2021-12-06.

[11] R.-J. Essiambre, R. W. Tkach, and R. Ryf, "Chapter 1 - fiber nonlinearity and capacity: Single-mode and multimode fibers," in *Optical Fiber Telecommunications (Sixth Edition)* (I. P. Kaminow, T. Li, and A. E. Willner, eds.), Optics and Photonics, pp. 1–43, Boston: Academic Press, sixth edition ed., 2013.

[12] D. B. Payne, "Optical networks," in *Fibre Optic Communication: Key Devices* (H. Venghaus and N. Grote, eds.), pp. 1–53, Berlin, Heidelberg: Springer Berlin Heidelberg, 2012.

[13] F. Idachaba, D. Ike, and O. Evwieroghene, "Future trends in fiber optics communication," *Lecture Notes in Engineering and Computer Science*, vol. 1, pp. 438–442, 07 2014.

[14] J. Du, W. Shen, J. Liu, Y. Chen, X. Chen, and Z. He, "Mode division multiplexing: from photonic integration to optical fiber transmission [invited]," *Chin. Opt. Lett.*, vol. 19, p. 091301, Sep 2021.

[15] A. Trichili, K.-H. Park, M. Zghal, B. S. Ooi, and M.-S. Alouini, "Communicating using spatial mode multiplexing: Potentials, challenges, and perspectives," *IEEE Communications Surveys Tutorials*, vol. 21, no. 4, pp. 3175–3203, 2019.

[16] A. M. Yao and M. J. Padgett, "Orbital angular momentum: origins, behavior and applications," *Adv. Opt. Photon.*, vol. 3, pp. 161–204, Jun 2011.

[17] S. Y. Siew, B. Li, F. Gao, H. Y. Zheng, W. Zhang, P. Guo, S. W. Xie, A. Song, B. Dong, L. W. Luo, C. Li, X. Luo, and G.-Q. Lo, "Review of silicon photonics technology and platform development," *Journal of Lightwave Technology*, vol. 39, no. 13, pp. 4374–4389, 2021.

[18] N. Margalit, C. Xiang, S. Bowers, A. Bjorlin, R. Blum, and J. Bowers, "Perspective on the future of silicon photonics and electronics," *Applied Physics Letters*, vol. 118, p. 220501, 05 2021.

[19] X. Cai, J. Wang, M. J. Strain, B. Johnson-Morris, J. Zhu, M. Sorel, J. L. O'Brien, M. G. Thompson, and S. Yu, "Integrated compact optical vortex beam emitters," *Science*, vol. 338, no. 6105, pp. 363–366, 2012.

[20] J. Sun, M. Moresco, G. Leake, D. Coolbaugh, and M. R. Watts, “Generating and identifying optical orbital angular momentum with silicon photonic circuits,” *Opt. Lett.*, vol. 39, pp. 5977–5980, Oct 2014.

[21] J. Baumann, *Silicon Photonic Integrated Devices for Space-Division Multiplexing.* PhD Thesis. Technical University of Denmark, 2019.

[22] C. T. Nadovich, W. D. Jemison, D. J. Kosciolek, and D. T. Crouse, “Focused apodized forked grating coupler,” *Opt. Express*, vol. 25, pp. 26861–26874, Oct 2017.

[23] Y. Chen, L. A. Rusch, and W. Shi, “Integrated circularly polarized oam generator and multiplexer for fiber transmission,” *IEEE Journal of Quantum Electronics*, vol. 54, pp. 1–9, April 2018.

[24] C. R. Doerr, N. K. Fontaine, and M. Hirano, “Silicon photonic integrated circuit for coupling to a ring-core multimode fiber for space-division multiplexing,” in *2011 37th European Conference and Exhibition on Optical Communication*, pp. 1–3, 2011.

[25] G. P. Agrawal, “Optical fibers,” in *Fiber-Optic Communication Systems*, ch. 2, pp. 23–76, John Wiley & Sons, Ltd, 2002.

[26] P. Nouchi, P. Sillard, and D. Molin, “Optical fibres,” in *Fibre Optic Communication: Key Devices* (H. Venghaus and N. Grote, eds.), pp. 55–97, Berlin, Heidelberg: Springer Berlin Heidelberg, 2012.

[27] C.-C. Su, “On the scalar approximation in fiber optics,” *IEEE Transactions on Microwave Theory and Techniques*, vol. 36, no. 6, pp. 1100–1103, 1988.

[28] K. Ingerslev, *Advanced Space-division Multiplexing for Optical Communications.* PhD thesis, Technical University of Denmark, 2018.

[29] L. Allen, M. W. Beijersbergen, R. J. C. Spreeuw, and J. P. Woerdman, “Orbital angular momentum of light and the transformation of laguerre-gaussian laser modes,” *Phys. Rev. A*, vol. 45, pp. 8185–8189, Jun 1992.

[30] M. C. Zanarella, *Propagação de modos com momento angular orbital em meios não-guiados e guiados.* Campinas, SP: 1 recurso online (141 p.). Universidade Estadual de Campinas, Faculdade de Engenharia Elétrica e de Computação, 2017. Accessed 2019-11-07.

[31] H. Lou, X. Ge, and Q. Li, “The new purity and capacity models for the oam-mmwave communication systems under atmospheric turbulence,” *IEEE Access*, vol. 7, pp. 129988–129996, 2019.

[32] J. Wang, J. Liu, S. Li, Y. Zhao, J. Du, and L. Zhu, "Orbital angular momentum and beyond in free-space optical communications," *Nanophotonics*, vol. 11, no. 4, pp. 645–680, 2022.

[33] Y. Lian, X. Qi, Y. Wang, Z. Bai, Y. Wang, and Z. Lu, "Oam beam generation in space and its applications: A review," *Optics and Lasers in Engineering*, vol. 151, p. 106923, 2022.

[34] U. Levy, S. Derevyanko, and Y. Silberberg, "Chapter four - light modes of free space," in *Progress in Optics* (T. D. Visser, ed.), vol. 61 of *Progress in Optics*, pp. 237–281, Elsevier, 2016.

[35] N. C. L. Valdivia, *Descrição de feixes de Bessel-Gauss e suas superposições do tipo Frozen Wave na teoria generalizada de Lorenz-Mie.* São Carlos, SP: Tese (Doutorado em Telecomunicações) - Escola de Engenharia de São Carlos, Universidade de São Paulo, 2020. Accessed 2022-05-27.

[36] A. Trichili, K. Park, M. Zghal, B. S. Ooi, and M. Alouini, "Communicating using spatial mode multiplexing: Potentials, challenges, and perspectives," *IEEE Communications Surveys Tutorials*, vol. 21, no. 4, pp. 3175–3203, 2019.

[37] A. Rjeb, H. Fathallah, and M. Machhout, "Oam modes in optical fibers for next generation space division multiplexing (sdm) systems," in *Fiber Optics* (G. Huerta-Cuellar, ed.), ch. 5, Rijeka: IntechOpen, 2021.

[38] L. E. E. de Araujo and M. E. Anderson, "Measuring vortex charge with a triangular aperture," *Opt. Lett.*, vol. 36, pp. 787–789, Mar 2011.

[39] M. E. Anderson, H. Bigman, L. E. E. de Araujo, and J. L. Chaloupka, "Measuring the topological charge of ultrabroadband, optical-vortex beams with a triangular aperture," *J. Opt. Soc. Am. B*, vol. 29, pp. 1968–1976, Aug 2012.

[40] A. Mourka, J. Baumgartl, C. Shanor, K. Dholakia, and E. M. Wright, "Visualization of the birth of an optical vortex using diffraction from a triangular aperture," *Opt. Express*, vol. 19, pp. 5760–5771, Mar 2011.

[41] R. Marchetti, C. Lacava, L. Carroll, K. Gradkowski, and P. Minzioni, "Coupling strategies for silicon photonics integrated chips [invited]," *Photon. Res.*, vol. 7, pp. 201–239, Feb 2019.

[42] "Lumerical - evanescent waveguide couplers." https://support.lumerical.com/hc/en-us/articles/360042304694-Evanescent-waveguide-couplers. Accessed 2022-02-21.

[43] D. M. Fatkhiev, M. A. Butt, E. P. Grakhova, R. V. Kutluyarov, I. V. Stepanov, N. L. Kazanskiy, S. N. Khonina, V. S. Lyubopytov, and A. K. Sultanov, "Recent advances in generation and detection of orbital angular momentum optical beams—a review," *Sensors*, vol. 21, no. 15, 2021.

[44] E. Lamilla, M. S. Faria, I. Aldaya, P. F. Jarschel, J. L. Pita, and P. Dainese, "Characterization of surface-states in a hollow core photonic crystal fiber," *Opt. Express*, vol. 26, pp. 32554–32564, Dec 2018.

[45] A. Nechibvute and C. Mudzingwa, "Modelling of optical waveguide using comsol multiphysics," *International Journal of Engineering Research & Technology (IJERT)*, vol. 2, May 2013.

[46] J. L. Pita, I. Aldaya, P. Dainese, H. E. Hernandez-Figueroa, and L. H. Gabrielli, "Design of a compact cmos-compatible photonic antenna by topological optimization," *Opt. Express*, vol. 26, pp. 2435–2442, Feb 2018.

[47] "Lumerical - finite difference time domain (fdtd) solver introduction." https://support.lumerical.com/hc/en-us/articles/360034914633-Finite-Difference-Time-Domain-FDTD-solver-introduction. Accessed 2021-03-29.

[48] D. M. Sullivan, *Electromagnetic Simulation Using the FDTD Method*. New York: Wiley-IEEE Press, 2000.

[49] "Lumerical - overlap script command." https://support.lumerical.com/hc/en-us/articles/360034405254-overlap-Script-command. Accessed 2021-05-06.

[50] L. Chrostowski and M. Hochberg, *Silicon Photonics Design: From Devices to Systems*. Cambridge University Press, 2015.

[51] Y. del Valle, G. K. Venayagamoorthy, S. Mohagheghi, J.-C. Hernandez, and R. G. Harley, "Particle swarm optimization: Basic concepts, variants and applications in power systems," *IEEE Transactions on Evolutionary Computation*, vol. 12, no. 2, pp. 171–195, 2008.

[52] I. Pereira Rosinha, K. Gernaey, J. Woodley, and U. Krühne, "Topology optimization for biocatalytic microreactor configurations," in *Proceedings of the 25th European Symposium on Computer Aided Process Engineering* (K. Gernaey, J. Huusom, and R. Gani, eds.), vol. 37 of *Computer Aided Chemical Engineering*, (United Kingdom), pp. 1463–1468, Elsevier, 2015. 25th European Symposium on Computer Aided Process Engineering : 12th International Symposium on Process Systems Engineering, PSE2015/ESCAPE25 ; Conference date: 31-05-2015 Through 04-06-2015.

[53] V. Shobeiri, "Structural topology optimization based on the smoothed finite element method," *Latin American Journal of Solids and Structures [online]*, vol. 13, pp. 378–390, Feb 2016.

[54] A. Michaels and E. Yablonovitch, "Leveraging continuous material averaging for inverse electromagnetic design," *Opt. Express*, vol. 26, pp. 31717–31737, Nov 2018.

[55] L. Su, D. Vercruysse, J. Skarda, N. V. Sapra, J. A. Petykiewicz, and J. Vuckovic, "Nanophotonic inverse design with spins: Software architecture and practical considerations," 2019.

[56] C. M. Lalau-Keraly, S. Bhargava, O. D. Miller, and E. Yablonovitch, "Adjoint shape optimization applied to electromagnetic design," *Opt. Express*, vol. 21, pp. 21693–21701, Sep 2013.

[57] J. W. Nicholson, A. D. Yablon, S. Ramachandran, and S. Ghalmi, "Spatially and spectrally resolved imaging of modal content in large-mode-area fibers," *Opt. Express*, vol. 16, pp. 7233–7243, May 2008.

[58] "Lumerical - grating coupler." https://support.lumerical.com/hc/en-us/articles/360042305334-Grating-coupler. Accessed 2021-07-15.

Appendix A

Implementation and Validation of the Mode Overlap Analysis

As described in Chapter 3, to evaluate the mode overlap between the generated beam and the fiber mode, we calculate the overlap integral according to [49]:

$$C = \left| \Re \left\{ \frac{\left(\int \vec{E}_1 \times \vec{H}_2^* \cdot \mathrm{d}\vec{S}\right)\left(\int \vec{E}_2 \times \vec{H}_1^* \cdot \mathrm{d}\vec{S}\right)}{\int \vec{E}_1 \times \vec{H}_1^* \cdot \mathrm{d}\vec{S}} \right\} \frac{1}{\Re\left\{\int \vec{E}_2 \times \vec{H}_2^* \cdot \mathrm{d}\vec{S}\right\}} \right| \tag{A.1}$$

where $\vec{E}_1$ and $\vec{H}_1$ are the electric and magnetic fields, respectively, from the generated beam, while $\vec{E}_2$ and $\vec{H}_2$ are the electric and magnetic fields, respectively, from the fiber mode. C is the overlap result, which represents a measure of the fraction of electromagnetic fields that overlaps between the two modes.

From the simulations results, we obtain each component (x, y and z) of both electric and magnetic fields in the form of two-dimensional arrays. Each element of the arrays represents the field intensity in the discretized surface. In order to calculate the overlap integral using these data, the field vectors are decomposed as:

$$\vec{E}_1 = E_{1x}\hat{\imath} + E_{1y}\hat{\jmath} + E_{1z}\hat{k} \tag{A.2a}$$
$$\vec{H}_1 = H_{1x}\hat{\imath} + H_{1y}\hat{\jmath} + H_{1z}\hat{k} \tag{A.2b}$$
$$\vec{E}_2 = E_{2x}\hat{\imath} + E_{2y}\hat{\jmath} + E_{2z}\hat{k} \tag{A.2c}$$
$$\vec{H}_2 = H_{2x}\hat{\imath} + H_{2y}\hat{\jmath} + H_{2z}\hat{k} \tag{A.2d}$$

Given that all cross products of Eq. A.1 are used for the inner product with $\mathrm{d}\vec{S}$, which is in the z-direction, we don't need the z-components of the fields and the cross products can be given by:

$$\vec{E}_1 \times \vec{H}_2^* = (E_{1x} \cdot H_{2y}^* - E_{1y} \cdot H_{2x}^*)\hat{k} \tag{A.3a}$$
$$\vec{E}_2 \times \vec{H}_1^* = (E_{2x} \cdot H_{1y}^* - E_{2y} \cdot H_{1x}^*)\hat{k} \tag{A.3b}$$
$$\vec{E}_1 \times \vec{H}_1^* = (E_{1x} \cdot H_{1y}^* - E_{1y} \cdot H_{1x}^*)\hat{k} \tag{A.3c}$$
$$\vec{E}_2 \times \vec{H}_2^* = (E_{2x} \cdot H_{2y}^* - E_{2y} \cdot H_{2x}^*)\hat{k} \tag{A.3d}$$

An algorithm was implemented in Python[1] to perform the mathematical operations on array elements and calculate the surface integrals. As a final result we obtain the overlap fraction in the range from 0 to 1, which is converted to logarithmic scale.

To validate this algorithm, we compare its result with the one obtained in a tool inside Lumerical Mode Solution for the mode overlap of a standard SMF with a conventional grating coupler. In the Mode Solution software, after we perform a modal analysis and obtain the supported modes, we can use this tool to select one of the supported modes and calculate the overlap with another mode imported from an external file. In this way, we performed the modal analysis in the SMF and evaluate the overlap between its fundamental mode and the emmited beam by the grating coupler. The grating coupler was designed based on [58] for an angle of 0°, i.e. normal to the device surface. This angle was chosen in order to obtain the results of the emmited beam in a slice 2 µm above the device and parallel to the device surface. The grating coupler was simulated using Lumerical FDTD Solution and its result was exported to Mode Solution. The SMF fundamental mode can be seen in Fig. A.1(a) and the results of the grating coupler emitted beam can be seen in Fig. A.1(b).

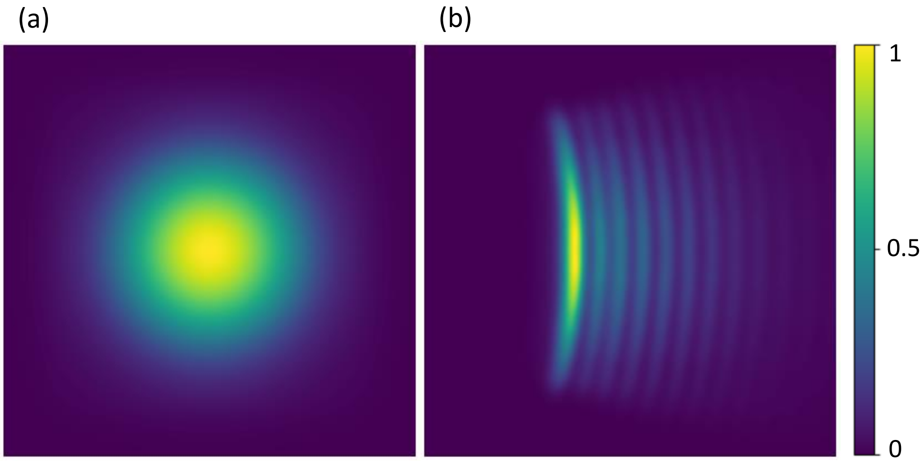

Figure A.1: (a) SMF fundamental mode and (b) grating coupler emitted beam.

Calculating the mode overlap using the tool inside the Mode Solution software,

[1] https://www.python.org/

we obtained a value of 0.426 568 (−3.70 dB), as we can see in Fig. A.2. Exporting both modes and calculating the overlap using our algorithm, we obtained a value of −3.68 dB, which validates our algorithm.

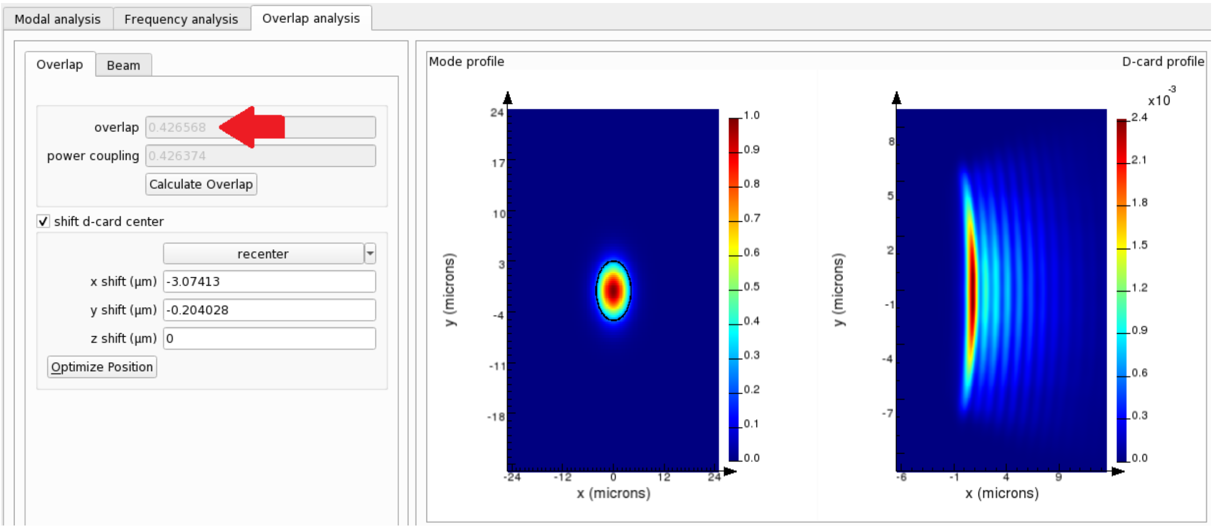

Figure A.2: Overlap result between SMF mode and grating coupler emitted beam using Lumerical Mode Solutions.